

SYNTHESIS OF GERMANIUM NANOWIRES BY VAPOR TRANSPORT AND  
FABRICATION OF TRANSPARENT AND FLEXIBLE PHOTODETECTORS

A THESIS SUBMITTED TO  
THE GRADUATE SCHOOL OF NATURAL AND APPLIED SCIENCES  
OF  
MIDDLE EAST TECHNICAL UNIVERSITY

BY  
BURCU AKSOY

IN PARTIAL FULFILLMENT OF THE REQUIREMENTS  
FOR  
THE DEGREE OF MASTER OF SCIENCE  
IN  
METALLURGICAL AND MATERIALS ENGINEERING

JUNE 2012

Approval of the thesis:

**SYNTHESIS OF GERMANIUM NANOWIRES BY VAPOR TRANSPORT  
AND FABRICATION OF FULLY TRANSPARENT FLEXIBLE  
PHOTODETECTORS**

submitted by **BURCU AKSOY** in partial fulfillment of the requirements for the degree of **Master of Science in Metallurgical and Materials Engineering Department, Middle East Technical University** by,

Prof. Dr. Canan Özgen  
Dean, Graduate School of **Natural and Applied Sciences**

\_\_\_\_\_

Prof. Dr. Hakan Gür  
Head of Department, **Metallurgical and Materials Engineering**

\_\_\_\_\_

Assist. Prof. Dr. Hüsnü Emrah Ünalın  
Supervisor, **Metallurgical and Materials Eng. Dept., METU**

\_\_\_\_\_

**Examining Committee Members:**

Prof. Dr. Tayfur Öztürk  
Department of Metallurgical and Materials Engineering, METU

\_\_\_\_\_

Assist. Prof. Dr. Hüsnü Emrah Ünalın  
Department of Metallurgical and Materials Engineering, METU

\_\_\_\_\_

Prof. Dr. Raşit Turan  
Department of Physics, METU

\_\_\_\_\_

Assoc. Prof. Dr. Fehmi Arcan Dericioğlu  
Department of Metallurgical and Materials Engineering, METU

\_\_\_\_\_

Assoc. Prof. Dr. Caner Durucan  
Department of Metallurgical and Materials Engineering, METU

\_\_\_\_\_

**Date: 22.06.2012**

**I hereby declare that all information in this document has been obtained and presented in accordance with academic rules and ethical conduct. I also declare that, as required by these rules and conduct, I have fully cited and referenced all material and results that are not original to this work.**

Name, Last name : Burcu AKSOY

Signature :

## **ABSTRACT**

### **SYNTHESIS OF GERMANIUM NANOWIRES BY VAPOR TRANSPORT AND FABRICATION OF FULLY TRANSPARENT FLEXIBLE PHOTODETECTORS**

AKSOY, Burcu

Master of Science, Department of Metallurgical and Materials Engineering

Supervisor: Assist. Prof. Dr. Hüsnü Emrah ÜNALAN

June 2012, 86 pages

Nanomaterials are widely investigated by researches and because of their unique properties they have been utilized in many different devices. Nanowires are one of these materials which show deviated mechanical, chemical, physical and optical, properties from their bulk counterparts. These deviations in properties of the nanowires are based on both their high surface to volume ratio and quantum confinement effect. Lately optical properties of nanowires have received great attention as they also exhibit good light sensitivity. Germanium is a semiconductor, which has been used widely as an active material in infrared light detectors. Due to excellent light detection of germanium its nanostructures have also been widely studied in optoelectronic devices. Germanium nanowires have been used in many devices such as field effect transistors, diodes, field emitters and photodetectors. Synthesis of high quality and high aspect ratio germanium nanowires could make important contributions to these devices. There are several synthesis methods for germanium nanowires. These are electrochemical etching, solvothermal, supercritical

fluidic, laser ablation, chemical vapor deposition and vapor transport methods. Among these methods, high quality, single crystalline, defect free germanium nanowires using accessible solid powder precursors could be synthesized with vapor transport method.

In the first part of this thesis, germanium nanowire growth with vapor transport method is investigated. One of the most advantageous features of this method is using solid powder precursors instead of toxic gases. Until now, three different kinds of solid germanium precursors have been reported in vapor transport method, all of them are investigated and the resulting nanowires are compared in this thesis. Vapor transport method enables high control over the morphology of the nanowires. The most important parameters which affect the morphology of the nanowires are temperature, pressure and precursor type. Therefore, a detailed parametric study is provided based on these parameters and their effect on the final diameter of the nanowires is determined. The as-synthesized nanowires contain a very thick oxide layer on their surface. Therefore, oxide removal with acid etching is also investigated in this thesis.

In the second part of this thesis, utilization of the germanium nanowire networks in fully transparent, flexible and network enhanced photodetectors is investigated. In order to obtain a germanium nanowire network, the as-synthesized nanowires are transferred from growth substrate to the device substrate by sonication and vacuum filtration. Silver nanowires and single walled carbon nanotubes are used as fully transparent electrodes. Both rigid and flexible photodetectors are fabricated and their current-voltage characteristics and photoresponse behaviors with different germanium nanowire densities are determined.

**Keywords:** germanium nanowires, vapor transport, network enhanced photodetectors.

## ÖZ

# GERMANYUM NANOTELERİN BUHAR TRANSFERİ YÖNTEMİ İLE SENTEZİ VE ŞEFFAF, ESNEK FOTOALGILAYICI ÜRETİMİ

AKSOY, Burcu

Yüksek Lisans, Metalurji ve Malzeme Mühendisliği Bölümü

Tez Yöneticisi: Yrd. Doç. Dr. Hüsnü Emrah ÜNALAN

Haziran 2012, 86 sayfa

Nanomalzemeler farklı özelliklerinden dolayı geniş ölçüde çalışılmakta ve çeşitli cihazlarda kullanılmaktadırlar. Nanoteller de kütle halindeki malzemelere göre farklı mekanik, kimyasal, fiziksel ve optik özellikler gösteren nanomalzemelerden birisidir. Nanotellerdeki bu farklılıklar geniş yüzey alanlarından ve iki yönlü kuantum sınırlamasından kaynaklanmaktadır. Nanotellerin gelişmiş ışık hassalığı göstermeleri son zamanlarda optik özelliklerinin büyük ilgi toplamasına neden oldu. Germanyum kızılötesi algılayıcılarda aktif malzeme olarak kullanılan bir yarıiletkenidir. Germanyumun çok iyi bir optik sensör olması, nanomalzemelerinin de optoelektronik cihazlarda kullanılmasına neden olmuştur. Germanyum nanoteller alan etkili transistör, diyot, alan salıcısı ve fotoalgılayıcı olmak üzere pek çok cihazda kullanılmıştır. Bu nedenle en boy oranı yüksek, kaliteli germanyum nanotel sentezi kullanıldığı bu cihazlara büyük katkı sağlayacaktır. Germanyum nanotel üretimi için geliştirilmiş birçok yöntem vardır. Bunlar; elektrokimyasal dağlama, solvotermal, süperkritik akışkan, lazer ablasyon, kimyasal buhar biriktirme ve buhar

transfer yöntemleridir. Bunların içinde yüksek kaliteli, tek kristalli, hata içermeyen germanyum nanoteller buhar transferi yöntemi ile kolay kontrol edilebilir toz öncü maddeler kullanılarak üretilebilir.

Bu tez çalışmasının ilk bölümünde, buhar transferi yöntemi ile germanyum nanotel üretimi incelenmektedir. Bu yöntemin en önemli avantajlarından biri zehirli gazlar yerine katı toz öncü maddelerin kullanılmasıdır. Şimdiye kadar buhar transferi ile germanyum nanotel üretiminde üç farklı toz öncü madde kullanılmıştır. Bu tez çalışmasında bu öncü maddelerin hepsi incelenmiş ve bunlardan üretilen nanoteller kıyaslanmıştır. Buhar transferi yöntemi ile üretilen nanotellerin biçimi kontrol edilebilir. Nanotel biçimini etkileyen en önemli parametreler sıcaklık ve basınçtır bu nedenle, üç farklı öncü maddeden üretilen germanyum nanotellerin çaplarının sıcaklık ve basınca göre değişimlerinin ayrıntılı parametrik çalışmaları bu tezde sunulmaktadır. Üretilen nanotellerin yüzeylerinde kalın bir oksit tabakası bulunmaktadır bu nedenle asit dağlama yöntemi ile oksit tabakasının kaldırılması da bu tezde çalışılmıştır.

Tezin ikinci bölümünde, germanyum nanotel ağlarının şeffaf, esnek fotoalgılayıcılarda kullanımı incelenmiştir. Germanyum nanotel ağı elde etmek için, üretilen germanyum nanoteller üretim altlıklarından cihaz altlıklarına ses titreşimi ve vakum filtreleme yöntemleri ile transfer edilmiştir. Gümüş nanotel ve tek duvarlı karbon nanotüp ağları şeffaf elektrotlar olarak kullanılmıştır. Esnek ve de esnek olmayan fotoalgılayıcılar üretilmiş ve bunların akım-voltaj karakteristikleri ile ışığa karşı olan duyarlılıkları farklı germanyum nanotel yoğunluklarında incelenmiştir.

**Anahtar Kelimeler:** germanyum nanoteller, buhar transferi, ağ yapısı ile güçlendirilmiş fotoalgılayıcılar.

*To My Family...*

## ACKNOWLEDGEMENTS

There are so many who must be thanked for their both moral and technical support for bringing this project to fruition.

First of all I wish to thank my advisor, Assist. Prof. Dr. Emrah Ünalın for all of his support, patience and tolerance throughout the whole time I have worked on this project. I also would like to thank Saffet Ayık, Serkan Yılmaz, Güher Kotan and Assist. Prof. Dr. Eren Kalay for spending infinite hours of SEM/TEM sessions. I acknowledge VAKSİS, and in particular Dr. Baybars Oral, Hilmi Volkan Demir and Shahab Akhavan for their great technical support for the experimental setup and all SEM, TEM, XRD facilities in Department of Metallurgical and Materials Engineering.

I owe my deepest gratitude to my lab-mates and dearest friends Şahin Coşkun, Ayşegül Afal, Elif Selen Ateş, Barış Özdemir, Şeyda Küçükyıldız and Emre Mülazımoğlu for their infinite support, patience and kindness. I feel very lucky to have such good labmates and I will never forget their support and guidance through my study. I also appreciate the great moral support from İnci Dönmez and all my friends in my department who have helped and supported me all along.

And finally, I would like to thank my parents for their unconditional support and love through my whole life.

## TABLE OF CONTENTS

ABSTRACT.....	iv
ÖZ .....	vi
ACKNOWLEDGEMENTS .....	ix
TABLE OF CONTENTS.....	x
LIST OF FIGURES .....	xii

### CHAPTERS

1. INTRODUCTION .....	1
2. GERMANIUM NANOWIRE SYNTHESIS BY VAPOR TRANSPORT METHOD.....	5
2.1 Introduction .....	5
2.1.1 Features of NWs .....	5
2.1.2 Conventional Ge NW Synthesis Methods .....	14
2.2 Experimental Details .....	21
2.2.1 Synthesis of Ge NWs.....	21
2.3 NW Characterization Methods .....	30
2.3.1 Scanning Electron Microscope (SEM) .....	30
2.3.2 Transmission Electron Microscope (TEM) .....	30
2.3.3 X-Ray Photoelectron Spectroscopy (XPS) .....	30
2.3.4 X-Ray Diffraction Spectroscopy (XRD) .....	31
2.4 Results and Discussion .....	31

2.4.1 Determination of Synthesis Parameters .....	31
3. GERMANIUM NANOWIRE PHOTODETECTORS .....	51
3.1 Introduction .....	51
3.1.1 History of Photodetectors .....	51
3.1.2 Different Photodetector Models.....	53
3.2 Experimental Details .....	59
3.3 Device Characterization Methods .....	65
3.3.1 Scanning Electron Microscopy .....	65
3.3.2 Current-Voltage and Photoresponse Measurements.....	65
3.3.3 Optical Transmittance Measurements .....	66
3.4 Results .....	66
3.4.1 Transparency and Resistance Variation with Ge NW Network Density...	66
3.4.2 Ge NW Network Photodetector Characterization Results.....	69
4. CONCLUSIONS AND FUTURE RECOMMENDATIONS .....	76
4.1 Conclusions .....	76
4.2 Future Recommendations .....	77
REFERENCES.....	79

## LIST OF FIGURES

Figure 2. 1. The variation of squareness of hysteresis loops of Co NW arrays with applied magnetic field ( $H$ ) parallel ( $\parallel$ ) and perpendicular ( $\perp$ ) to the wire axes: (a) NW diameter, 78 nm and (b) NW diameter, 18 nm [2].	6
Figure 2. 2. Temperature dependent thermal conductivity ( $k$ ) of Si NWs [13].	7
Figure 2. 3. DOS of Ti NWs: (a) and (b) wire diameter $< 1$ nm and (c) and (d) wire diameter $> 1$ nm with 0.05 eV Gaussian broadening [15].	9
Figure 2. 4. The change in current as a function of time for an individual $\text{In}_2\text{O}_3$ NW when exposed to buffer and protein specific antigen (PSA). Inset: SEM image of the single $\text{In}_2\text{O}_3$ NW sensor device [18].	11
Figure 2. 5. Applications of Ge nanowires.	13
Figure 2. 6. Conventional Ge NW synthesis methods.	14
Figure 2. 7. HRSEM images of Ge NWs grown by Korgel et al. at 38 MPa for 20 min using TEG at (a) 300, (b) 400, (c) 500 $^\circ\text{C}$ and using DPG at (d) 300, (e) 400 and (f) 500 $^\circ\text{C}$ [33].	16
Figure 2. 8. SEM image of Ge NWs synthesized by Wang et al. Inset shows an atomic force microscopy (AFM) image of Au nanoclusters on Si substrate [33].	18
Figure 2. 9. SEM image of Ge NWs synthesized by Yan et al. Inset is a TEM image of a single Ge NW capped with Au catalyst [47].	21
Figure 2. 10. (a) Schematic and (b) photograph of chemical vapor deposition system used in this study.	23
Figure 2. 11. (a) Schematic drawing of the experimental set-up in the horizontal tube furnace. (b) Temperature distribution of the furnace, when it is set at 950 $^\circ\text{C}$ .	25
Figure 2. 12. Phase diagram of Au-Ge system [33].	26
Figure 2. 13. Schematic representation of the Vapor-Liquid-Solid (VLS) growth of Ge NWs.	28

Figure 2. 14. SEM images of the synthesized Ge nanostructures using Ge powder under different temperature and pressure conditions (50 sccm Ar gas flow and 2 nm Au catalyst are the same for all of them). Scale bars are all the same. ....	33
Figure 2. 15. Diameter change of Ge NWs synthesized using Ge powder with temperature and (b) pressure. ....	34
Figure 2. 16. SEM images of Ge nanostructures synthesized using GeO <sub>2</sub> and C powder mixture and at different temperature and pressure conditions. (50 sccm Ar gas flow and 2 nm Au catalyst are the same for all of them). Scale bars are all the same. ....	36
Figure 2. 17. Diameter change of Ge NWs synthesized using GeO <sub>2</sub> and C powder mixture with (a) temperature and (b) pressure. ....	37
Figure 2. 18. SEM images of Ge nanostructures synthesized using GeI <sub>4</sub> and Ge powder mixture and at different temperature and pressure conditions. (50 sccm Ar gas flow and 2 nm Au catalyst are the same for all of them). Scale bars are all the same. ....	39
Figure 2. 19. Diameter change of Ge NWs synthesized using GeI <sub>4</sub> and Ge powder mixture with (a) temperature and (b) pressure. ....	40
Figure 2. 20. XRD spectrum of Ge NWs (synthesized using Ge precursor, under 950 °C and 100 mbar) before and after HBr etching. ....	41
Figure 2. 21. XRD spectrum of the etched Ge NWs synthesized with different powder precursors. ....	42
Figure 2. 22. XPS spectra for (a) Ge and GeO <sub>2</sub> -3d signals and (b) oxygen-1s signals of as-synthesized Ge NWs. ....	43
Figure 2. 23. XPS spectra for (a) Ge-(3d) and (b) O-(1s) signals of etched Ge NWs. (c) Ge-(3d) 5/2 and 3/2 signal separation of the main Ge-(3d) signal. ....	44
Figure 2. 24. XPS spectra for (a) Ge-(3d) and (b) O-(1s) signals of as-synthesized, HBr etched and 2 days kept Ge NWs (synthesized with Ge precursor under 950 °C and 100 mbar). ....	45
Figure 2. 25. XPS spectrum for I-(3d) scan of Ge NWs synthesized using GeI <sub>4</sub> + Ge mixture precursor. ....	46

Figure 2. 26. (a) Low magnification TEM image of Ge NWs (synthesized with Ge precursor under 950 °C and 100 mbar). Inset shows a Ge NW with Au cap on it. (b) TEM image of a single Ge NW with oxidized surface (c) HRTEM image of a single Ge NW. Left inside shows inverse Fast Fourier transform (IFFT) image indicating the distance between (111) planes; right inset shows the Fast Fourier transform (FFT) pattern indicating the reciprocal space along [011] zone axis. [111] growth direction is indicated on the image.....	48
Figure 2. 27. TEM images of as-synthesized and HBr etched Ge NWs synthesized from (a,b) Ge powder, (c,d) GeO <sub>2</sub> and C powder mixture and (e,f) GeI <sub>4</sub> and Ge powder mixture. ....	50
Figure 3. 1. History of various IR photodetector materials [53]......	52
Figure 3. 2. Classification of photodetector devices [62]. ....	54
Figure 3. 3. Energy band diagram of p-n photodetectors.....	55
Figure 3. 4. Energy band diagram of a MSM photodetector under bias.....	56
Figure 3. 5. Flow chart of Ge NW transfer onto the glass or PET substrates.....	61
Figure 3. 6. (a-e) Flow chart of the fabrication procedure of Ge NW photodetectors. (f) SEM image of Ag NW network with a gap of 20 μm formed by mechanical scratching. SEM images of a (g) Ag-Ge and (h) SWNT-Ge photodetectors following Ge NW deposition.....	64
Figure 3. 7. Photograph of a fabricated Ge NW network photodetector. ....	65
Figure 3. 8. Half of the filter papers with different Ge NW network densities of i) 1.4, ii) 1.8, iii) 2.0, iiiii) 2.5 NWs/μm <sup>2</sup> .....	66
Figure 3. 9. SEM images of Ge NW networks deposited onto glass substrates with densities (a) 1.4, (b) 1.8, (c) 2.0 and (d) 2.5 NWs/μm <sup>2</sup> .....	67
Figure 3. 10. Transmittance of (a) Ge NW networks with different densities and (b) fabricated photodetectors. (c) Dark resistance variation of the Ge NW networks with transmittance measured at 550 nm.....	68
Figure 3. 11. A typical I-V curve for Ag-Ge NW network photodetectors under dark and light.....	69

Figure 3. 12. Light ON/OFF responses of Ag-Ge NW network photodetectors on glass substrates with different Ge NW densities.....	70
Figure 3. 13. (a) Enlarged view of the reset time of a Ge NW photodetector. The reset time is found to be less than 10 milliseconds. (b) Schematic of charge generation within the Ge NWs. (c) NW-NW junction barrier height variation with incident light. ....	72
Figure 3. 14. Comparison of light ON/OFF responses of Ag-Ge and SWNT-Ge NW photodetectors on glass substrates. ....	73
Figure 3. 15. A typical I-V curve for SWNT-Ge photodetectors on PET substrates.	74
Figure 3. 16. Light ON/OFF measurements of SWNT-Ge photodetectors on PET substrates with (a) different bending radius and (b) repeated bending cycles. Inset shows a flexible SWNT-Ge photodetector. ....	75
Figure 3. 17. Comparison of light ON/OFF responses of flat Ag-Ge and SWNT-Ge NW photodetectors on PET substrates.....	75

# CHAPTER 1

## INTRODUCTION

Technology necessitates the use of smaller devices as integrated circuits continue to shrink in size. Integrated circuit industry has been driven to improve the power of the chips, while miniaturizing the circuits such as transistors, resistors and capacitors. In the beginning, there were several thousand of transistors per chip, while today there are hundreds of millions of transistors for a single chip, each of which is several tens of nanometer in size [1]. While dimensions are reduced significantly, the conventional materials limit further size reduction due to physical and chemical reasons such as, lack of ultra fine precursors, high amount of heat generated at high speeds and rapid failure. At that point, nanomaterials open up new avenues and allow further size reduction, while improving the power consumption of integrated devices. They provide nanocrystalline pure precursors, better thermal conductivity and last longer when compared to bulk counterparts.

A material which has at least one of its dimensions below 100 nm is accepted as a nanomaterial. Quantum dots, thin films, nanowires (NWs) and nanoparticles are 4 main classes of nanomaterials. Besides their small dimensions, nanoscale materials have unique mechanical, electrical, chemical and optical properties, which arise from their high surface to volume ratio and quantum confinement effect. Because of these unique properties, they have been widely used in many optical, electrical and mechanical applications, such as next generation computer chips, optoelectronic devices, insulation materials, flat panel displays, pollutant eliminators, cutting tools, high energy density batteries, high power magnets, aerospace components and medical implants.

Germanium (Ge) is a narrow band gap (0.67 eV) semiconductor. Since now Ge has been investigated both in its bulk and nanostructure form in field effect transistors, solar cells, infrared photodetectors and photoconductors. Although silicon (Si) is the most widely used material in optoelectronic devices due its well known material properties, stable surface oxide, ease of fabrication and large photoconductive gain, its wide band gap (1.12 eV) limits applications of Si for the infrared region of the light spectrum. Moreover compared to Si, Ge has higher charge carrier mobility and carrier concentration which enables higher frequency devices, larger exciton Bohr radius (24.3 nm) which enables more prominent quantum confinement effects, higher absorption coefficient in the wavelength range of 800-1550 nm and it needs lower thermal energy for doping.

Nanomaterials can be fabricated with two different approaches, namely top-down and bottom-up. Top-down method involves reducing the size of a bulk material down to nanoscale. Bottom-up method, on the other hand involves using atoms to construct the nanostructure. For Ge NWs, mostly bottom-up growth techniques are applied. These include; solution methods such as solvothermal and supercritical fluidic synthesis and gas phase methods such as laser ablation, chemical vapor deposition (CVD) and vapor transport synthesis. Electrochemical etching method is also applied for Ge NWs as a top-down process. Solution methods enable low temperatures, simple equipments and low cost; however, quality of the resulting NWs is low and their reproducibility is limited. CVD synthesis enables low temperature growth of NWs. In this method, germane ( $\text{GeH}_4$ ) gas is used as the main precursor material; however, transportation and toxicity of  $\text{GeH}_4$  gas creates some problems. Likewise, electrochemical etching process provides a low cost and simple method for the synthesis of NWs over large areas; however, bundling of NWs and lack of reproducibility in synthesis create some drawbacks.

By vapor transport method, single crystalline and defect free NWs with excellent reproducibility, using solid powder precursors could be synthesized. Powder precursors are non-toxic and much easier to handle and transport compared to  $\text{GeH}_4$  gas. Another advantage of this method is to control the length and diameter of the

resulting NWs by altering temperature, pressure and incoming gas flow in the system. This method relies on vapor-liquid-solid growth, which is first applied by Wagner and Ellis in 1964. Simply in this method, Ge vapor is obtained from solid precursors at high temperature and carried to a thin layer of Au coated Si substrate. When Ge vapor reaches on the substrate, it makes an Au-Ge alloy and when the alloy supersaturates with Ge it grows as a NW. In the second chapter of this thesis NW synthesis with vapor transport method is studied with three different solid powder precursors. They are Ge powder, germanium dioxide ( $\text{GeO}_2$ )+ carbon (C) powder mixture and germanium iodide ( $\text{GeI}_4$ )+ Ge powder mixture. In the literature, synthesis of Ge NWs using these precursors have been conducted by different groups; however, a detailed parametric study on the process parameters is missing. In this thesis, a detailed parametric study was conducted and synthesized NWs were compared with each other in terms of their growth direction, crystal structure and surface oxidation states. Oxide removal from the NW surface was also studied in order to fabricate Ge NW photodetectors.

One of the most important advantages of one dimensional nanomaterials is their network structure. Conducting NWs such as silver (Ag) and carbon nanotubes (CNT) are widely used as transparent conducting electrodes. They provide both transparency and conductivity together. Moreover, because of their network structure they are highly resistant to bending unlike crystalline materials such as indium tin oxide (ITO) and metallic thin films. ITO and thin film conductors have been used as electrode materials in several applications; however, they are not suitable for solely flexible devices as they crack upon bending. In addition, ITO is not transparent in the infrared region of light spectrum. In literature, flexible devices have been studied with mostly thin film electrodes; however, because of the drawbacks mentioned before, these devices do not work properly after several bending cycles. In the third chapter of this thesis, fully transparent and flexible network enhanced Ge NW photodetectors are investigated. Both Ag NW and single walled carbon nanotube (SWNT) networks are studied as electrode materials. For the active material, Ge NW network is used. Therefore, these photodetectors are the first devices in which both

the active material and the electrodes are one dimensional nanostructures. In the early studies only single NW is used in the channel of the photodetectors; however, using NWs in the form of a network provides both easy fabrication and faster response. A parametric study is conducted and the effect of bending is investigated on the fabricated devices. Finally, Ag-Ge and SWNT-Ge photodetectors are compared.

## CHAPTER 2

### GERMANIUM NANOWIRE SYNTHESIS BY VAPOR TRANSPORT METHOD

#### 2.1 Introduction

##### 2.1.1 Features of NWs

Bulk materials contain grains ranging from micron to millimeter in size and within each grain there are billions of atoms. As grains are reduced to nanometer size number of atoms per grain decreases significantly down to about several hundreds. Therefore, volume fraction and the number of atoms in the grain boundaries and interfaces increase. This causes several deviations in physical and chemical properties of materials. Nanomaterials are classified into 4 main groups which are quantum dots, NWs, thin films and nanoparticles. As the dimension of a material decrease below a critical value, the carriers inside it start to get trapped and behave like a wave instead of a particle. This behavior only occurs if the dimension of the material is reduced below the de Broglie wavelength of the carriers. This effect is called quantum confinement and deviated electrical and optical properties of nanoscale materials originate from it. Materials, which show size depended electrical and optical properties are called quantized particles. NWs have two dimensional quantum confinements. The magnetic, thermal, electrical and optical behaviors of NWs which are greatly influenced by their high surface to volume ratio and 2 dimensional quantum confinement affect will be discussed briefly in this section.

Magnetic properties of materials are characterized by coercivity ( $H_c$ ), remanent magnetization ( $M_R$ ), and squareness of the hysteresis loop. These properties change with grain size. A bulk material consists of many magnetic domains in a single

crystal; therefore, its  $M_R$  and  $H_c$  is independent of particle size. However, as the particle size decreases there will be only one domain in the whole structure. Therefore,  $M_R$  and  $H_c$  of the material increase. If the particle size further decreases down to a critical dimension then these values begin to decrease resembling superparamagnetic (no remanence) behaviour. Many studies have been conducted on NWs to determine their magnetic properties [2]. It has been reported that as the diameter of the NWs is decreased, squareness of the hysteresis loop increases [3,4] which means, the material retains a large fraction of the saturation field ( $M_R$ ) when driving field ( $M_S$ ) is removed as it is illustrated in Figure 1.1 (a)-(b).

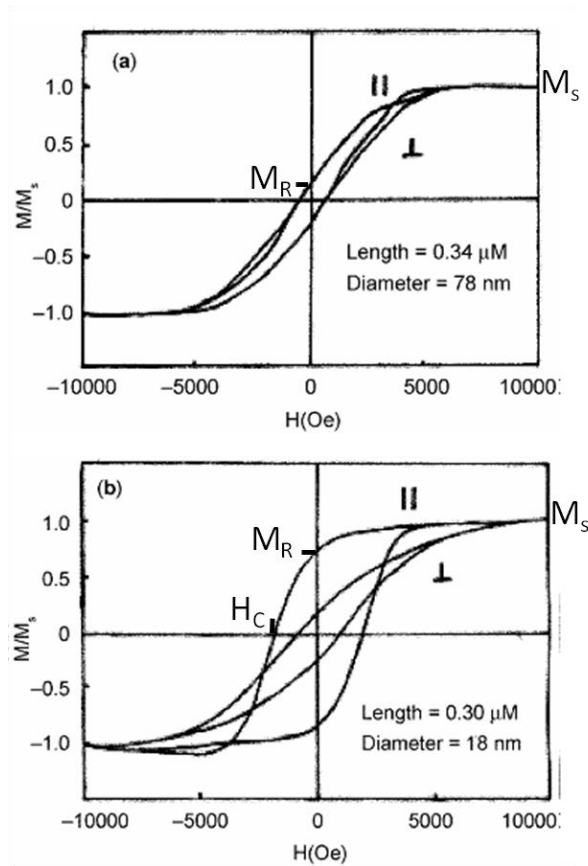


**Figure 2. 1.** The variation of squareness of hysteresis loops of Co NW arrays with applied magnetic field ( $H$ ) parallel ( $\parallel$ ) and perpendicular ( $\perp$ ) to the wire axes: (a) NW diameter, 78 nm and (b) NW diameter, 18 nm [2].

It has also been shown that magnetic materials as cobalt (Co), iron (Fe) and nickel (Ni) have higher magnetic coercivity in their NW form compared to their bulk counterparts [5]. The magnetoresistance (MR) behavior (change in electrical resistance upon application of a magnetic field) of NWs has been shown to be also diameter dependent using  $\text{Bi}_{0.85}\text{Sb}_{0.15}$  [6]. Improvements in remanance and coercivity are useful for data storage systems. Therefore, one of the most important application areas of NWs is magnetic data storage systems and Co, Fe and Ni NWs are the most suitable candidates for these applications.

The thermoelectric behavior of NWs also shows differences than their bulk counterparts. Metallic NWs exhibit an increase in the Seebeck Coefficient (induced thermoelectric voltage in response to a temperature gradient in the material) because of their high density of electronic states, which can be explained by quantum confinement effect. It has been also shown that thermopower of the metallic NWs is dependent on a diameter decrease in the NW. Indium antimony (InSb) and Si doped bismuth (Bi) NWs [7,8] and in aluminum (Al) doped zinc (Zn) NWs [9] leads to an increase in thermopower. In another experiment, thermal conductivity of Si NWs is reported to be decreased with a decrease in their diameter, as shown in Figure 2.2. [13]. These properties make NWs applicable to thermoelectric cooling systems and energy conversion devices [11,12].

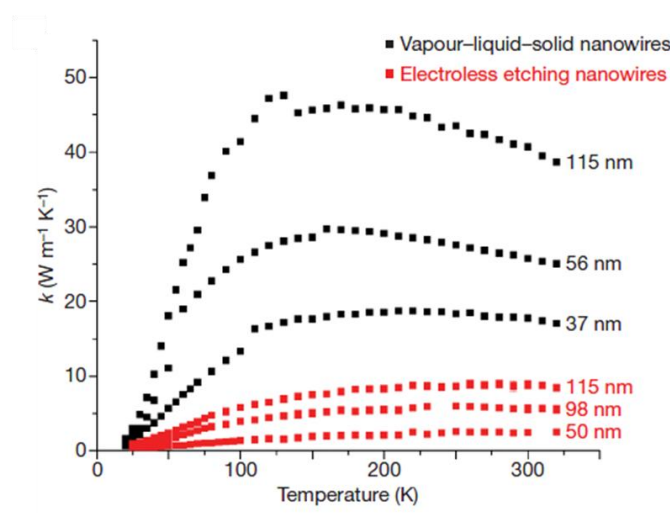


**Figure 2. 2.** Temperature dependent thermal conductivity ( $k$ ) of Si NWs [13].

Electrical properties of NWs are affected by their diameter, surface conditions, crystal structure and crystallographic orientation. There are two types of electrical conduction in NWs, which are diffusive and ballistic conduction [14]. Diffusive conduction occurs when mean free path of an electron is shorter than the NW length. On the other hand, ballistic conduction occurs when mean free path of an electron is longer than the NW length. Therefore, there is no scattering in ballistic type of conduction. In diffusive type of conduction, scattering of electrons occurs and conduction becomes similar to that in bulk materials. Therefore, electron transfer in NWs depends on wire diameter, carrier mean free path and de Broglie wavelength of electrons. If the diameter of a NW is larger than carrier mean free path and de Broglie wavelength of electrons, electrical conduction occurs similar to that of bulk materials. On the contrary, if the diameter is smaller than the mean free path of carriers; but, larger than de Broglie wavelength of electrons then, the transport mechanism obeys the classical physics laws. However, if the NW diameter is comparable or smaller than the two of these parameters quantum confinement occurs changing density of states (DOS) in other words states in the bands and their dependence on energy. In Figure 1.3 (a-c) discrete DOSs for Ti NWs having diameters lower than 1 nm and continuous DOS for Ti NWs having diameters higher than 1 nm are illustrated.

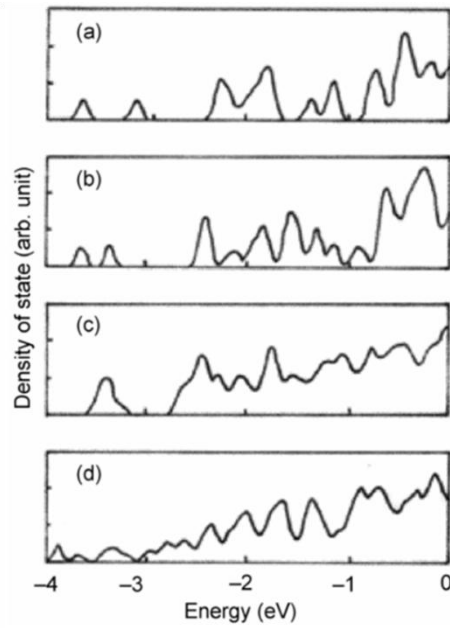


**Figure 2. 3.** DOS of Ti NWs: (a) and (b) wire diameter < 1 nm and (c) and (d) wire diameter >1 nm with 0.05 eV Gaussian broadening [15].

Electrical conduction in NWs also changes with crystal defects. For a perfect NW, conduction paths are larger in number and hence conduction is easier compared to one or two atom defective NWs [16]. Surface conditions could influence scattering and thus change the properties of NWs. NWs are highly used in electrical applications such as junction diodes, memory cells, switches, transistors, field effect transistors (FETs) and light emitting diodes (LEDs).

NWs are ideal candidates for the examination of mechanical properties of a single crystal nanostructure. Mechanical properties of the macroscale crystalline materials depend on their crystal structure and number and type of imperfections. Hall-Petch equation is used for polycrystalline materials correlating the grain size into the yield strength of materials. Since grain boundaries act as obstacles to impede dislocation motion, a fine grained material would have a higher yield strength value as compared to a coarse grained counterpart. However, Hall-Petch equation is valid only down to a certain limit. Beyond ultra-fine grained materials, as the grain size decrease to nanoscale, the yield strength decreases following a reverse Hall-Petch behaviour as

intergrain and grain boundary sliding mechanism becomes dominant in nanoscale. Since the NWs are single crystalline and defect free, the mechanism governing the mechanical behavior of NWs is different. In a study conducted by Demon et al. using Ge NWs, it has been found that as the NW diameter decreases, the maximum strain that can be given to a NW without failure increases. This is due to a decrease in the number of defects in a small volume [17]. It has been found that with decreasing diameter of the NWs, their bending strengths reach to their theoretical fracture strength as in the case of a defect free single crystalline solid. In addition, within the same study it has been found that the elastic modulus of the Ge NWs is independent of their diameter.

NWs present enhanced chemical properties because of their high surface to volume ratio, surface curvature and high number of surface atoms. Their enhanced chemical reactivity makes them ideal candidates for the active elements in chemical sensors. Detection of a desired element with a NW depends on the resistance capacitance change of the NW. In Figure 1.4, change in the current and the conductivity of an individual  $\text{In}_2\text{O}_3$  NW through the absorption of protein molecules onto their surface can be clearly seen.

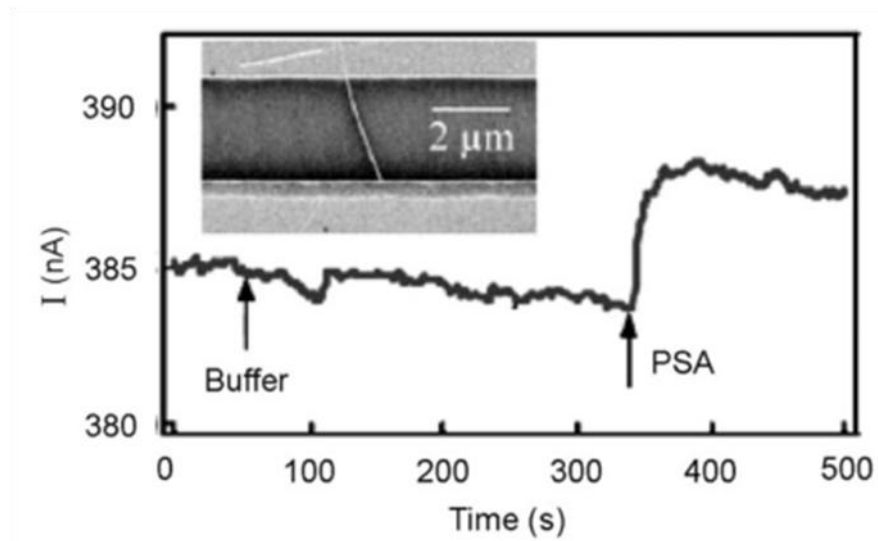


**Figure 2. 4.** The change in current as a function of time for an individual  $\text{In}_2\text{O}_3$  NW when exposed to buffer and protein specific antigen (PSA). Inset: SEM image of the single  $\text{In}_2\text{O}_3$  NW sensor device [18].

Optical properties of NWs have been also widely investigated. Metallic NWs show enhanced plasmon scattering characteristics. For silver (Ag) nanostructures, it has been shown that two plasmon bands occur when the zero dimensional Ag nanoparticles begin to form one dimensional structures [19]. Photoluminescence (PL) peak position and thus the bandgap of semiconductor NWs increase as their diameter decreases, confirming the quantum confinement effect. NWs also exhibit non-linear optical behavior; therefore, their light sensitivity has been one of the frequently investigated fields. Even if their diameter is much larger than their quantum confinement size, NWs show greater light sensitivity compared to their bulk counterparts, which is because of their large surface to volume ratio. Moreover, since dimensions of NWs are comparable to the wavelength of the incident light, enhanced light scattering, which leads to optical birefringence and optical funneling (waveguiding effect) are expected. Vertically stacked arrays of NWs show significant reduction in reflectance. As they are surrounded by air their low refractive index acts as an antireflection coating. Moreover, their large surface area enables very high density of surface states. These surface states create Fermi energy pinnig

near the surface forming a depletion region. Therefore, photogenerated electrons and holes can be separated easily leading to a prolonged photocarrier lifetime. Thus, high photoconductive gain of NWs could be attributed to their high density of surface states leading to an ease in charge separation and their defect free single crystalline structure enabling high carrier mobility. The outstanding properties of NWs lead to a number of applications such as, LEDs, lasers, solar cells, optical interconnects, single photon detectors and image sensors.

Because of their unique properties Ge NWs have been used in many different devices as can be seen in Figure 2.5 (a-e). The most investigated devices with Ge NWs are field effect transistors (FETs). Since now many groups have fabricated Ge NW FETs [1, 20, 21, 22]. The low effective mass of electrons and holes in Ge result in higher carrier mobility making Ge a very important candidate for FETs. Other Ge NW device applications include but not limited to photoresistors [23], diodes [24, 25], field emitters [26] and photodetectors [27, 28, 29].

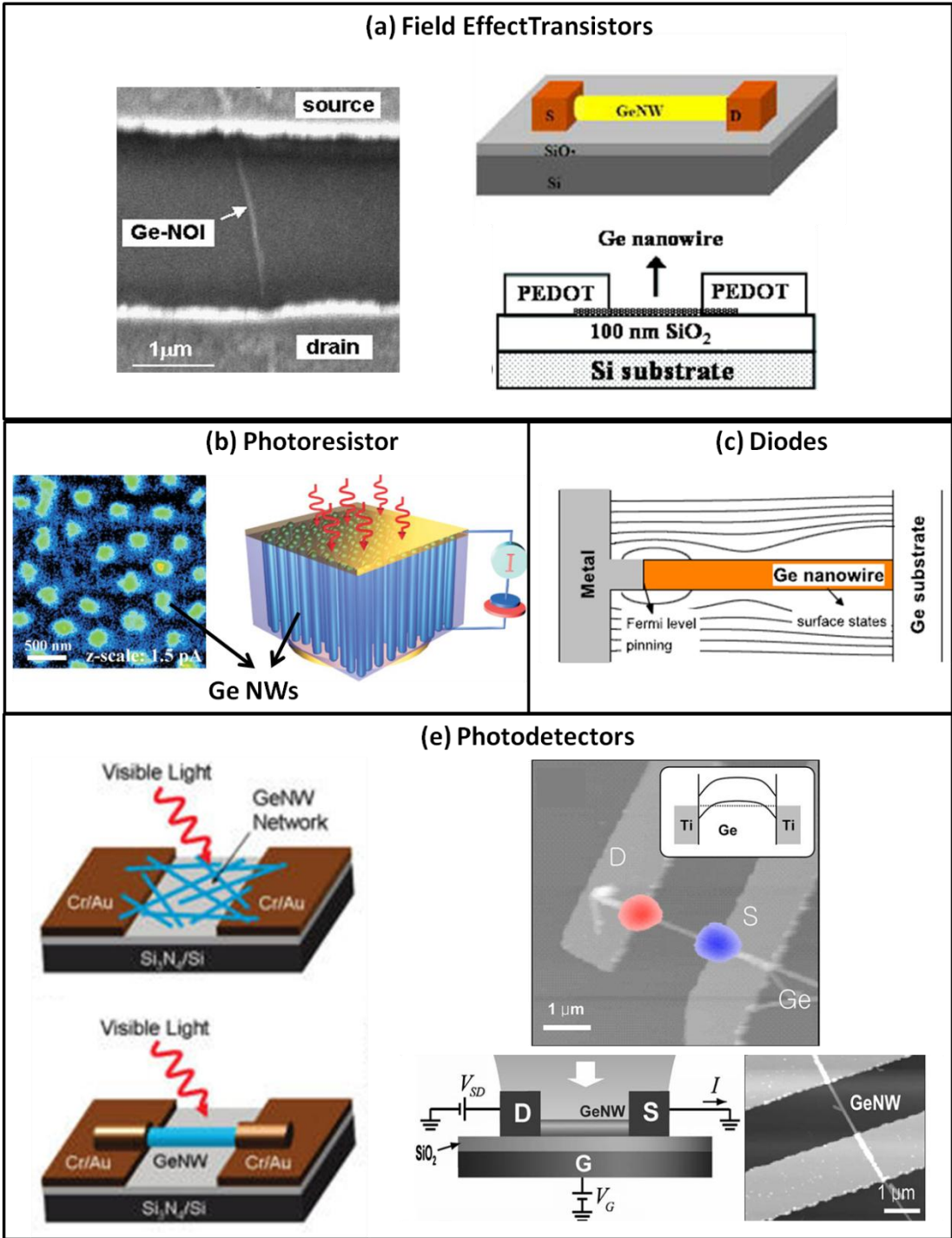


**Figure 2. 5.** Applications of Ge nanowires.

## 2.1.2 Conventional Ge NW Synthesis Methods

Synthesis approaches of Ge NWs can be divided into two groups, which are top-down and bottom-up, as can be seen in Figure 2.6. Bottom-up approaches can be further divided into two groups that are solution phase and gas phase synthesis. Solution phase methods enable lower synthesis temperatures and simpler equipments compared to gas phase methods [30]. Gas phase synthesis methods use vapor-liquid-solid (VLS) growth mechanism. The principle behind all of these techniques is the decomposition of a Ge precursor and the consequent supply of Ge containing species to feed a proper catalyst to eventually form the Ge NWs. Solvothermal and super critical fluidic methods are solution phase methods; while laser ablation, vapor transport and CVD are gas phase methods. All of these methods are briefly described in this section.

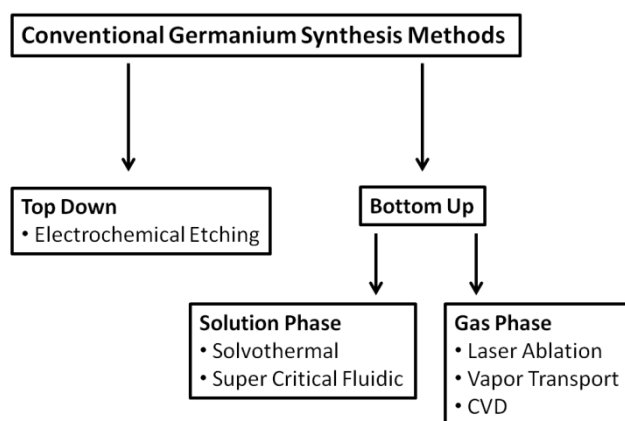


**Figure 2. 6.** Conventional Ge NW synthesis methods.

### 2.1.2.1 Top-down Methods

#### 2.1.2.1.1 Electrochemical Etching

The electrochemical etching method was first used for Ge NWs by Fang et al in 2006 [31]. In this method, Ge NWs were fabricated from a single crystalline n-type Ge in a hydrochloric (HCl) containing aqueous electrolyte in an electrochemical double cell

with a four-electrode configuration. Potentiostatic or galvanostatic conditions were controlled by a custom-built potentiostat using an Ag/AgCl reference electrode and a platinum (Pt) counter electrode. The temperature change was reported to be very effective on NWs; therefore, the temperature during synthesis was kept strictly at 14 °C. First of all, a homogenous nucleation was obtained and after that, macropores were etched at different etching currents. Since the band gap of Ge is narrow, the leakage current through pore walls was much higher than that used for electrochemical etching of Si. The as synthesized Ge NWs had diameters ranging from 50 to 500 nm and lengths up to several hundred micrometers.

### **2.1.2.2 Bottom-up Methods**

#### **2.1.2.2.1 Solvothermal Synthesis**

Supercritical fluidic method was firstly applied by Heath and Françoise in 1993 [32] for the synthesis of Ge NWs. In this method, mixed germanium tetrachloride ( $\text{GeCl}_4$ ) and phenyl- $\text{GeCl}_3$  with sodium (Na) precursors were mixed and the mixture was heated up to 275 °C, while the pressure was maintained at 100 atm. During the reaction,  $\text{GeCl}_4$  and  $\text{GeCl}_3$  was reduced by Na in an alkane solvent. The reaction took about 2-8 days. The synthesized Ge NWs were polycrystalline, had diameters between 7-30 nm and their length was 10  $\mu\text{m}$ . However, these NWs especially bigger ones consisted of many defects; while small ones (2-5 nm) were defect free.

#### **2.1.2.2.2 Supercritical fluidic synthesis**

This method was first conducted by Korgel et al. in 2001 [33]. Alkanethiol-capped gold (Au) nanocrystals were used as catalyst and dispersed in cyclohexane. The Ge precursors were tetraethylgermane (TEG) and diphenylgermane (DPG). A stock solution containing 1:2000 molar ratio of Au:Ge was prepared under nitrogen atmosphere. Then the mixture was diluted and used as the injection solution. The reaction took place at a temperature of 350-400 °C and under 13.8-38 MPa pressure.

The final product was single crystal Ge NWs with diameters ranging between 10-150 nm. The growth mechanism was suggested as vapor-liquid-solid (VLS), which was first discovered by Wagner and Ellis in 1964 [34]. In this mechanism, the precursor materials decompose and release reactive Ge species. These species feed the Au catalyst, forming an alloy. As this alloy saturates, it reaches to a eutectic composition and the alloy liquidifies. Further feeding of Ge species causes supersaturation; leading to precipitation of Ge around the circumference of the catalyst particle, which then grows as a NW. The VLS mechanism will be discussed later in detail. The comparison of DPG and TEG has been conducted and results are shown in Figure 2.7. DPG was found to be superior to TEG, because of its faster deposition rate. High concentrations of both precursors resulted in the production of dense NWs, while low concentrations resulted in aggregated particles. Ge NWs were immediately oxidized upon exposure to atmosphere at the end of the reaction.

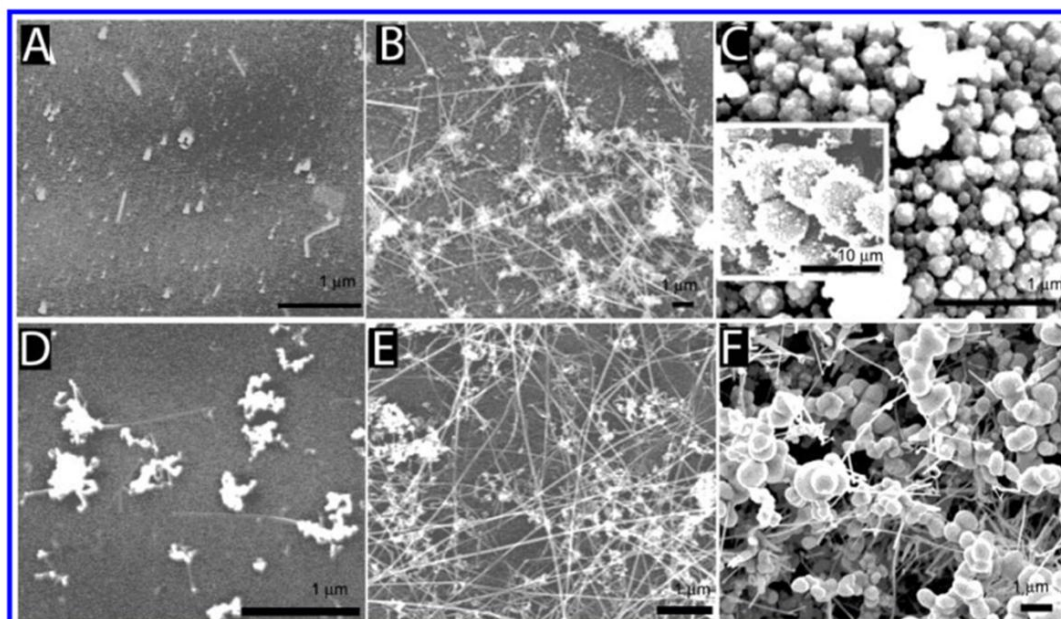


**Figure 2. 7.** HRSEM images of Ge NWs grown by Korgel et al. at 38 MPa for 20 min using TEG at (a) 300, (b) 400, (c) 500 °C and using DPG at (d) 300, (e) 400 and (f) 500 °C [33].

### **2.1.2.2.3 Laser Ablation**

This method was developed by Lieber et al. in 1998 and used to synthesize Si and Ge NWs [35]. Later on, the laser ablation method has been used for the synthesis of various semiconductor NWs such as gallium nitride (GaN) and gallium arsenide (GaAs). This method was improved in order to overcome the equilibrium size of the Au clusters, which determines the NW diameter. A pulsed laser (frequency-doubled Nd–yttrium-aluminum- garnet laser (wavelength, 532 nm)) was used to create nanometer sized Au clusters. In this method, laser was directed onto a target containing Ge precursor,  $\text{Ge}_{0.9}\text{Fe}_{0.1}$  and seed materials at a temperature and a pressure of 820 °C and 300 torr, respectively. Following the ablation, the precursor and seed materials formed an alloy and NWs grew from these alloys via VLS mechanism. The diameter of the resulting NWs was uniform and very small (3-9 nm). The NWs were single crystalline without any amorphous coating; but they contained twinning on their (111) planes.

### **2.1.2.2.4 Chemical Vapor Deposition**

Chemical vapor deposition (CVD) method uses gas precursors, such as germane ( $\text{GeH}_4$ ), digermane ( $\text{Ge}_2\text{H}_6$ ) and tetraethylgermane ( $\text{Ge}(\text{C}_2\text{H}_5)_2$ ). In this method, a vacuumed tube furnace with temperature and pressure control is used. Ge gas precursors are supplied into the system at an elevated temperature, while substrates are placed in the tube at the beginning of the experiment. Ge species in the gas phase forms a eutectic solution with the catalyst on the substrate. When the solution supersaturates, the Ge NWs nucleate and grow. By changing temperature and pressure, the NW length and diameter can be controlled in this method. Therefore, it allows the synthesis of NWs with desired dimensions.

The first Ge NW synthesis using CVD method was accomplished by Wang et al.[33] in 2002. In the synthesis,  $\text{GeH}_4$  gas was used as the precursor. The experiments were

carried out a temperature of 275 °C under atmospheric pressure. The resulting NWs were found to be single crystalline in nature with a growth direction of  $\langle 110 \rangle$ . The average diameter of the NWs was 23 nm, while their length was found to be up to ten micrometers, as shown in Figure 2.8. In another study, individual nanoseed patterned Au particles as catalyst were used and individual NWs from those Au nanoparticles were synthesized.

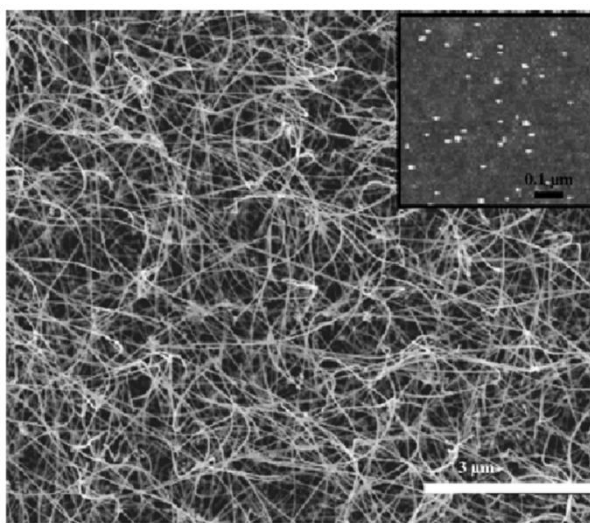


**Figure 2. 8.** SEM image of Ge NWs synthesized by Wang et al. Inset shows an atomic force microscopy (AFM) image of Au nanoclusters on Si substrate [33].

After that, several groups synthesized Ge NWs using CVD method [36, 37, 38]. Dailey et al. used  $\text{Ge}_2\text{H}_6$  instead of  $\text{GeH}_4$  as precursor gas and synthesized Ge NWs at lower pressures of  $4 \times 10^{-5}$ ,  $10^{-2}$  torr [39]. In this study, nanopillar growth was observed at lower pressures while with an increase in pressure NW formation was reported.  $\text{Ge}(\text{C}_5\text{H}_5)_2$  gas precursor was used by Mathur et al. and iron (Fe) foils were used as substrates [40]. Resulting NWs had no residual catalyst particles at the end of the reaction. Average diameter of the NWs was found to be between 15-20 nm, while their length was between 25-40  $\mu\text{m}$ .

Parametric studies based on temperature, pressure and incoming gas flow was carried out in many studies [41,42]. Diameter and shape of the NWs were found to be controlled in CVD method by changing these parameters.

#### **2.1.2.2.4 Vapor Transport**

In vapor transport method, the principle is to obtain a Ge vapor from solid precursors by several different reactions and then to transfer this vapor through the substrate, the NW growth occurs by VLS method. Different groups reported on the use of various precursors such as Ge, Ge and GeI<sub>4</sub>, Ge and GeO<sub>2</sub>, GeO<sub>2</sub> and C, to obtain Ge vapor.

This method was pioneered by Omi et al. in 1997 [43]. In this study, molecular beam epitaxy method was used to grow wire-like Ge islands. The substrate was Si (113) and the growth temperature was 400-500 °C. The Ge vapor was produced from Boron Nitride Knudsen cell and then transferred to the Si substrate. The growth occurred by self assembly of Ge atoms because of strain relief with the same crystal orientation of Si (113) substrate. However, as synthesized NWs were polycrystalline in nature and were constrained on the substrate.

After that, Wu et al. used GeI<sub>4</sub> and Ge powders as precursor materials and synthesized Ge NWs with higher quality [44]. A quartz sealed tube was used in the experiments. They placed 50-200 nm Au coated Si substrates in the cold end of the tube for the collection of NWs, while mixed Ge and GeI<sub>4</sub> powders were placed in the hot zone. The furnace was heated to 1000-1100 °C and the pressure was maintained at 30 mtorr. During the experiment, the quartz tube was flushed with nitrogen gas. Resulting NWs had diameters between 5-300 nm and were several hundreds of micron in length. NWs were single crystalline in nature with a [111] growth direction. A heat treatment process was used to reduce the size of the NWs and make them more uniform. For this purpose, NWs were sealed in an evacuated quartz tube,

which was heated to 800 °C for an hour. This reduced the average diameter of the NWs to 16 nm.

In the same year, Gu et al. synthesized Ge NWs using Ge powder [45]. In this method, Ge vapor was obtained through the evaporation of Ge powder at 950 °C, which was then transported towards the catalyst coated Si substrate. Both Au thin film and Au nanoparticles were used as catalyst. Thickness of the thin Au film was 2 nm, while the average size of the Au nanoparticles was 10 nm. Tube furnace was used for the experiments and Ge powder and Si substrate were placed in the hot and cold zone, respectively. Ar was used as the carrier gas. The reaction carried out at 1.2 mbar for 30 minutes under 30 sccm (standart cubic centimeter per minute) Ar gas flow. The diameters of the as-synthesized NWs using Au thin film were 20-180 nm; while they were 20-45 nm using the Au nanoparticles. The growth direction of the NWs was determined to be [111] and they were single crystalline in nature. The surface of the NWs was covered with a 1-2 nm thick oxide layer. Field effect transistors (FET) was fabricated from the as synthesized NWs in order to determine the electrical properties of NWs.

Mei et al. used a different substrate, porous anodic alumina template for the synthesis of Ge nanorods [46]. Using this method, it was possible to synthesize large amounts of Ge nanorods in a single run. Small Ge tablets and GeO<sub>2</sub> powder was used as the precursor materials. The powder mixture was placed in a quartz tube and the alumina template was placed 10 cm downstream from the powder mixture. The pressure of the quartz tube was maintained at 10<sup>-3</sup> Pa during the experiment. The Ge and GeO<sub>2</sub> mixture was heated up to 1100 °C for 3 hours and remained in vacuum for 10 hours. The diameter of the resulting nanorods was measured to be 50 nm and their growth direction was determined as [220].

A few years later, Yan et al. used GeO<sub>2</sub> and C powders for the synthesis of one dimensional Ge and GeO<sub>2</sub> nanostructures on the same substrate [47]. In this work, GeO<sub>2</sub> and C powder mixture and 9 nm Au coated Si substrate were placed into the hot and cold zone of the furnace, respectively. The temperature of the furnace was

maintained at 1000 °C for about 1 hour under 300 sccm Ar gas flow. The substrate temperature varied between 300 to 600 °C. Both white and brown products were obtained on the substrate, which were then identified as GeO<sub>2</sub> and Ge, respectively. GeO<sub>2</sub> NWs were synthesized at 500-600 °C, while Ge NWs were synthesized at relatively lower temperatures of 300-400 °C. The growth direction of the Ge NWs was determined to be [111]. An SEM image of Ge NWs synthesized in this work is provided in Figure 2.9. At the hot zone, GeO<sub>2</sub> powder was reduced with C forming Ge gas. Since the melting temperature of Ge is much lower than that of GeO<sub>2</sub>, Ge gas was carried through the cold zone of the furnace over the Au coated substrates and led to the growth of NWs.

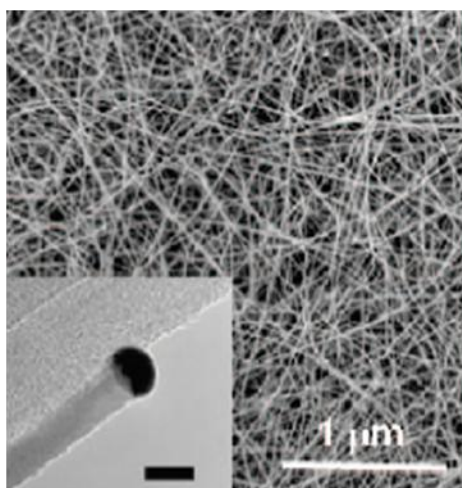


**Figure 2. 9.** SEM image of Ge NWs synthesized by Yan et al. Inset is a TEM image of a single Ge NW capped with Au catalyst [47].

## 2.2 Experimental Details

### 2.2.1 Synthesis of Ge NWs

Prior to the experiments, all glassware and Si substrates to be used in the experiments were thoroughly cleaned. The cleaning procedure began with a rough mechanical

cleaning with a powder precision cleaner. After that, the glasswares were washed with dilute nitric acid ( $\text{HNO}_3$ ) solution and then rinsed in pure water in order to get rid of the acidic solution. Right after, they were rinsed in a dilute sodium hydroxide ( $\text{NaOH}$ ) solution and again they were cleaned with pure water. Following these steps, the glasswares were consecutively sonicated in acetone, isopropanol and deionized water, respectively, for 10 minutes each. All the chemicals used in the experiments were purchased from Sigma Aldrich and used without further purification.

For all experiments, one side polished (100) Si wafers were used as the substrates. Before the synthesis of the Ge NWs, a 2 nm thick Au thin film layer was deposited on the Si substrate using a physical vapor deposition (PVD) setup. During this procedure, bulk Au (99.98 %) tablets were placed in a tungsten (W) holder and vaporized with resistive heating in a vacuum chamber. The pressure inside the chamber was kept at  $10^{-7}$  torr during the evaporation process. A 10 cm circular Si wafer was placed above the Au tablets. Current of the W holder increased slowly to 80 Amp. At that current Au tablet vaporized and Au atoms condensed on the cold Si substrate forming a thin Au layer. The substrate was rotated constantly during the coating procedure in order to obtain a uniform coating. When desired 2 nm thickness was reached (read through a thickness monitor) shutter of the system was closed and current of the holder decreased slowly.

The 2 nm Au coated Si substrates was then placed in the horizontal vacuum-tube furnace to synthesize Ge NWs. In Figure 2.10 (a) and (b) a schematic and actual photograph of the CVD setup used in the experiments are shown, respectively. At the center of the system, there was a horizontal tube furnace which could be heated up to 1100 °C. A quartz tube was inserted inside the furnace as a reaction chamber. One end of the quartz tube was connected with the vacuum system, while the other end was connected with the argon (Ar) and oxygen ( $\text{O}_2$ ) gas inlets. Two flowmeters was used to send Ar and  $\text{O}_2$  gases into the system. There were two kinds of pumps in the system. One of them was a mechanical pump to decrease the pressure down to  $10^{-2}$  mbar and the other one was a turbo pump to further decrease pressure below  $10^{-5}$

mbar and to clean the system from residual  $O_2$ . A smaller second tube was placed inside the quartz tube in order to better control the Ge gas flow. Whole system was controlled with a computer in order to increase reproducibility.

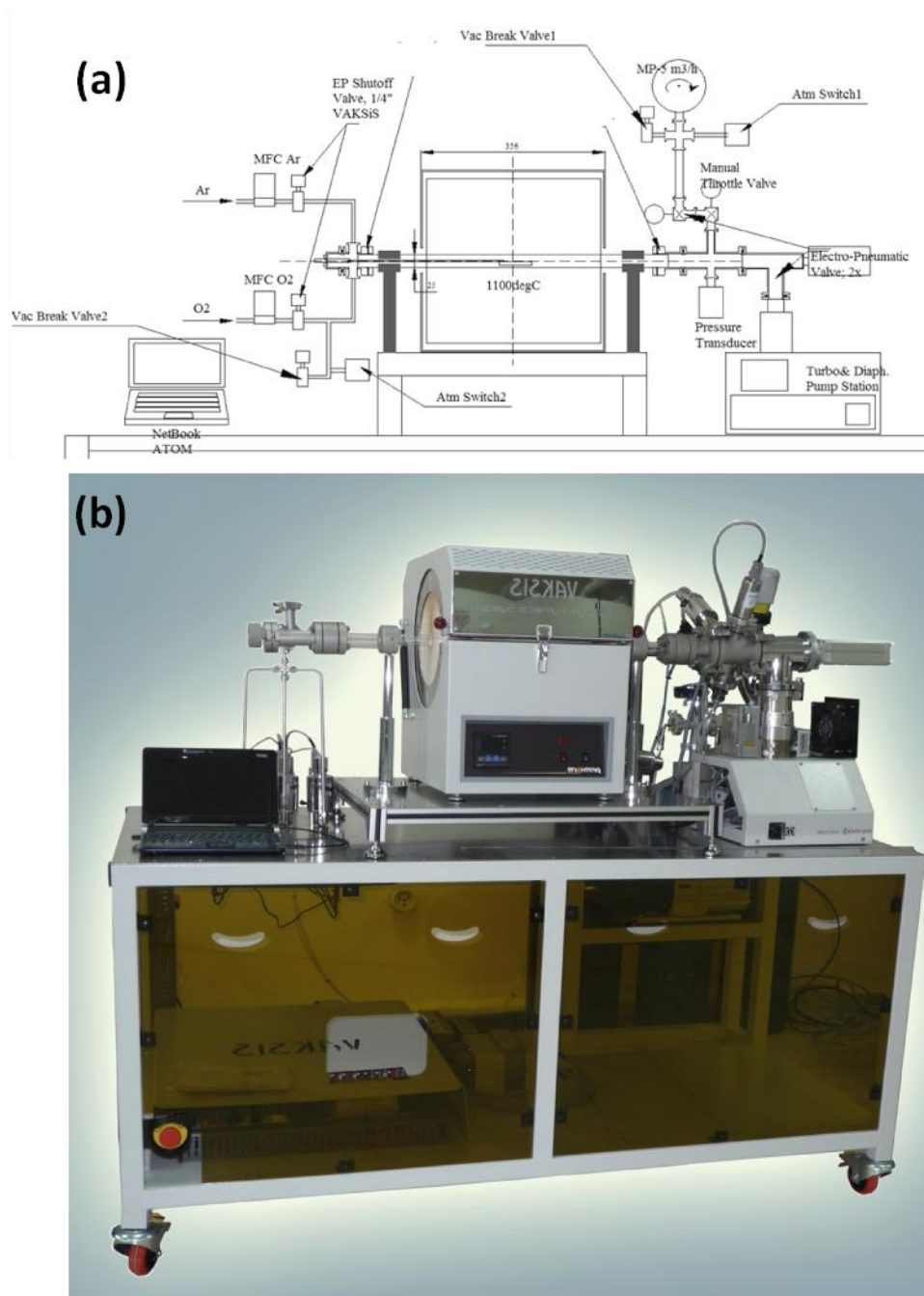


**Figure 2. 10.** (a) Schematic and (b) photograph of chemical vapor deposition system used in this study.

In a typical experiment, powder precursors were placed in the hot zone of a small quartz tube and Au coated Si substrate was placed in the cold zone (details of the synthesis temperature and pressure values are given below according to the precursor types) as shown in Figure 2.11 (a). Then the system was vacuumed down to  $10^{-5}$  mbar in order to clean residual oxygen. After that, Ar gas flow (50 sccm) was supplied to the system and desired synthesis pressure was set with a throttle valve. A constant heating rate of 30 °C/ minute was used to heat up the system to desired temperature. As shown in Figure 2.11 (b), when the furnace was heated to 950 °C, temperature distribution inside the furnace was constant and 950 °C, while it reduces gradually down to 700 °C towards the sides of the furnace. This gradual temperature decrease enabled the investigation of different temperatures on the NW growth using the same substrate. System was kept at the reaction temperature for 60 minutes for the growth of NWs. At the end of the growth process, the furnace was cooled down to room temperature under the same pressure and Ar gas flow. Upon cooling the system, substrates were removed from the furnace. A dark brown layer formed by Ge NWs were observed on the substrates.

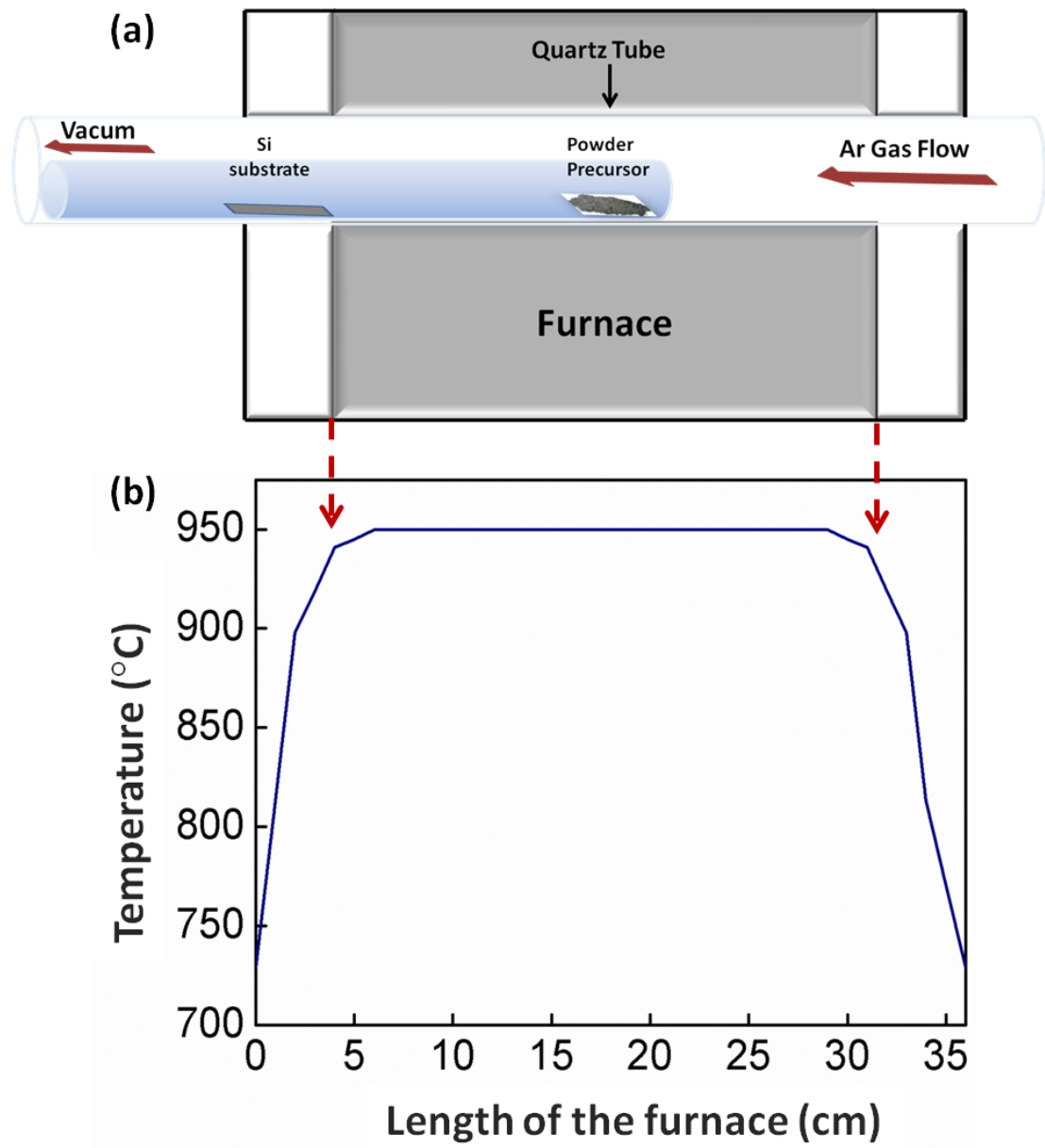


**Figure 2. 11.** (a) Schematic drawing of the experimental set-up in the horizontal tube furnace. (b) Temperature distribution of the furnace, when it is set at 950 °C.

The Ge NWs were grown through VLS mechanism. The VLS mechanism was pioneered by Wagner and Ellis in 1964 [34]. Si whiskers have been synthesized by  $\text{SiI}_2$  dismutation or hydrogen reduction of  $\text{SiCl}_4$ . A small particle of Au was placed on the {111} surface of a Si wafer as the catalyst. Then the substrate was heated to  $950^\circ\text{C}$ . At this temperature, Au-Si alloy droplet was formed decreasing the melting temperature. As more Si was fed in the liquid, it supersaturated and grew as Si wires. The growth direction was identified to be [111]. Catalysts such as Pt, Ag, Pd or Ni have been used and similar results from each have been obtained.

In this work, Ge NWs were synthesized by the same VLS mechanism. The catalyst used was 2 nm thick physical vapor deposited Au thin film. As the Ge vapor was transferred towards the catalyst, small Ge-Au alloy droplets form and NWs grow upon supersaturation of the alloy droplets with Ge according to the Au-Ge phase diagram provided in Figure 2.12.

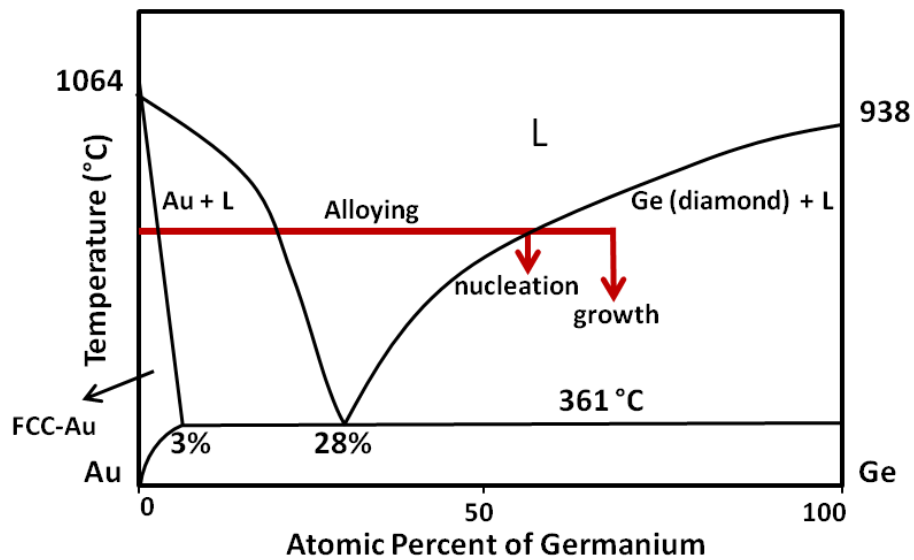


**Figure 2. 12.** Phase diagram of Au-Ge system [33].

There are 3 main steps of VLS growth of Ge NW [48], which are alloying, nucleation and axial growth.

- i. **Alloying step:** Au thin film in Figure 2.13 (a) without Ge vapor stays solid until 900 °C. As temperature increases, it forms small Au islands shown in Figure 2.13 (b). Once Ge vapor reaches the substrate Au-Ge alloy starts to form at about 800 °C, as illustrated in Figure 2.13 (c). This step has been observed by volume increase and decrease of elemental contrast (molecular weight of Ge is lower than Au) of the droplet by in-situ TEM images [48]. Au-Ge alloy is solid in the beginning of the alloying process; however, with an increase in Ge condensation, alloy liquifies.
- ii. **Nucleation step:** After a certain Ge composition, alloy enters biphasic region of the Au-Ge phase diagram, as can be seen in Figure 2.12. At this point, alloy consists of a solid Ge and liquid Au-Ge phases as can be seen in Figure 2.13 (d). At 800 °C and around a Ge concentration of 40%, nucleation starts to form from the supersaturated alloy. During nucleation droplet alloy consists of 50-60 % Ge. This could be observed from the volume change of the alloy.
- iii. **Axial growth step:** Nucleation of a solid Ge on the liquid alloy forms a solid-liquid interface. Dissolved Ge atoms in the liquid alloy diffuse through the interface instead of forming secondary nucleations as the energy barrier of a liquid solid interface is lower than the energy barrier necessary to form a new nucleus. Therefore, other nucleation probabilities are suppressed and no other nucleation occurs. By this mechanism, Ge crystal amount increases and nucleus grows as a NW, as shown in Figure 2.13 (e). As temperature decreases, the droplet on the NW solidifies inhibiting the growth process.

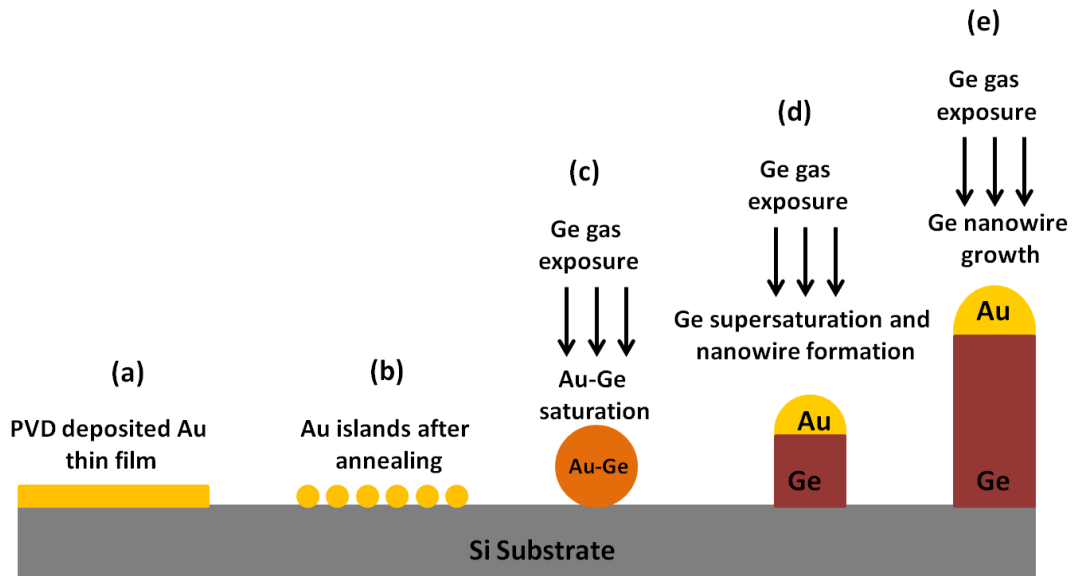
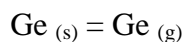


**Figure 2. 13.** Schematic representation of the Vapor-Liquid-Solid (VLS) growth of Ge NWs.

### Ge powder

10 mg Ge powder (99.999 %) is used for the synthesis of Ge NWs. Temperature of the furnace was kept at 950 °C and Si substrate was placed within the temperature range of 850-950 °C. Pressure of the system was kept between 5-200 mbar. When the system reached 950 °C, following reaction occurs:

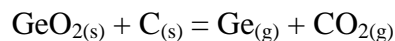


Then, Ge gas was carried towards the Si substrate and led to the growth of NWs.

### GeO<sub>2</sub>+ C powder mixture

25 mg GeO<sub>2</sub> (99.998 %) and 5 mg C powder was mixed in a mortar and placed in the hot zone of the furnace. Temperature of the furnace was 1000 °C and Au coated Si substrate was placed within the temperature range of 800- 900 °C. Pressure of the

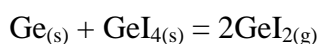
system was kept between 5-200 mbar. When the system reached 1000 °C, following reaction occurs:



Resulting Ge gas was carried towards the Si substrate and led to the growth of NWs.

### **GeI<sub>4</sub> + Ge powder mixture**

30 mg Ge and 7 mg GeI<sub>4</sub> (99.99 %) powder mixture was mixed in a mortar and placed in the hot zone of the furnace. Temperature of the furnace was 1050 °C and Au coated Si substrate was placed within the temperature range of 850- 1000 °C. Pressure of the system was kept between 0.2-200 mbar. When the system reached 1050 °C, following reaction occurs:



Then GeI<sub>2</sub> gas was carried towards the cold region of the substrate and led to the growth of NWs according to the following reaction:



The surface of the as-synthesized NWs had an oxide layer. Oxidation of the surface may occur during the experiment, because of the residual oxygen remained in the quartz tube or when the sample was taken out of the vacuum to the laboratory atmosphere. This insulator oxide layer should be removed from the surface as it inversely effect the electrical properties of the NWs. Therefore, following synthesis the NWs were etched with 5% hydrogen bromide (HBr) solution for 4 minutes and then dried with N<sub>2</sub> gas.

Growth pressure and temperature were critical in the determination of the diameter and morphology of the NWs. Therefore, a parametric study was conducted with temperature and pressure in order to obtain diameter dependence of the NWs on these variables. During the experiments, only one parameter was changed at a time while others were kept constant.

## **2.3 NW Characterization Methods**

### **2.3.1 Scanning Electron Microscope (SEM)**

Final length, diameter and morphology of the NWs were examined with field emission scanning electron microscope (FE-SEM) (Nova NanoSEM 430). The operation voltage was 10 kV for all the samples. SEM analysis for the Ge NWs grown on Si substrates were directly conducted without any extra gold/C coating. As there were height difference between the as-grown NWs on the growth substrates focusing was not uniform everywhere.

### **2.3.2 Transmission Electron Microscope (TEM)**

A JEOL 2010 high-resolution transmission electron microscope (HRTEM) was used to examine the NWs in atomic scale. Growth direction, crystallinity and surface oxide layer characteristics were determined with TEM. The operation voltage was 200 kV. As synthesized NWs were first dispersed in ethanol by a brief 6 seconds sonication and then drop casted onto holey carbon coated 400 mesh copper grids for TEM analysis.

### **2.3.3 X-Ray Photoelectron Spectroscopy (XPS)**

K-Alpha - Monochromated high-performance XPS spectrometer was used for the XPS analysis of the NWs. XPS analysis has been formed to examine existence or removal of the oxide layer on the NWs and to conduct elemental analysis. NWs

grown on Si substrates were directly subjected to analysis without any special sample preparation protocol. In order to compare the effectiveness of oxide removal process, as synthesized and HBr etched NWs were examined. Carbon calibrations of all of the XPS spectra shown in this thesis were done.

### **2.3.4 X-Ray Diffraction Spectroscopy (XRD)**

The crystal structure and phase identification of the Ge NWs was investigated by X-Ray diffraction (XRD) using a Rigaku D/Max-2000 pc diffractometer with Cu K $\alpha$  radiation ( $\lambda = 1.54 \text{ \AA}$ ) operating at 40 kV in the  $2\theta$  range of 20-70 with a scanning rate of  $2^\circ/\text{min}$ .

## **2.4 Results and Discussion**

### **2.4.1 Determination of Synthesis Parameters**

#### **2.4.2 Ge powder Precursor**

SEM images of the synthesized Ge structures at different temperatures and pressures are shown in Figure 2.14 (a)-(c). It has been found that the diameter of the NWs increases with temperature. This effect arises from the coalescence of Au islands, at higher temperatures, increasing the diameter of the NWs. Moreover at higher temperatures diffusion of Ge in larger Au particles becomes possible giving larger diameter NWs. Plots showing the change in the diameter of the NWs with the growth temperature and pressure is provided in Figure 2.15 (a) and (b), respectively. As can be seen in Figure 2.15 (a), diameter of Ge NWs increases from 40 to 120 nm as temperature goes from 750 to 850 °C at 100 mbars of pressure. At the highest temperature region (950 °C) the NW formation was hindered and only micron-sized particles exist for all investigated pressures. This was because at high temperatures, energy of existing atoms is high enough to diffuse and grow in every direction. As temperature decreases, existing nuclei could only grow in the lowest energy direction

favoring the formation of NWs. Pure NW formation was observed at cooler region (750 °C) of the substrates. However, as temperature decreases down to a certain limit, yield of NWs begun to decrease. This effect occurs due to limited diffusion of Ge atoms into the Au islands. At very low temperatures (< 750 °C) Ge atoms could not diffuse enough to saturate Au islands; therefore, NW growth was observed to be initiated only from a few islands. Similar results with temperature were obtained in a study conducted by Yu et al. [49]. At low pressures, more Ge vaporized increasing saturation of Ge vapor in the quartz tube; therefore, NWs with smaller diameters formed. As pressure increases Ge vapor saturation level decreased and diameter of the Ge NWs increased in order to decrease the surface energy. Diameter of the NWs (at 750 °C) increases from 30 to 60 nm as pressure goes from 5 to 200 mbar, as shown in Figure 2.15 (b). In the same Figure, it is also seen that at a pressure and temperature of 5 mbar and 850 °C, respectively, NW formation was hindered. This was because under these conditions, Ge vapor was very far away from equilibrium conditions. Therefore, Ge vapor could not condense to form NWs. However, as pressure increased at constant temperature, micron-sized spherical particles formed. Diameter of these particles increased just like NWs with an increase in pressure to reduce the surface energy.

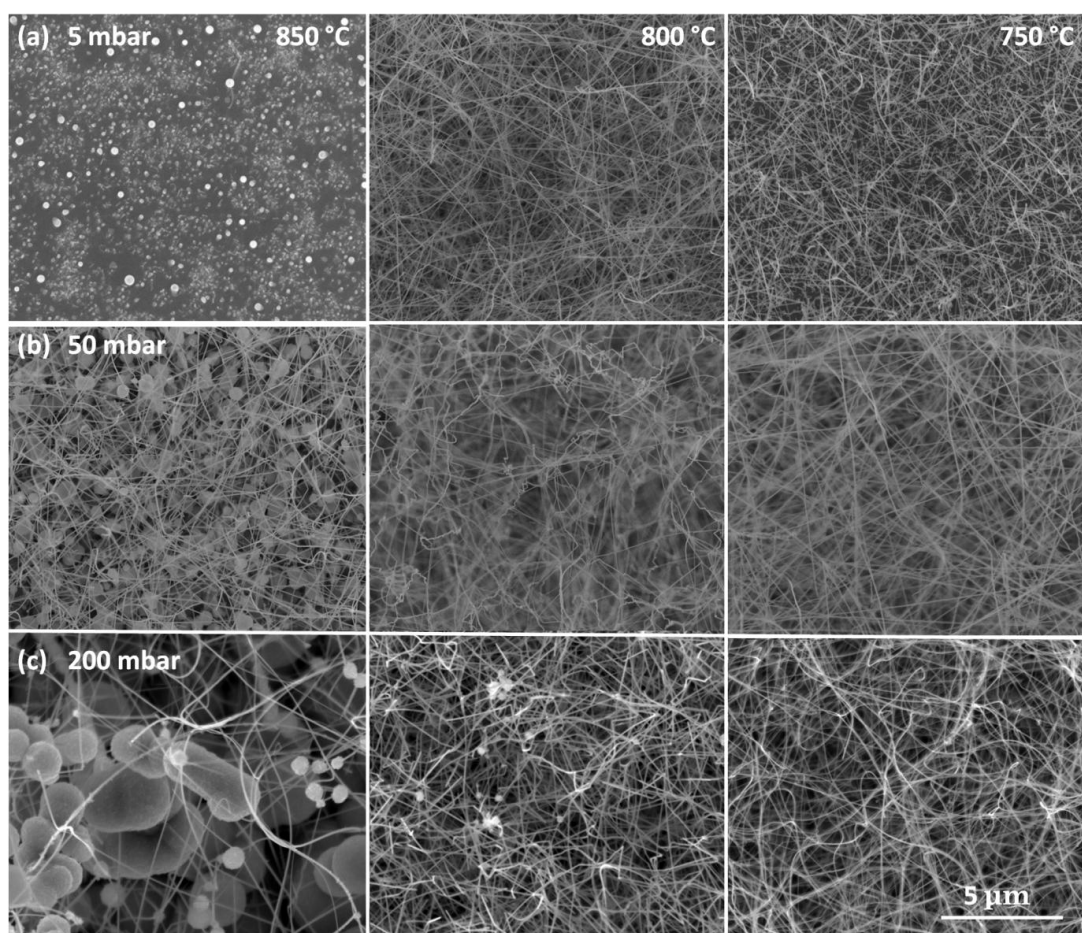


**Figure 2. 14.** SEM images of the synthesized Ge nanostructures using Ge powder under different temperature and pressure conditions (50 sccm Ar gas flow and 2 nm Au catalyst are the same for all of them). Scale bars are all the same.

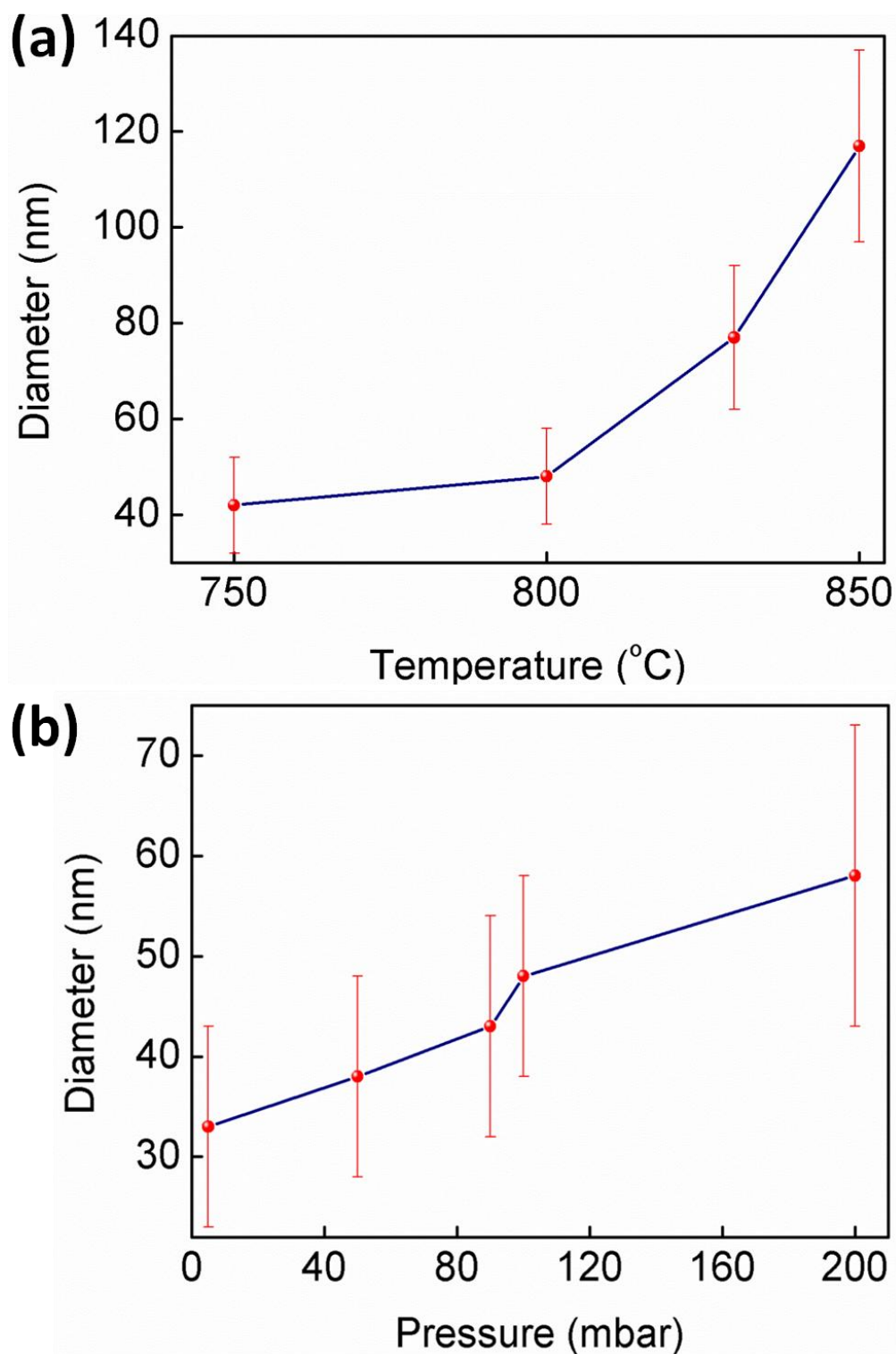


**Figure 2. 15.** Diameter change of Ge NWs synthesized using Ge powder with temperature and (b) pressure.

### 2.4.3 GeO<sub>2</sub> and C powder mixture precursor

The change in the morphology and diameter of the nanostructures with temperature and pressure are shown in Figure 16 (a)-(c). Plots showing the change in the diameter of the NWs with the growth temperature and pressure are given in Figure 2.17 (a) and (b), respectively. Diameter change trends with temperature and pressure were the same with NWs synthesized using Ge precursor. Diameter of the NWs increased from 35 nm to 200 nm, as temperature increased from 800 to 900 °C, as shown in Figure 2.17 (a). Diameter also changed from 30 to 60 nm as pressure increased from 5 mbar to 500 mbar, as shown in Figure 2.17 (b). Micron-sized spherical particles grew at high temperature regions (> 900 °C) and they formed over a large temperature window at low pressures. Optimum temperature leading to NWs synthesis with the highest yield was found to be 800 °C. Below this temperature, NW yield was low due to limited diffusion.

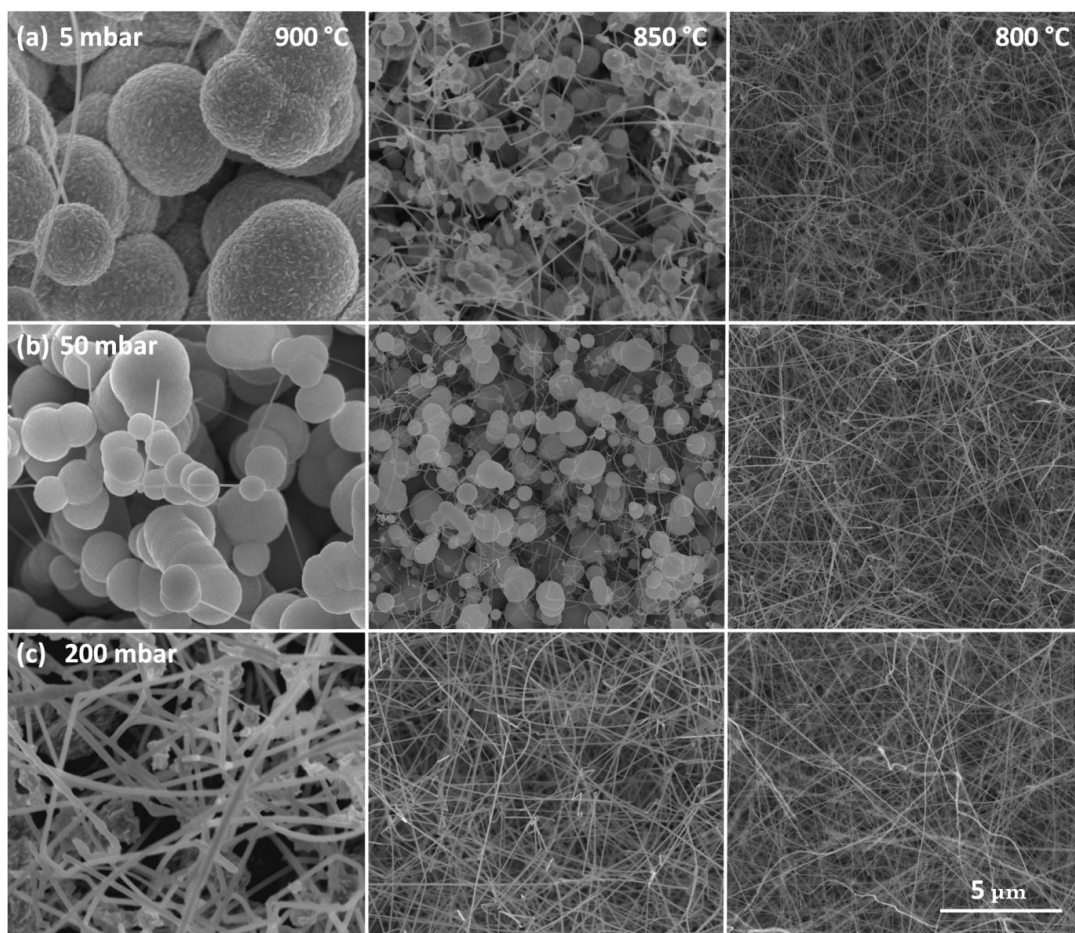


**Figure 2. 16.** SEM images of Ge nanostructures synthesized using  $\text{GeO}_2$  and C powder mixture and at different temperature and pressure conditions. (50 sccm Ar gas flow and 2 nm Au catalyst are the same for all of them). Scale bars are all the same.

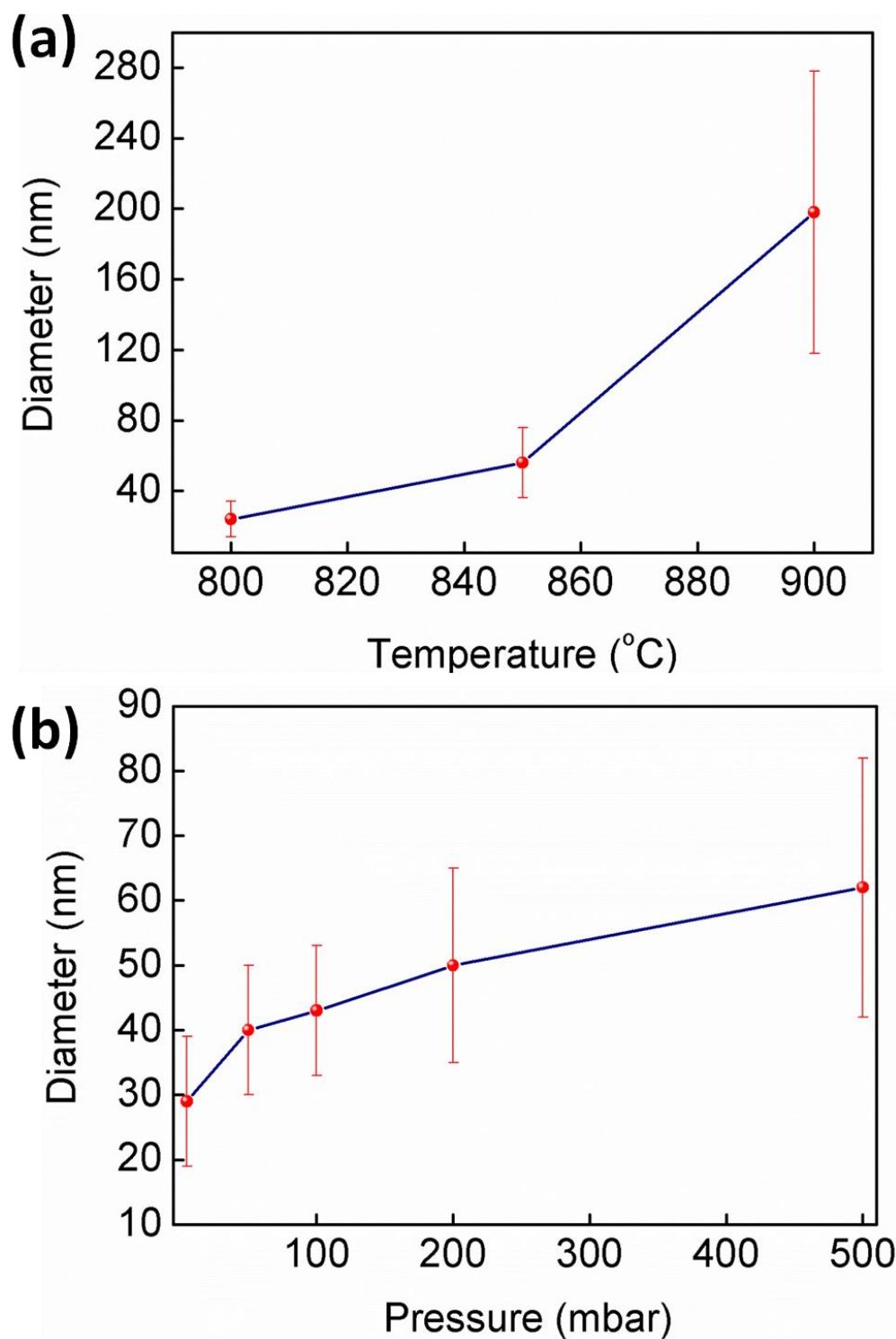


**Figure 2. 17.** Diameter change of Ge NWs synthesized using  $\text{GeO}_2$  and C powder mixture with (a) temperature and (b) pressure.

#### 2.4.4 Ge and GeI<sub>4</sub> powder mixture precursor

The change in the morphology and diameter of the nanostructures that are grown from Ge and GeI<sub>4</sub> mixture precursor with temperature and pressure are shown in Figure 2.18 (a)-(c). Plots showing the change in diameter of the NWs with the growth temperature and pressure are given in Figures 2.19 (a) and (b), respectively. Although the change in diameter of the NWs with temperature and pressure is similar to the results obtained from other precursors, there were some small differences in the structures obtained with GeI<sub>4</sub>+ Ge mixture precursor. At very low pressures (0.2 mbar), no Ge NW formation was observed, as shown in Figure 2.18 (a). Instead of NWs, worm-like structures with very large diameters (> 100 nm) formed. This was because at this pressure, energy barrier for horizontal atomic diffusion could be exceeded easily as the Ge vapor saturation was much higher than its equilibrium value. The length of these structures was shorter than usual NWs, as more Ge vapor was needed for further growth. NW formation was observed for pressures between 10- 100 mbar and more towards the cold region (850 °C) of the substrate. Diameter of the NWs increased from 30 to 45 nm as temperature increased from 800 to 900 °C, as shown in Figure 2.19 (a). It also changed from 30 to 70 nm as the pressure increased from 10 to 100 mbar, as shown in Figure 2.19 (b). At an intermediate (900 °C) temperature, curly or plate like structures appeared between the NWs. This structure was only observed for The Ge+GeI<sub>4</sub> mixture precursor and could be attributed to the low melting point (146 °C) of GeI<sub>4</sub>. As temperature exceeded a particular value ( $\approx$ 1000 °C), only micron-sized particles were observed, instead of NWs similar to the results obtained from other precursors.

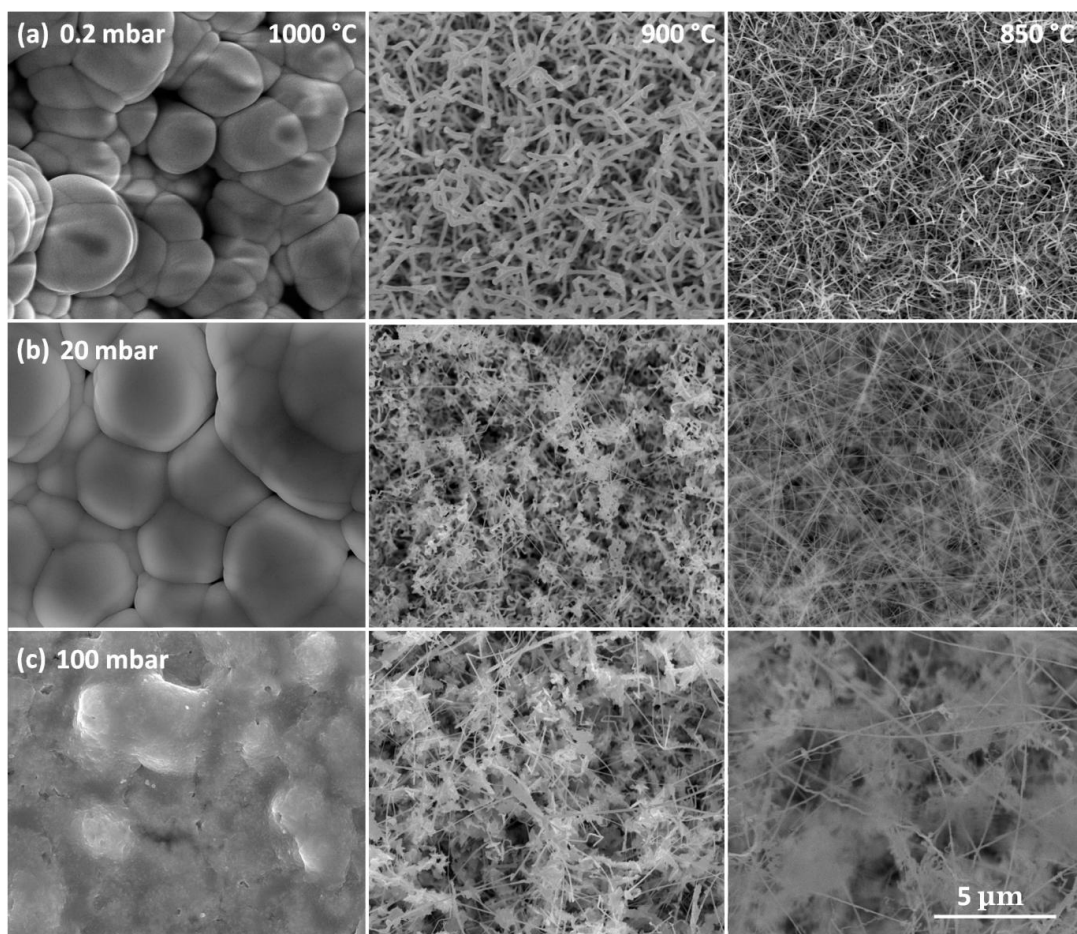


**Figure 2. 18.** SEM images of Ge nanostructures synthesized using  $\text{GeI}_4$  and Ge powder mixture and at different temperature and pressure conditions. (50 sccm Ar gas flow and 2 nm Au catalyst are the same for all of them). Scale bars are all the same.

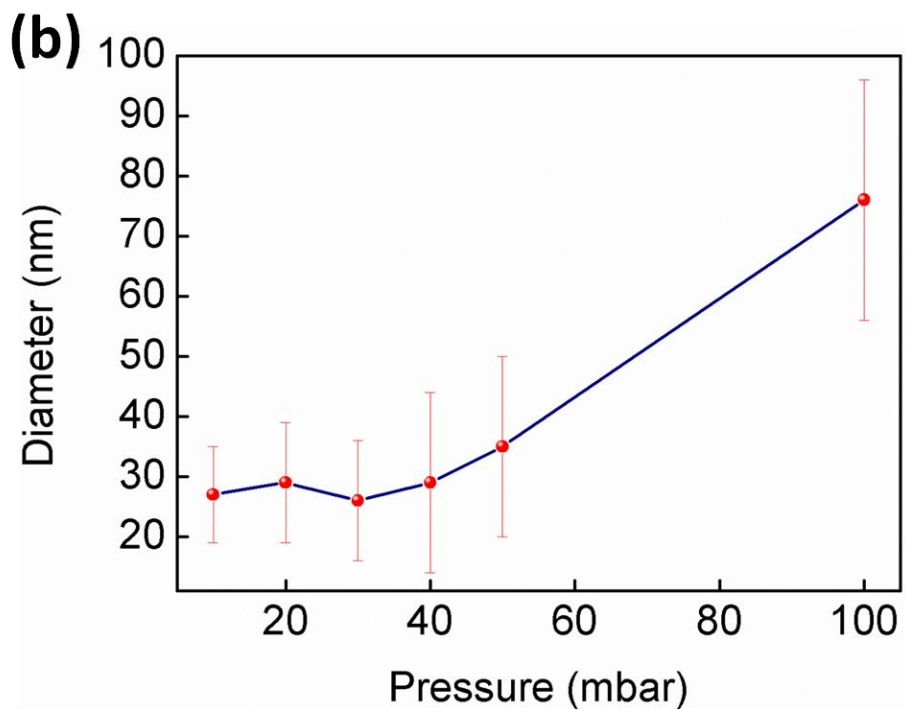
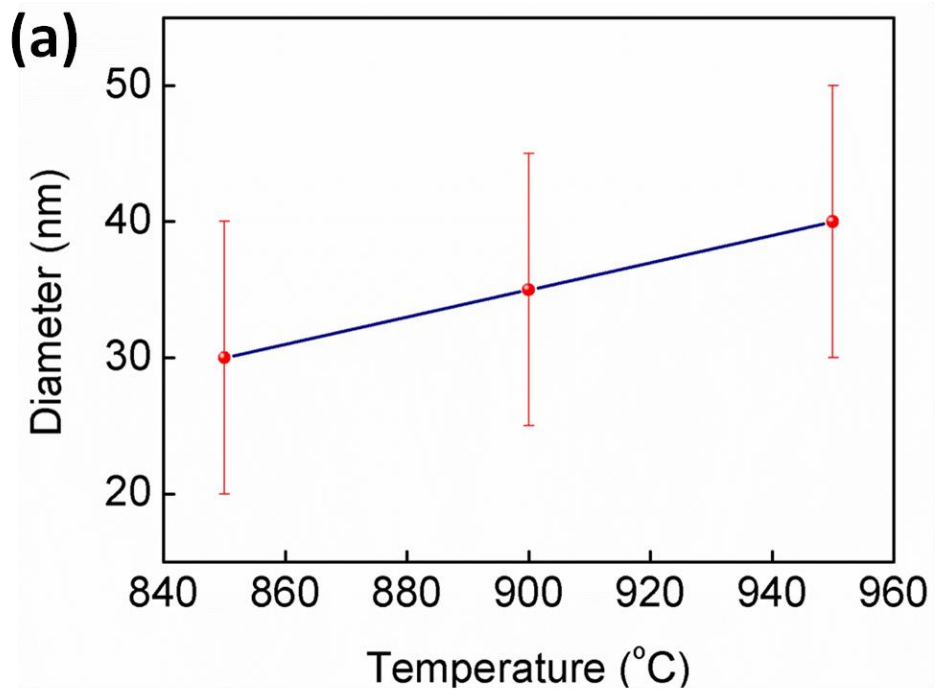


**Figure 2. 19.** Diameter change of Ge NWs synthesized using GeI<sub>4</sub> and Ge powder mixture with (a) temperature and (b) pressure

### 2.4.5 X-Ray Diffraction Results

XRD analysis was conducted in order to determine the crystal structure, lattice constant, nature of the NWs and the presence of contaminants. The XRD pattern of as-synthesized and HBr etched Ge NWs are shown in Figure 2.20. There are three main peaks for etched NWs, which correspond to Ge (111), (220) and (311) planes (JCPDS Card no. 04-0545); however, there are additional peaks for the as-synthesized NWs which correspond to GeO<sub>2</sub> hexagonal structure (marked with asterisk (JCPDS 36-1463)). From the data, Bravais lattice structure and the lattice parameter of the Ge NWs was found to be diamond cubic and 5.63 Å, respectively. These results are in good agreement with the literature [50].

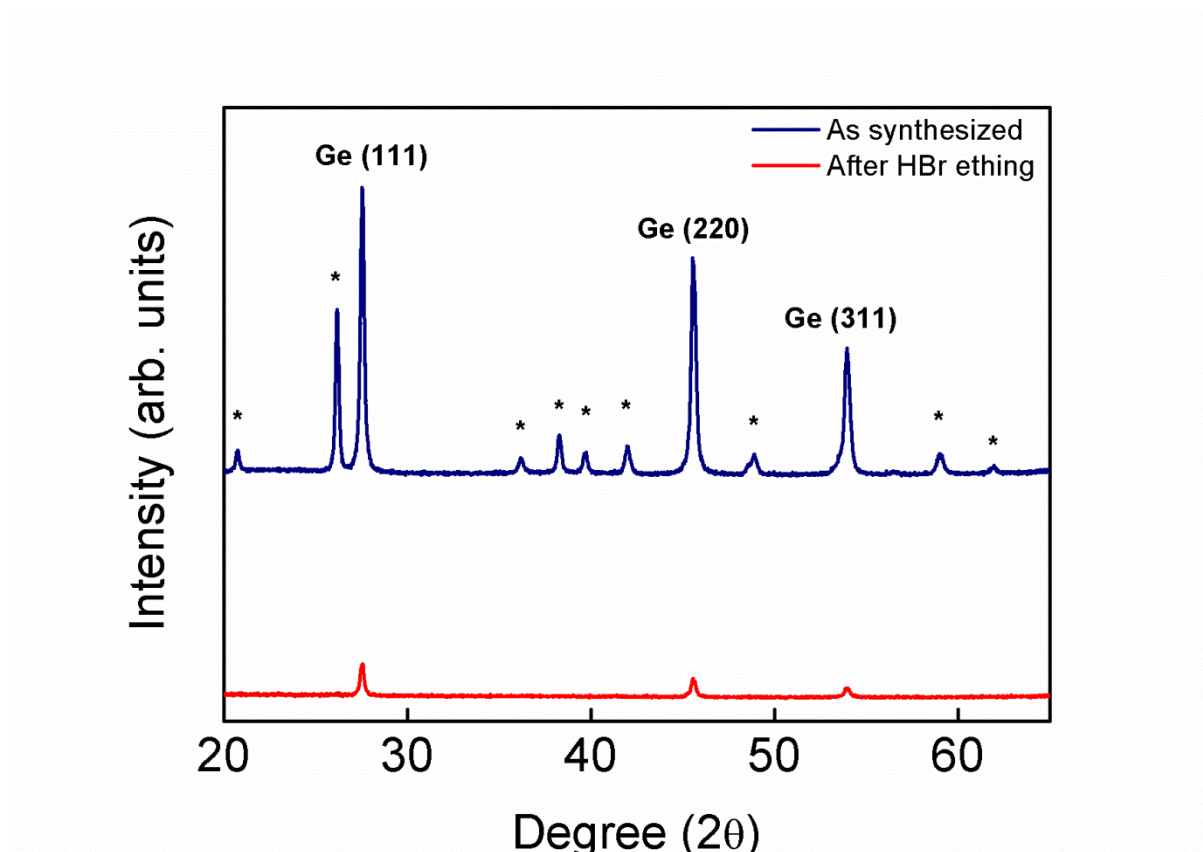


**Figure 2. 20.** XRD spectrum of Ge NWs (synthesized using Ge precursor, under 950 °C and 100 mbar) before and after HBr etching.

XRD spectrum of the etched Ge NWs synthesized using different powder precursors are shown in Figure 2.21. For all cases, Ge NWs are found to be in diamond cubic crystal structure. However, for GeI<sub>4</sub>+ Ge mixture precursor XRD spectra indicates the presence of some amorphous phase. This could be due to, curly or plate-like structures, which grows between the NWs, as described previously.

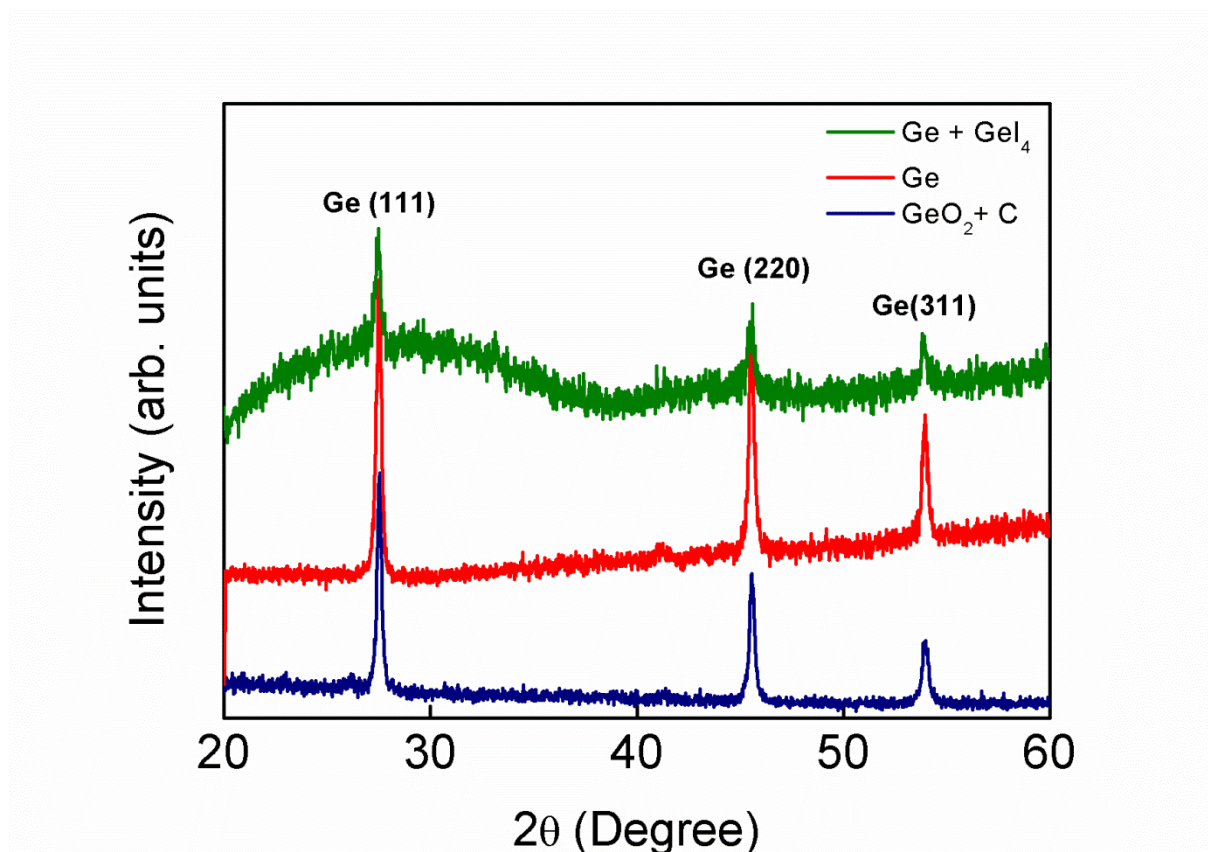


**Figure 2. 21.** XRD spectrum of the etched Ge NWs synthesized with different powder precursors.

#### 2.4.6 XPS Results

XPS analysis was carried out in order to determine the surface properties of the NWs. As explained previously, surface of the as-synthesized NWs had a thick

insulating oxide layer. This insulator layer should be removed from the NWs before the fabrication of photodetectos.

XPS spectra for O-(1s) and Ge-(3d) scan of the as-synthesized NWs using three different powder precursors are shown in Figure 2.22 (a) and (b), respectively. Two signals are apparent in the Ge-3d scan, as shown in Figure 2.22 (a). The smaller signal at a binding energy of 29.1 eV corresponds to Ge-3d binding energy, while the larger signal at 32.8 eV represents the  $\text{GeO}_2$ -(3d) binding energy. Maximum signal values are the same binding energy values for all precursors indicating similar oxidation levels. The penetration depth of the XPS beam is 7-10 nm; therefore, most of the data collected from the sample consists of electrons collected from  $\text{GeO}_2$  surface layer instead of Ge core. Therefore, oxide signals are much higher in intensity compared to the Ge signals. O-(1s) signals at a binding energy of 531.7 eV in Figure 2.22 (b) also confirm the presence of oxygen at the NW surface. The intensity of the data collected from the NWs grown with the Ge powder precursor seems to be highest for both scans. This could be due to higher Ge NW yield obtained within that sample.

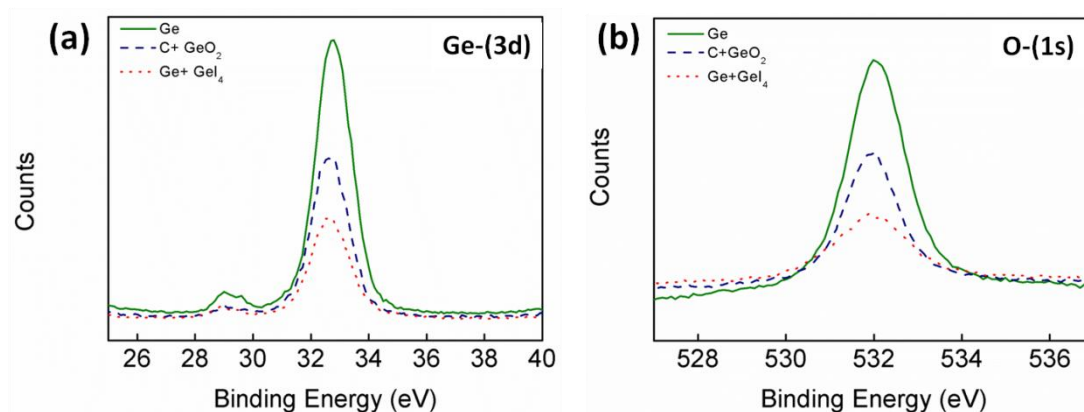


**Figure 2. 22.** XPS spectra for (a) Ge and  $\text{GeO}_2$ -3d signals and (b) oxygen-1s signals of as-synthesized Ge NWs.

XPS analysis has been also conducted for the acid treated NWs. XPS spectra for the Ge-3d and O-1s scans for the etched NWs using three different powder precursors are shown in Figures 2.23 (a)-(c), respectively. Figure 2.23 (a) shows Ge-(3d) signals

at a binding energy of 29.4 eV. The  $\text{GeO}_2$  signals at a binding energy of 32.8 eV disappeared following the acid treatment indicating successful removal of the oxide layer. Another evidence for the removal of the oxide layer is the rough O-(1s) signals as shown in the XPS spectrum provided in Figure 2.23 (b). Due to the removal of the oxide layer from the surface of the NWs, intensity of the oxygen signals get smaller and the spectra becomes rougher. However, the signals did not disappear completely indicating the presence of trace amount of oxygen on the NW surface. This could simply be adsorbed oxygen from the ambient in between acid etch and analysis. Extra shoulders have been obtained for the etched samples as shown in the XPS spectra given in Figure 2.23 (a) and (c). This shoulder comes from spin orbital splitting of Ge. The main signal consists of two separate signals at 29 and 30 eV, which corresponds to Ge-(3d) 5/2 and 3/2 spin orbitals, respectively. Highest intensity signal was obtained at the same binding energy value for all the precursors examined in this work, indicating the success of etching process for all three samples.

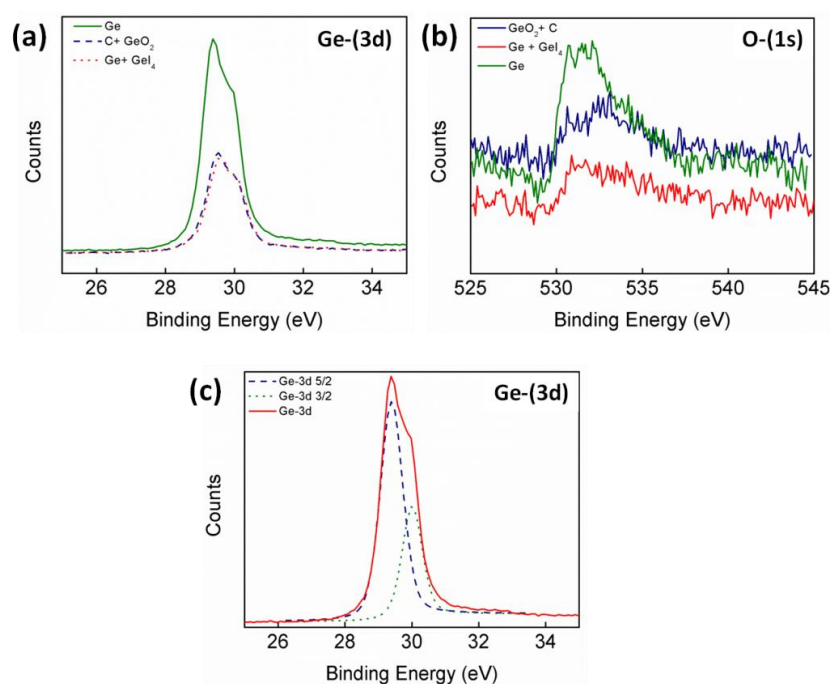


**Figure 2. 23.** XPS spectra for (a) Ge-(3d) and (b) O-(1s) signals of etched Ge NWs. (c) Ge-(3d) 5/2 and 3/2 signal separation of the main Ge-(3d) signal.

XPS analysis was also used to follow the reoxidation behavior of the NWs following etching process. For this purpose, as-synthesized, HBr etched and 2 days kept samples were analyzed. As-synthesized NWs exhibit only one signal at a binding energy of 32.8 eV, corresponding to GeO<sub>2</sub> oxidation state, as shown in Figure 2.24 (a). It has been observed that right after etching, oxide signal disappears and Ge-(3d) signal appears. After two days, NWs begin to get oxidized associated with appearance of a small oxide signal in the spectra. Oxide amount is the highest for the as-synthesized NWs. Etching completely removes the surface oxide; but after two days, oxide amount begins to increase, as shown in the XPS spectra given in Figure 2.24 (b).

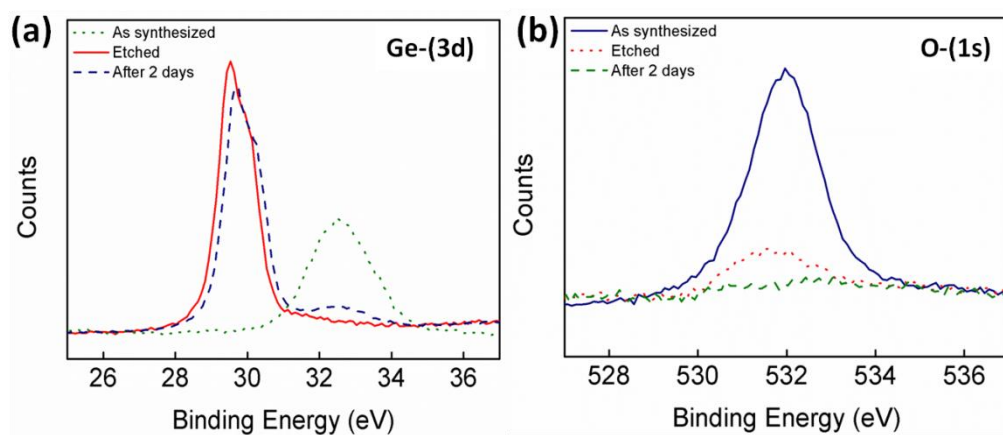


**Figure 2. 24.** XPS spectra for (a) Ge-(3d) and (b) O-(1s) signals of as-synthesized, HBr etched and 2 days kept Ge NWs (synthesized with Ge precursor under 950 °C and 100 mbar).

XPS analysis was also conducted in order to determine if iodine contamination has occurred for the NWs that are synthesized using Ge+ GeI<sub>4</sub> mixture precursor. XPS spectra for I-(3d) scan is provided in Figure 2.25. As can be seen from the Figure, spectra is very noisy and rough indicating that there is no iodine contamination on the NW surface.

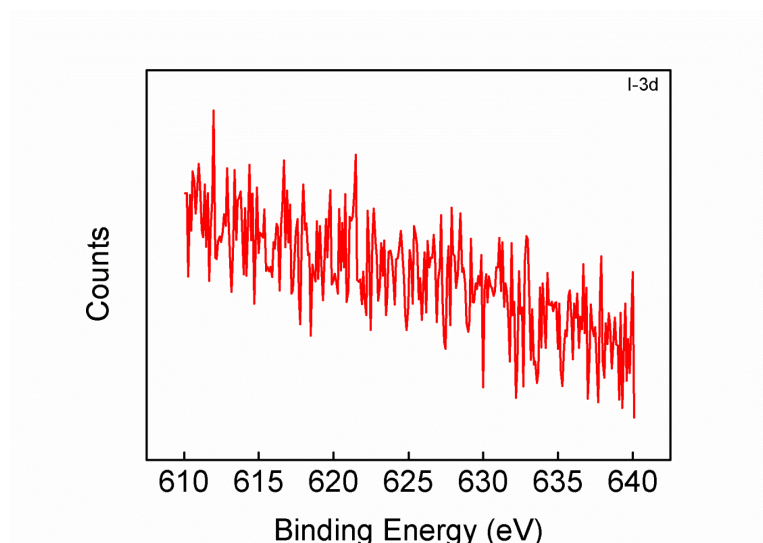


**Figure 2. 25.** XPS spectrum for I-(3d) scan of Ge NWs synthesized using  $\text{GeI}_4 + \text{Ge}$  mixture precursor.

#### 2.4.7 TEM Analysis

TEM analysis was carried out in order to determine the surface conditions, oxide thickness, oxide removal effectiveness and growth direction of the NWs. A representative TEM image of the as-synthesized Ge NWs has been provided in Figure 2.26 (a). It is evident that NWs got shortened during TEM sample preparation. As can be seen from the figure the diameters of the NWs are constant throughout the whole length of the NWs. Tapering was not observed as expected, since vapor transport method is known to provide taper-free and constant diameter NWs. Inset in the same figure provides evidence for the VLS growth mechanism, since higher contrast gold particle stays on the tip of the NW. Although all the NWs grew from a gold particle not all of them found to carry a gold cap within TEM analysis. This could simply be due to the sonication process by which fractionation of the NWs occurs or the gold particles fall off the tip.

A TEM image of a single Ge NW with its oxidized surface can be seen in Figure 2.26 (b). A homogenous and conformal, 10 nm thick oxide layer covering the NW

surface is apparent. Therefore, as-synthesized NWs cannot be used for device fabrication, in particular photodetectors without etching. The diameter of the NWs was measured to be 45 nm, consistent with the average measured values from SEM images.

A HRTEM image showing the single crystal defect free nature of the as-synthesized Ge NWs is provided in Figure 2.26 (c). Selected area diffraction pattern is provided in the inset. The growth direction of the NWs was found to be [111]. After supersaturation, during the nucleation process, Ge prefers [111] direction since it is the lowest energy plane between Au and Ge. Therefore, all of the NWs grow within that direction regardless of the precursor type.

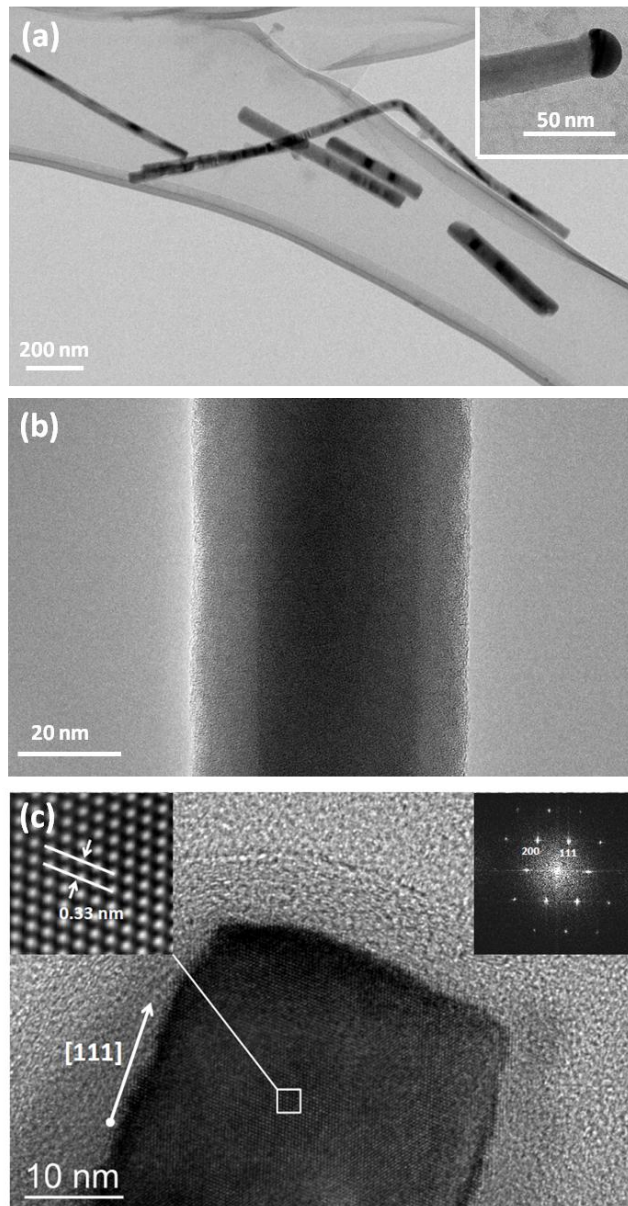


**Figure 2. 26.** (a) Low magnification TEM image of Ge NWs (synthesized with Ge precursor under 950 °C and 100 mbar). Inset shows a Ge NW with Au cap on it. (b) TEM image of a single Ge NW with oxidized surface (c) HRTEM image of a single Ge NW. Left inside shows inverse Fast Fourier transform (IFFT) image indicating the distance between (111) planes; right inset shows the Fast Fourier transform (FFT) pattern indicating the reciprocal space along [011] zone axis. [111] growth direction is indicated on the image.

Ge NWs can get either oxidized during the synthesis from the residual oxygen within the CVD or upon removal of the sample from the CVD system. Oxidation states before and after the HBr etching were explained in XPS characterization part. It is also confirmed with HRTEM images. HRTEM images of the as-synthesized and oxide etched Ge NWs synthesized with different precursors are shown in Figure 2.27 (a)-(e). As-synthesized NWs were stored at laboratory conditions for about 20 days prior to TEM analysis and etched NWs were examined immediately after HBr etching. Figure 2.27 (a) shows a Ge NW synthesized using Ge powder with a thick 10 nm oxide layer. After HBr etching, oxide layer was removed almost completely, as can be seen in Figure 2.27 (b). The same is valid for NWs synthesized using  $\text{GeO}_2 + \text{C}$  and  $\text{GeI}_4 + \text{Ge}$  powders, as shown in Figures 2.27 (c)-(f), respectively. However, there is an important difference. Oxide layer thicknesses are much lower for those NWs compared to the ones synthesized using Ge powder. This difference could come from the oxidation of NWs during the synthesis process.  $\text{GeO}_2 + \text{C}$  and  $\text{GeI}_4 + \text{Ge}$  powders seem to reduce the amount of residual oxygen within the chamber. Therefore, these NWs are only getting oxidized in laboratory conditions. Oxidation in ambient atmosphere (native oxide) is rate limited; therefore, the oxide layer thickness of the NWs that are not exposed to oxygen during synthesis process is thinner than the ones that are exposed to oxygen.

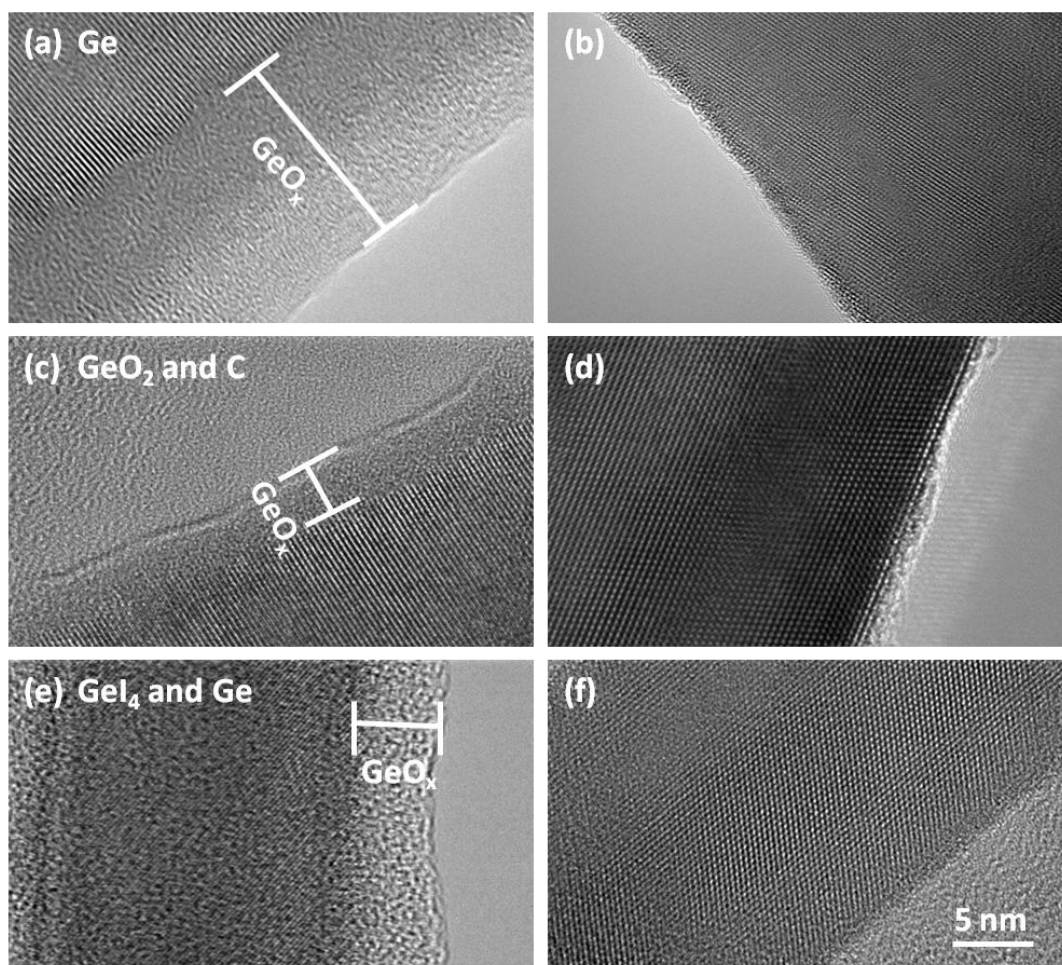


**Figure 2. 27.** TEM images of as-synthesized and HBr etched Ge NWs synthesized from (a,b) Ge powder, (c,d) GeO<sub>2</sub> and C powder mixture and (e,f) GeI<sub>4</sub> and Ge powder mixture.

## CHAPTER 3

### GERMANIUM NANOWIRE PHOTODETECTORS

#### 3.1 Introduction

##### 3.1.1 History of Photodetectors

In 1839 Edmunt Becquerel, a French physicist, first observed that when light is incident on a material, a weak current forms in it. Later, he called this phenomenon as the ‘photovoltaic effect’. Then in 1873, Willoughby Smit found that conductivity of selenium changes upon exposure to light [51]. After then, several experiments have been conducted on different materials in order to observe the photovoltaic effect. These improvements lead to construction of first semiconducting infrared (IR) photodetectors. Military applications are the most important driving force behind the research on IR detectors.

In the early forties, Ge was the most commonly used material in field effect devices and photoconducting detectors, as it was available with the best crystal quality and controllable doping [52, 53]. First point contact transistor was fabricated using a Ge slab in 1948 by researches from Bell Labs. Ge has been also used until early sixties in bipolar transistors. Meanwhile, better properties of Si combined with the advantage of Si wafers in planar technology applications have outshined Ge. Then, Si has been started to be widely used in solar cells and photodetectors [52]. However, wide band gap of Si (1.12 eV) has limited its applications in photodetectors only in the wavelength range below 1.1  $\mu\text{m}$ . Conversely, most photodetectors used in local

area networks, band to band and intra chip applications require detection of light in the range of 1.3-1.55  $\mu\text{m}$  [52]. Therefore, Ge with its narrow band gap (0.6 eV) offers higher absorption in the near- infrared range (NIR) of 1.3-1.55  $\mu\text{m}$ , standing out as a better candidate for optical fiber applications. Indium gallium arsenide (InGaAs) is a competitor material for Ge for NIR applications as it provides lower dark current compared to Ge however crystalline growth of InGaAs is a complex process.

First Ge on Si detector was fabricated by Luryi in 1984 [54]. Then, normal incidence (NI) Ge photodetectors were studied due to their ease in fabrication. In 2002, Fama et al. [55] developed a p-i-n NI Ge photodetector with highest responsivity (0.7 A/W) and in 2009 Klinger et al. [56] fabricated a p-i-n structure NI Ge photodetector with the highest bandwidth (49 GHz). In 2005 Liu et al. [57, 58] reported a zero bias p-i-n photodiode, which have wide spectral response. In 2008, first avalanche Ge photodetector was fabricated by Kang et al. [59]. Two years later, Assefa et al. [60] reported a metal-semiconductor-metal (MSM) avalanche Ge photodetector with 200 nm metal to metal spacing. In the same year, Ang et al.[61] fabricated the first waveguide avalanche Ge photodetector.

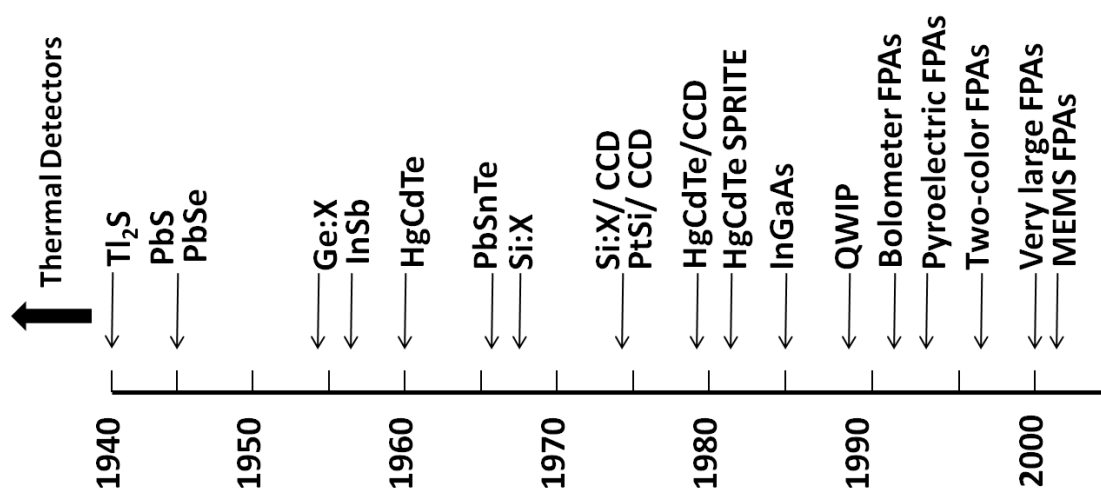


**Figure 3. 1.** History of various IR photodetector materials [53].

During history, many other materials have also been used for the fabrication of IR photodetectors [53]. As shown in Figure 3.1, before 1950s thermal detectors were used for IR detection. During 1950s, lead-salt detectors were in use for anti-air-missile seekers. Then, first extrinsic Ge detectors were introduced. 10 years later, metal silicate/silicon Schottky-barrier detectors were proposed enabling sophisticated read-out schemes. During these years, narrow bandgap compound semiconductor alloys were also under investigation. In 1950s, indium lead (InPb) was firstly used as a member of III-V family. Soon after, narrow band gap compounds, which belong to III-V ( $\text{InAs}_{1-x}\text{Sb}_x$ ), IV-VI ( $\text{Pb}_{1-x}\text{Sn}_x\text{Te}$ ) and II-VI ( $\text{Hg}_{1-x}\text{Cd}_x\text{Te}$ ) groups have been used. One advantage of these semiconductors was the control over their bandgap, which allows detection of the desired wavelengths. Mercury cadmium telluride (HgCdTe) is the most widely used variable bandgap IR detector; however, high vapor pressure of Hg introduces some difficulties during fabrication. Therefore, as an alternative in 1960s, lead tin telluride (PbSnTe) detectors were investigated. However, its high dielectric constant and large coefficient of thermal expansion mismatch with Si lead to abandonment of this material. At these times Si-Ge heterojunctions, aluminum gallium arsenide (AlGaAs) and gallium indium antimony (GaInSb) stand out as other alternatives to HgCdTe to be used in IR detectors.

### 3.1.2 Different Photodetector Models

A semiconductor photodetector working principle is to create an electron-hole pair upon illumination of light. If the energy of incident light is equal to or greater than the bandgap of the semiconductor, it excites valence electrons creating electron-hole pairs. Excited electrons move to conduction band, in where they can freely move long distances under an applied internal or external electric field, creating current. On the other hand, remaining holes contribute to the current by moving from one atomic site to another. The motion of these electron-hole pairs under light illumination is called photocurrent. The light generated current is then collected at the terminals of the photodetectors.

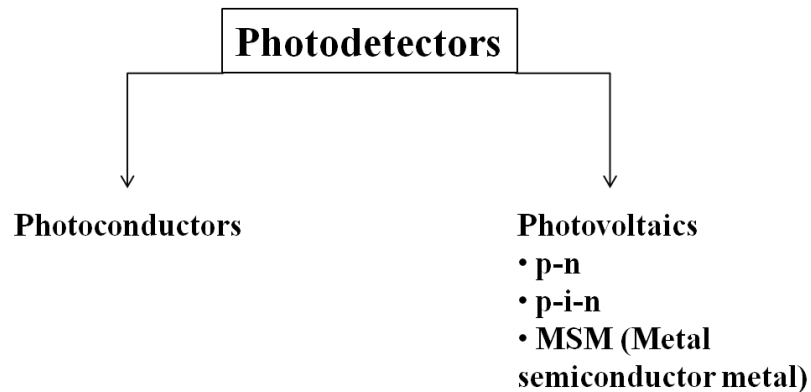


**Figure 3. 2.** Classification of photodetector devices [62].

The semiconductor photodetectors could be divided into two main groups according to their mechanism of electron-hole pair separation, as shown in Figure 3.2 [62]. First group is photoconductors in which, a single layer of a semiconducting material is combined with two ohmic electrodes. An external bias is applied between the electrodes to separate the electron-hole pairs and to collect the photocurrent. Second group is photovoltaics, which uses a p-n or Schottky junctions to create an internal electric field and hence separate electron-hole pairs. In this group, two or more layers of semiconductors are used in order to create p-n or Schottky junctions and in some cases an intrinsic layer is put between the p-n layers (p-i-n structure). Type of photodetectors will be briefly explained in this section.

### **3.1.2.1 p-n and p-i-n Photodetectors**

In a p-n structure, there is a p-type semiconductor physically linked to an n-type semiconductor. In the junction area due to the linkage of Fermi levels, a region with no free charges forms (space charge region (SCR)) as shown in Figure 3.3. Presence of charged donors and acceptors creates an electric field in that region. Therefore, photogenerated electron-hole pairs in SCR get separated by the help of an internal electric field before recombination. With the doping level of p and n layers, energy

barrier and electric field in the junction increases, which improves the efficiency of electron-hole pair separation, while width of the junction decreases. For moderate doping levels width of SCR is important. The photoresponse of a p-n photodetector increases if the photogenerated electron hole pairs are inside the SCR. Therefore in order to increase the spatial extend of this region an intrinsic (i) material is placed between the doped layers creating a p-i-n structure. Thereby high doping of p-n layers without decreasing spatial extend of SCR could be possible. In Ge p-i-n photodetectors, the intrinsic layer is usually Ge while p and n layers are formed in-situ or through implantation doping of Ge layers. Si single crystal p-n layers can also be used [54].

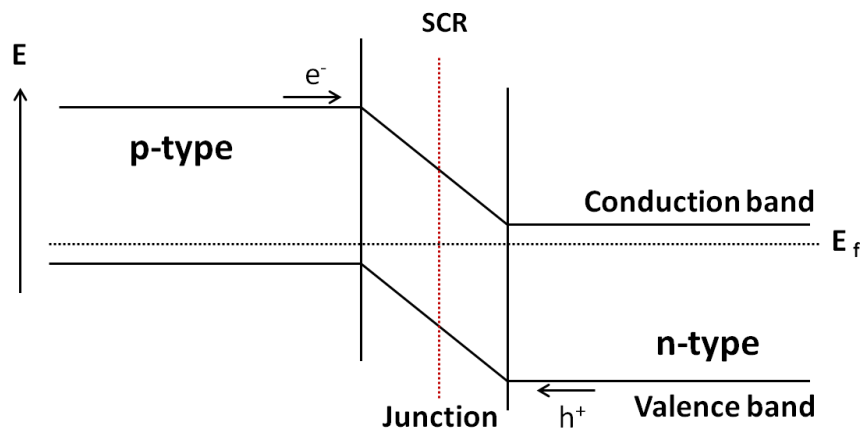


**Figure 3. 3.** Energy band diagram of p-n photodetectors.

### 3.1.2.2 Avalanche Photodetectors

An avalanche photodetector has a p-i-n structure. Once the reverse bias voltage is high enough, it closes the breakdown voltage of the photodetector. When such a bias is applied on the photodetector, photogenerated charge carriers in SCR get accelerated enough to separate secondary charge carriers from other atoms. This is so called the avalanche effect. Therefore, in avalanche photodetectors, incoming photon

creates more than one electron-hole pair leading to a gain value higher than one. In these photodetectors, p-n layers are highly doped in order to obtain a high internal electric field.

### 3.1.2.3 Metal-Semiconductor-Metal Photodetectors

Metal-semiconductor-metal (MSM) photodetectors are composed of two Schottky junctions. A single layer of semiconductor is placed between two metal electrodes and a voltage is applied to the electrodes. Therefore, one electrode will be under reverse bias while the other will be under forward bias, as illustrated in Figure 3.4. In the figure  $L$  is the distance between the electrodes,  $I_{ph}$  is the photogenerated current and  $\Phi$  is the height of the Schottky barrier. The reverse biased metal-semiconductor end produces a Schottky barrier and created internal electric field separates photogenerated electron-hole pairs. On the other hand, forward biased metal-semiconductor end acts as a collector electrode. In MSM photodetectors, semiconductor material is in its intrinsic form, highly pure and resistive.

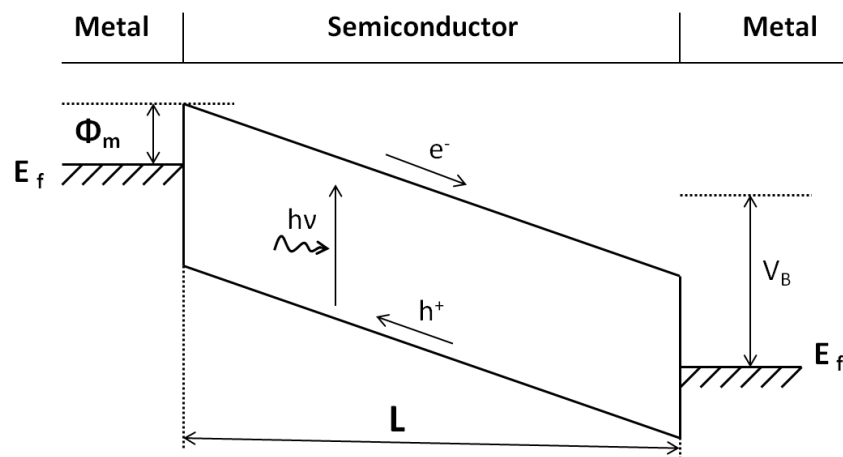


**Figure 3. 4.** Energy band diagram of a MSM photodetector under bias.

### 3.1.2.4 Nanowire Photodetectors

Photoconductivity of NWs has been widely studied. Because of their high surface to volume ratio, NWs have enhanced biological and chemical sensitivity. They are also used in many applications such as photovoltaics, optical switches, optical interconnects, transceivers, sensors and photodetectors [63].

Many different NWs have been used as the active material in photodetectors. Group III-V compound NWs have excellent transport properties, they can be easily doped, respond to a wide spectral range by bandgap engineering and have very fast responses since the charge carrier relaxation times are around picoseconds. Indium phosphide (InP), gallium arsenide (GaAs), aluminum gallium arsenide (AlGaAs), indium gallium arsenide (InGaAs) and gallium nitride (GaN) NWs are some group III-V examples used in photodetectors. Similarly group VI NWs are also widely investigated. Among them, selenium (Se) and tellurium (Te) are the most studied materials. Group II-VI NWs provide a direct bandgap and cover a wide spectrum of light. Cadmium telluride (CdTe), zinc telluride (ZnTe), cadmium selenide (CdSe), zinc selenide (ZnSe) and cadmium sulfide (CdS) NWs were investigated from this group. Metal-oxide NWs are also good photoconductors due to their wide band gap, they are used in UV photodetection. Zinc oxide (ZnO), cadmium oxide (CdO) and vanadium (V) oxide ( $V_2O_5$ ) are some examples within this group.

Ge and Si are group IV elemental semiconductors. Si NWs have been extensively used for visible light detection. Si NW photodetectors reveal high photoconductive gain and are easy to fabricate. Ge NWs, on the other hand, are used in most of the previous studies, as individual form with conventional metal thin film electrodes [64, 22, 65, 52]. In these studies, single NW photodetectors show slow response with high noise. In addition, although utilized, metal thin films for contacts are not desired for fully flexible devices. Moreover, devices utilizing single NWs require intense lithographical processes for their fabrication limiting their commercial applications. Instead of individual NWs, using NW networks as the active material enhances

photodetection, decreasing response time and increasing sensitivity [66, 67, 68, 69, 70]. Network concept in devices allows the fabrication of devices through economic and wide-scale available methods such as transfer printing, stamping or spray coating [71]. This could also shift the research focus to large area electronics that are flexible and transparent. However, fabricating a uniform NW network on large areas is still missing for Ge. Drop casting method is not suitable over large areas, giving a non-uniform network that would lead to irreproducible devices [29].

Transparent and flexible devices require transparency and flexibility for both their active semiconducting and passive metallic elements. Transparency using thin film or bulk elemental semiconducting materials (such as Ge and Si) is not possible for optoelectronic devices. Semiconducting NW networks at this stage provide unique advantages. Transparent contacts, on the other hand, necessitate the use of very thin metallic films, inorganic oxides or NW / nanotube networks. Indium tin oxide (ITO) is the most widely used inorganic oxide for transparent and conducting electrodes. However, several inherent problems associated with it, limit its wide scale utilization. A few of these problems include limited availability of indium in contrast to large scale need for it for flat panels, vacuum deposition requirement due to inferior properties of its solution deposited counterparts and limited chemical stability and flexibility. Networks of one-dimensional conducting nanostructures such as single walled carbon nanotubes (SWNTs) [72,73] and NWs [74] with graphene [75] offer unique advantages if only performance metric of ITO has been met. They can be solution deposited over large areas. For instance, SWNT and silver (Ag) NW networks are successfully used as electrode materials in many studies such as flexible organic thin film transistors [76], solar cells [77], resistive touch screens [78,79], photodetectors [80,81] and organic light emitting diodes [75].

An important point in the fabrication of flexible devices, on the other hand, is to make both the active semiconducting element and the contacts flexible. Although many groups report on flexible active semiconductors, they still use non-flexible and crystalline and evaporated metallic thin films for contacts [82-87].

All NW Ge photodetectors, which consist of NWs both in the active channel and electrode was fabricated in this study. Network enhanced, transparent, flexible, high efficiency, fast response and recovery time Ge photodetectors were fabricated using SWNT and Ag NWs as solution deposited and transparent electrodes. For this, transparent Ge NW networks were fabricated uniformly through vacuum filtration and stamping method over similarly prepared Ag and SWNT network electrodes. This method precisely allowed the control over the NW network densities enabling the fabrication of photodetectors with desired transmittance and dark current. Ge NW network properties with the photoresponse characteristics of the photodetector devices are investigated.

### **3.2 Experimental Details**

For the fabrication of photodetectors, Ge NWs were synthesized by vapor transport method as explained in Chapter 2. To sum up, 10 mg Ge powder was placed in a small quartz tube and the tube was placed in the middle of a horizontal tube furnace. 2 nm Au coated Si substrates were placed at the cold end of the furnace. Whole system was taken under vacuum in order to decrease the oxygen content and then the pressure was maintained at 100 mbar. The temperature of the furnace during the reaction was kept at 950 °C, while the temperature of the substrate was around 750 °C. At this temperature, Ge powder got vaporized and carried towards the Si substrate with the help of carrying argon gas. Then, it formed a eutectic alloy with Au and grows by VLS mechanism<sup>[35, 36]</sup>. The duration of the reaction determined the length of the NWs. At the end of a one-hour reaction, dark brown layer on the Si substrate indicates the existence of Ge NWs as shown in Figure 3.5 (a)-(b). The length and the diameter of the NWs were found to be around 15 μm and 60 nm, respectively.

Following growth, the surface of the as-synthesized Ge NWs was found to be highly oxidized. The thickness of the oxide layer was around 10 nm. In order to remove this insulating layer, hydrobromic acid (HBr) etching (20 wt %) was conducted for a few minutes.

After etching process, the growth substrate was sonicated for a few seconds in isopropanol to obtain a suspension of Ge NWs. A photo of Ge NW suspension is shown in Figure 3.5 (c). In this step, NWs were cracked from the substrate and dispersed in isopropanol. Excessive sonication was avoided to prevent further rupture of NWs. The Ge NW suspension was then vacuum filtrated on to mixed cellulose ester (MCE) membranes. The vacuum filtration setup is shown in Figure 3.5 (d). The Ge NW suspension was poured through the glass tube. Then the pump was turned on and Ge NWs were trapped on the filter paper, while isopropanol is filtered through it. Following the filtration process, Ge NWs in the form of a network was obtained on the filtration membrane, as can be seen in Figure 3.5 (e). Finally, the filter paper was stamped onto soda-lime silicate glass or polyethylene terephthalate (PET) substrates and dissolved through consecutive acetone washings, allowing the transfer of Ge NW network onto the substrate surface. A photo of a glass substrate with Ge NWs on it is shown in Figure 3.5 (f). NW networks have adequate transparency so that the METU logo behind the glass slide is clearly visible.

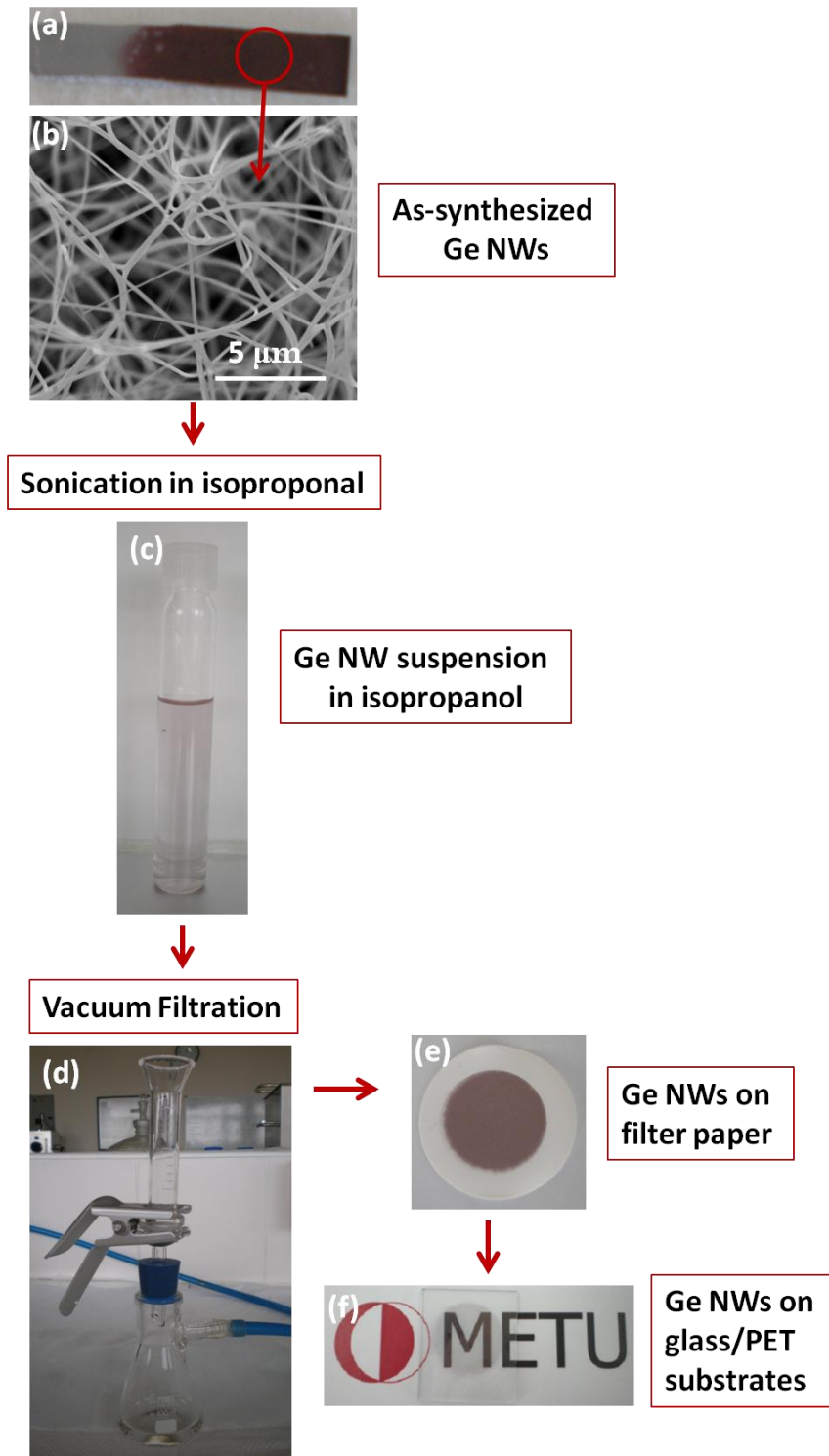


**Figure 3. 5.** Flow chart of Ge NW transfer onto the glass or PET substrates.

Ag NWs were synthesized using a polyol process. In this process, a 10 mL of 0.45 M ethylene glycol (EG) solution of polyvinylpyrrolidone (PVP) was prepared and 7 mg of sodium chloride (NaCl) was added into the solution. Meanwhile, a 0.12 M AgNO<sub>3</sub> solution in 5 mL of EG was also prepared. Then, the PVP solution was heated to 170 °C and AgNO<sub>3</sub> solution was added drop wise into the PVP solution by an injection pump at a rate of 5 mL/h. The solution was stirred during the whole process at a rate of 1000 rpm by a magnetic stirrer. Once the Ag<sup>+</sup> ions are introduced in the solution Ag NW formation starts [88]. Following the synthesis, NWs were centrifuged two times in acetone and one time in ethanol at 10000 rpm, in order to purify the NWs. Right after purification, NWs were dispersed in isopropanol and spray coated onto glass or PET substrates. The substrate to be coated was heated to 150 °C on a hot plate. The transparency and sheet resistance of Ag NW networks used in this study was 85% and 15 Ω/sq, respectively [89].

SWNTs on the other hand were coated onto substrates by vacuum filtration method, as described previously. In brief, 2 mg/L SWNTs (Carbon Solutions “P3”) were dispersed in deionized water with the help of sodium dodecyl sulfate (SDS) through tip sonication. After that, the suspension was vacuum filtered on MCE membranes and transferred to glass and PET substrates. For the transfer, samples were compressively loaded and dried at 80 °C. Finally, membranes were etched within consecutive acetone and isopropanol alcohol baths. All samples were nitric acid (65%) treated for 3 hours to improve their conductivities [90]. Sheet resistance and transparency of the prepared SWNT thin films were 100 Ω/sq and 85%, respectively.

A schematic for the fabrication of the photodetectors is shown in Figure 3.6 (a)-(e). SWNT or Ag NW networks were deposited onto substrates as schematically shown in Figure 3.6 (a). This was followed by formation of a 20 μm gap simply by mechanical scratching with a scalpel as illustrated in Figure 3.6 (b). After that, Ge NW networks were deposited in between the SWNT or Ag NW network electrodes, as shown in Figure 3.6 (c). Contact pads were then formed by silver paint on the Ag NWs and SWNTs as shown in Figure 3.6 (d) and finally the photodetector was characterized through illumination by an A.M. 1.5 solar simulator from top as shown

in Figure 3.6 (e). An SEM image of the channel region of Ag-Ge photodetector before and after Ge NW deposition is shown in Figure 3.6 (f) and (g), respectively. The gap was free from Ag NWs confirmed by electrical measurements, as shown in Figure 3.6 (f) prior to Ge NW network deposition. In Figure 3.6 (g), thicker NWs were Ag, while the thinner ones were Ge. Likewise, Figure 3.6 (h) shows an SEM image of SWNT-Ge photodetector. SWNTs formed a network below the Ge NWs and again the gap was confirmed to be free from SWNTs prior to Ge NW network deposition. A photograph of fabricated Ge NW photodetector is shown in Figure 3.7. In a single 2.5x2.5 cm glass substrate, like the one shown in Figure 3.7, there are 9 photodetector devices.

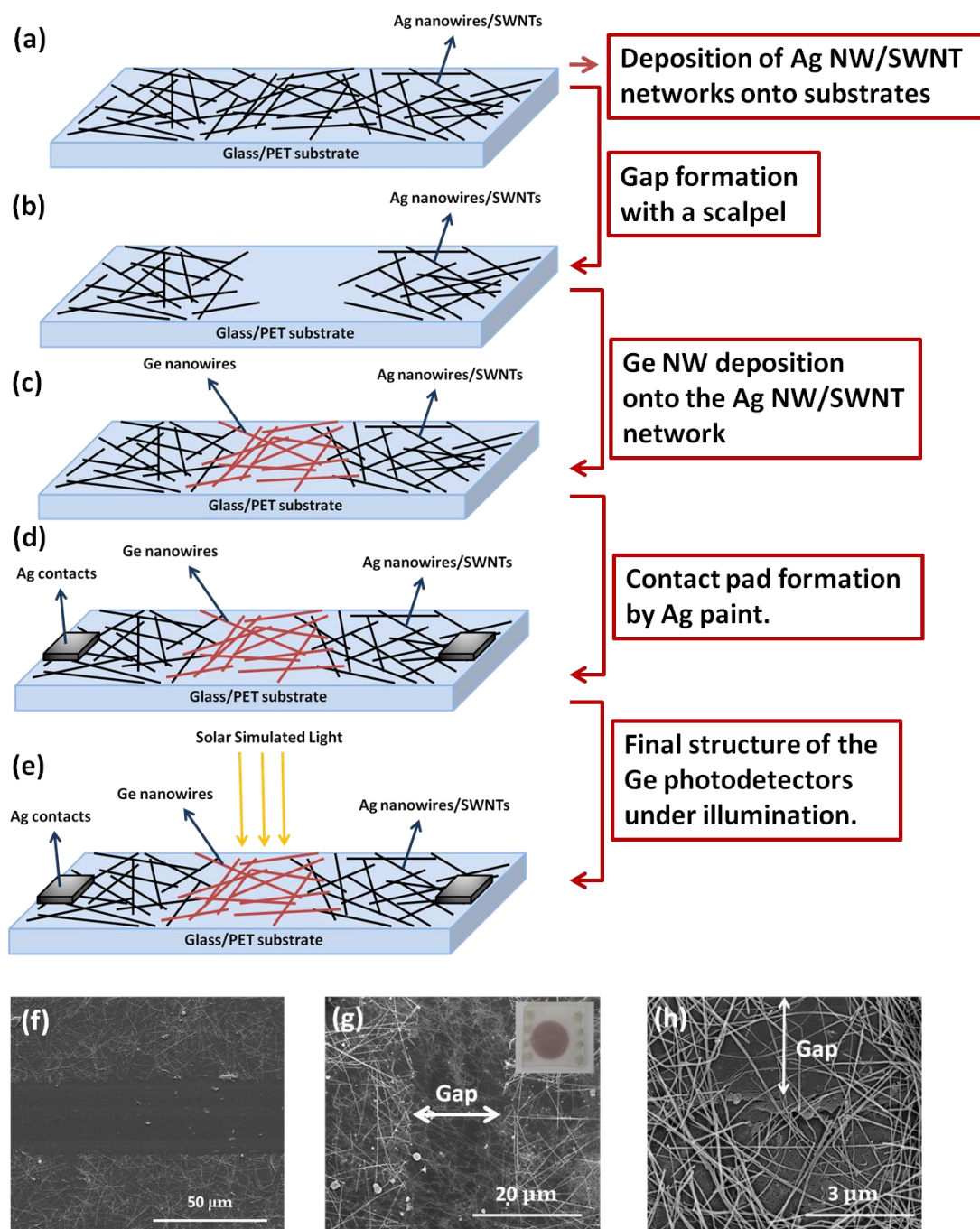


**Figure 3. 6.** (a-e) Flow chart of the fabrication procedure of Ge NW photodetectors. (f) SEM image of Ag NW network with a gap of 20 μm formed by mechanical scratching. SEM images of a (g) Ag-Ge and (h) SWNT-Ge photodetectors following Ge NW deposition.

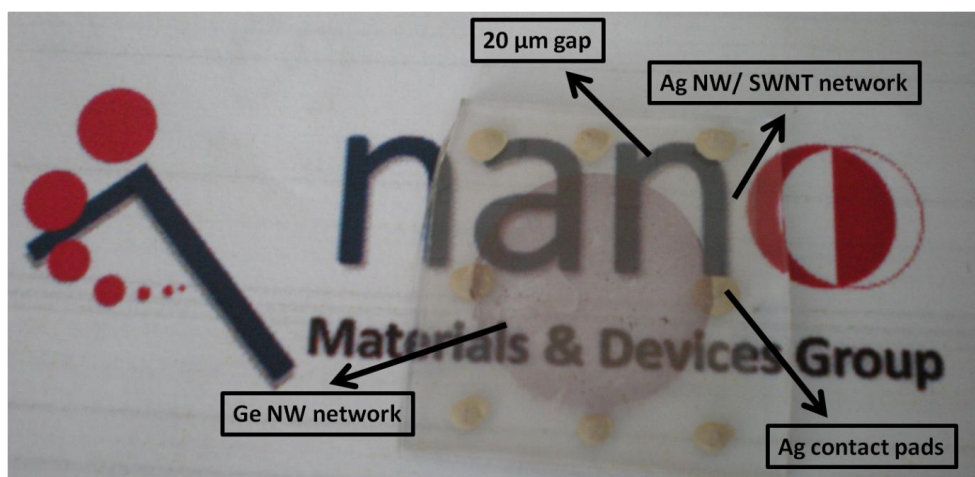


**Figure 3. 7.** Photograph of a fabricated Ge NW network photodetector.

### **3.3 Device Characterization Methods**

#### **3.3.1 Scanning Electron Microscopy**

Photodetectors were examined with FE-SEM (Nova NanoSEM 430). The operation voltage was 10 kV for all the samples. A 5 nm gold coating was applied through sputtering before microscopy as both glass and PET substrates were insulating. Gaps formed by scratching were confirmed to be free from Ag NWs or SWNTs by SEM investigation.

#### **3.3.2 Current-Voltage and Photoresponse Measurements**

Current- voltage (I-V) measurements were conducted in two modes. First mode was dark I-V measurements. A bias between  $\pm 5$  V was applied through a Keitley 2400 sourcemeter to the photodetector by connecting the Ag pads with two probes and corresponding current values were measured under dark. Dark measurements also illustrates the resistance of Ge NW networks. Then, the same measurement was conducted under a ORIEL 92192 Full Spectrum Solar Simulator, which had a 500 W, 10x10 cm collimated output with a calibrated light spectrum of AM 1.5G.

Photoresponse measurements were done under the same solar simulator by switching the shutter in front of the light supplier while a 5 V bias was applied to the photodetector. The reset time measurements were done with an Agilent B 1500 A parameter analyzer under 5 V bias.

### 3.3.3 Optical Transmittance Measurements

Transmittance measurements were made both for Ag, SWNT and Ge thin films separately and for the photodetector devices. Carry 5000 UV-Vis-NIR spectrometer was used for the transmittance measurements. The measurements were made between 300-800 nm wavelengths.

## 3.4 Results

### 3.4.1 Transparency and Resistance Variation with Ge NW Network Density

Density of the NWs could be controlled during filtration step by filtering the desired amount of NW solution, which can also control the conductivity and transmittance of the NW network. The as-synthesized and etched NWs were sonicated in 20 ml isopropanol solution. Then 2, 4, 6 and 8 ml of the same solution was filtered and stamped to obtain networks with different densities. Photographs of half of the filter papers which contain different densities of Ge NW networks are shown in Figure 3.8.

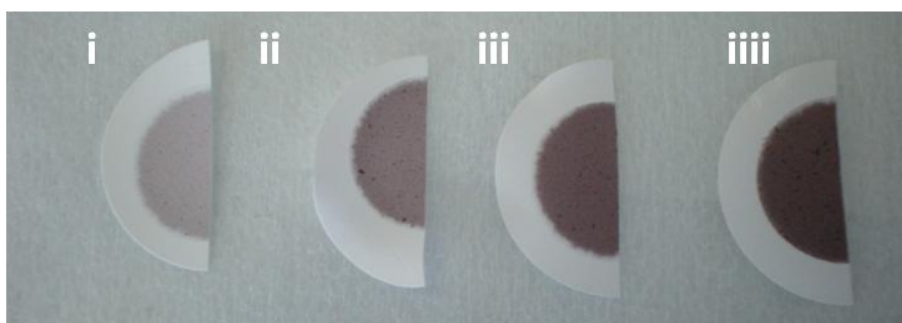


**Figure 3. 8.** Half of the filter papers with different Ge NW network densities of i) 1.4, ii) 1.8, iii) 2.0, iiiii) 2.5 NWs/ $\mu\text{m}^2$ .

SEM images of the Ge NW networks deposited from filtered solutions of 2, 4, 6 and 8 ml are shown in Figure 3.9 (a)-(d), respectively. A software program, Image J, was used for the network density calculations from the obtained SEM images. Corresponding NW densities were then calculated as 1.4, 1.8, 2.0, 2.5 NWs/ $\mu\text{m}^2$ , respectively.

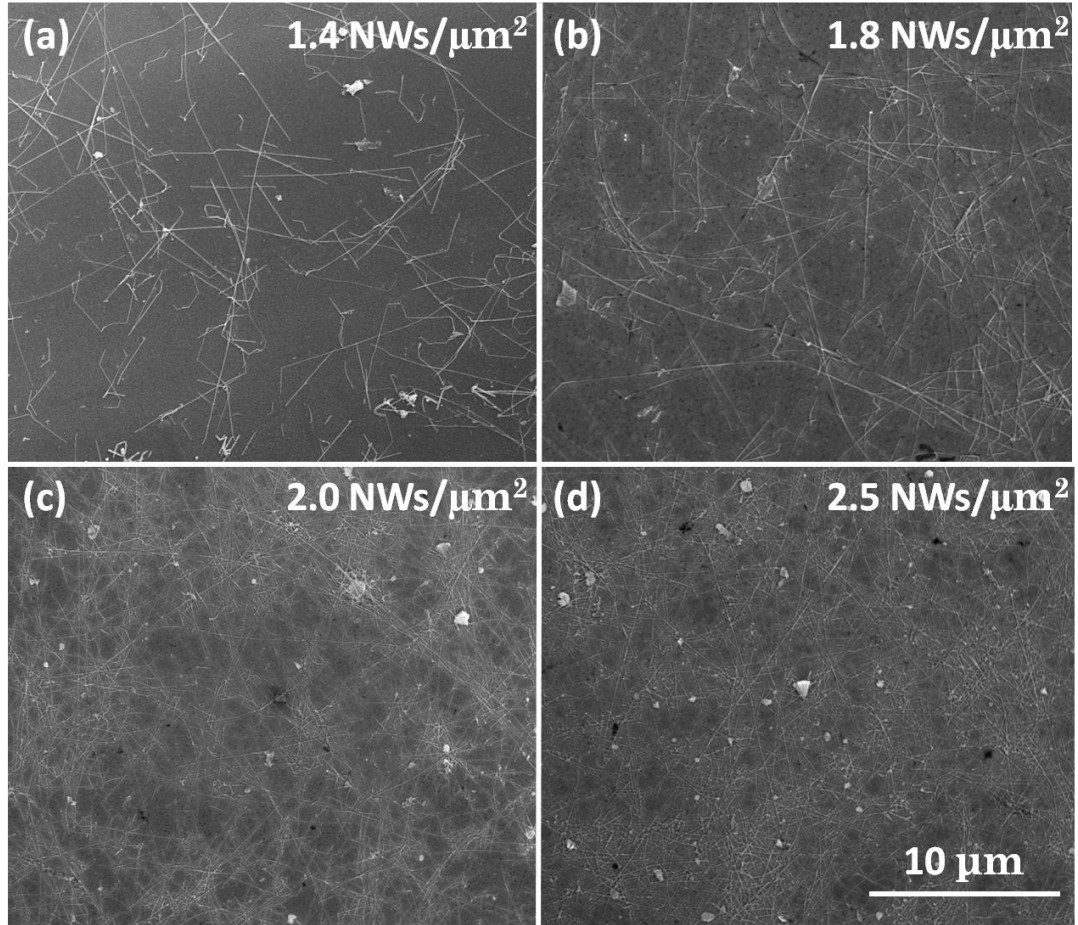


**Figure 3. 9.** SEM images of Ge NW networks deposited onto glass substrates with densities (a) 1.4, (b) 1.8, (c) 2.0 and (d) 2.5 NWs/ $\mu\text{m}^2$ .

Figure 3.10 (a) and (b), reveals the transmittance of Ge NW networks and fabricated photodetectors with different Ge NW densities within the wavelength range of 300 to 800 nm. Transmittance was 75% (at 550 nm) for the Ge NW network with a density

of 1.4 NWs/ $\mu\text{m}^2$  and it decreases down to 40 % for a network with a density of 2.5 NWs/ $\mu\text{m}^2$ , as shown in Figure 3.10 (a). Ag NW and SWNT network electrodes have a very high and uniform transmittance within the investigated range, hence they have only slightly decreased the total transmittance of the fabricated devices, as can be seen in Figure 3.10 (b). A plot showing the variation of the dark resistance of the Ge NW networks with transmittance is provided in Figure 3.10 (c). As expected, transmittance decreases as dark resistance decreases, due to creation of alternate current paths.

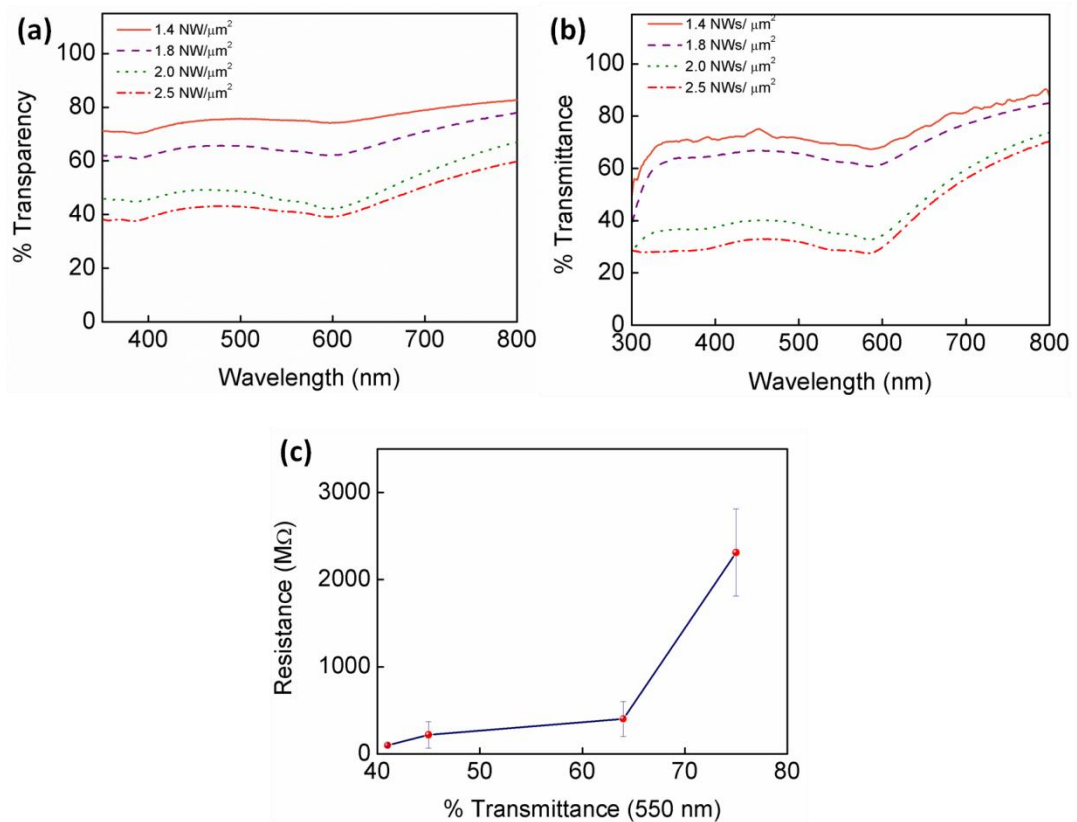


**Figure 3. 10.** Transmittance of (a) Ge NW networks with different densities and (b) fabricated photodetectors. (c) Dark resistance variation of the Ge NW networks with transmittance measured at 550 nm.

### 3.4.2 Ge NW Network Photodetector Characterization Results

Current-Voltage (I-V) and ON/OFF characteristics of Ag-Ge and SWNT-Ge NW network photodetectors with various densities on glass and PET substrates were examined.

A typical I-V characteristic of Ag-Ge photodetectors on glass substrate is shown in Figure 3.11. The response was symmetric and quasi-linear, which indicates highly resistant NW-NW junctions instead of ohmic NW-electrode junction dominated conduction.

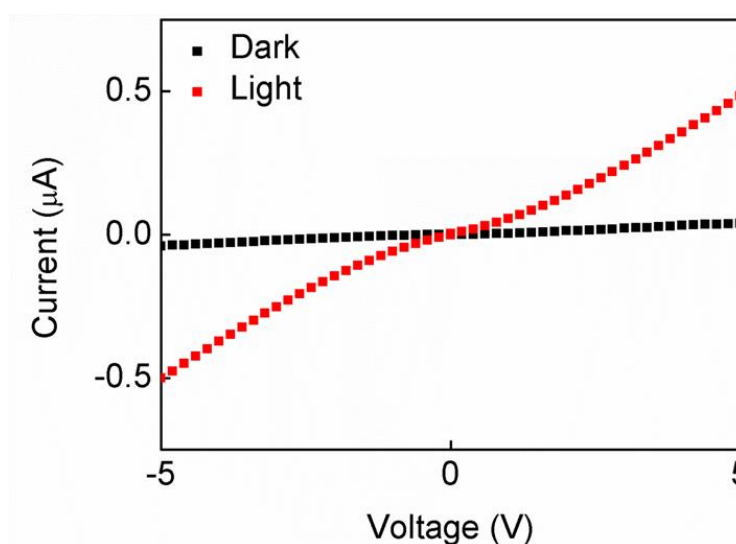


**Figure 3. 11.** A typical I-V curve for Ag-Ge NW network photodetectors under dark and light.

Light ON/OFF response of the same samples is shown in Figure 3.12. Dark and light current changed with Ge NW density in the network. As can be seen from Figure 3.12, both dark and light currents increased as NW density changed from 1.4 to 2.5 NWs/ $\mu\text{m}^2$ . In addition, as Ge NWs get denser, charge generation capacity under illumination was increased. Therefore, photoresponse current, which is defined as  $(\Delta I = I - I_0)$ , increased from 0.033  $\mu\text{A}$  to 0.42  $\mu\text{A}$ , as the NW density increased from

1.4 to 2.5 NWs/ $\mu\text{m}^2$ . The ratio between light and dark current was 5 and it stayed constant as both dark and light current changes simultaneously with the NW density. Fully reversible switching behavior was observed for all devices with Ag and SWNT network electrodes during ON/OFF measurements, which illustrates the reproducibility of the devices.

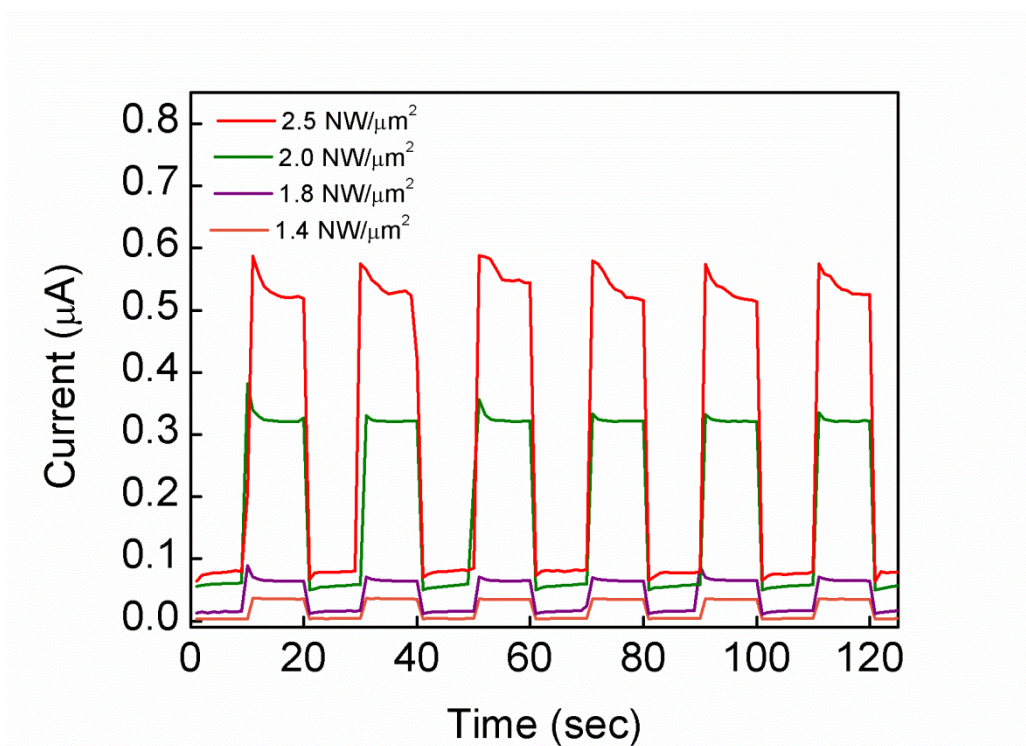


**Figure 3. 12.** Light ON/OFF responses of Ag-Ge NW network photodetectors on glass substrates with different Ge NW densities.

In previous studies, photoresponse time of Ge NW devices was indicated to be lower than 0.2 seconds [29]. In this study, the response time of the fabricated photodetectors were found to be lower than 10 ms, as can be seen in Figure 3.13 (a), which is much faster than individual Ge NW devices and several other network devices [91]. Yan et al. [29] first studied Ge NW network photodetectors and they attributed this effect to the barrier dominated conductance. For individual Ge NW photodetectors, the electron conduction mechanism occurs by desorption and

adsorption of oxygen atoms through the surface of the NWs. Upon exposure to air, oxygen atoms get adsorbed on the surface of NWs by capturing electrons. Upon illumination, charge carriers are generated and holes are accelerated through the NW surface to fill the charge traps or leading to desorption of the oxygen atoms, as shown in Figure 3.13 (b). For this mechanism to occur, oxygen and hole diffusion, both of which are very slow, should take place. Hence, response time of a single NW device is above 70 seconds. For Ge NW network devices, on the other hand, conduction mechanism occurs in a different way. Barrier dominated conduction is responsible for the fast response and recovery time. Barrier dominated behavior was explained in a study on ZnO NWs carried out by Zhou et al.[92] In that study, photoresponse behavior of a single ZnO NW with ohmic and Schottky contacts was examined separately. ZnO NW showed very slow response, when it was connected with ohmic contacts; while its response was greatly enhanced with Schottky contacts. The conduction mechanism of ZnO NWs is the same with the one in Ge NWs; in other words, both of them are dominated with the oxygen adsorption and desorption mechanism. However, when there is a Schottky contact the oxygen adsorption/desorption around the Schottky contact is enough to increase or decrease the current. Upon illumination, the desorbed oxygen atoms increase the carrier density and decrease the height of the Schottky contact, hence current increases. When the light is turned off, adsorbed oxygen atoms around schottky barrier decrease the number of charge carriers and increase the height of the Schottky barrier, as shown in Figure 3.13 (c). Hence, current decreases in a shorter time than the ohmic contact ZnO photodetectors. For Ge NW networks, there are two barriers for electron conduction, which are NW-NW junction barrier and NW-electrode (Ag NW or SWNTs) junction barrier. For Ge NWs, NW-NW junction barrier acts as two Schottky barriers placed back to back. When light is incident on the device, carrier density increases, NW-NW junction barrier height decrease and electron conduction occurs through the NW junctions. This mechanism is much faster than oxygen adsorption and desorption thus, NW network devices exhibit much faster response and relaxation times than their individual NW counterparts.

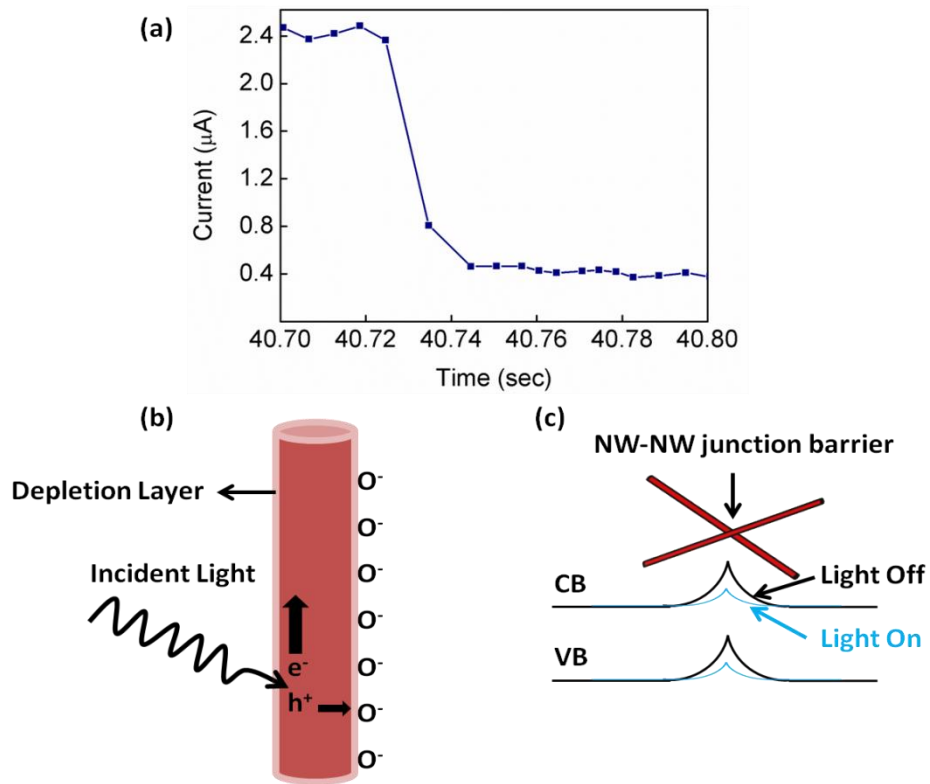


**Figure 3. 13.** (a) Enlarged view of the reset time of a Ge NW photodetector. The reset time is found to be less than 10 milliseconds. (b) Schematic of charge generation within the Ge NWs. (c) NW-NW junction barrier height variation with incident light.

In Figure 3.12, it is also shown that there is no cavity for both response and relaxation time of the photodetectors, which means that the current increases to its maximum value in less than 10 milliseconds right after the light is turned on. A small signal appears in the first few seconds upon illumination and current gradually decreases to a stable value. In a similar study, same characteristic signal was observed for a field effect phototransistor fabricated with Si NW networks as the active material [93, 94]. It was concluded that the reaction of NW surfaces with air molecules or water vapor was responsible for this; since no such behavior was observed when light ON/OFF measurements were conducted under vacuum.

Response characteristics of SWNT-Ge and Ag-Ge photodetectors on glass substrates are compared in Figure 3.14. SWNT-Ge photodetector was found to have lower dark

current when compared to Ag-Ge photodetector even if it had higher light current. This was due to the higher sheet resistance values of SWNT networks used in this study compared to Ag NW networks under the same transmittance.

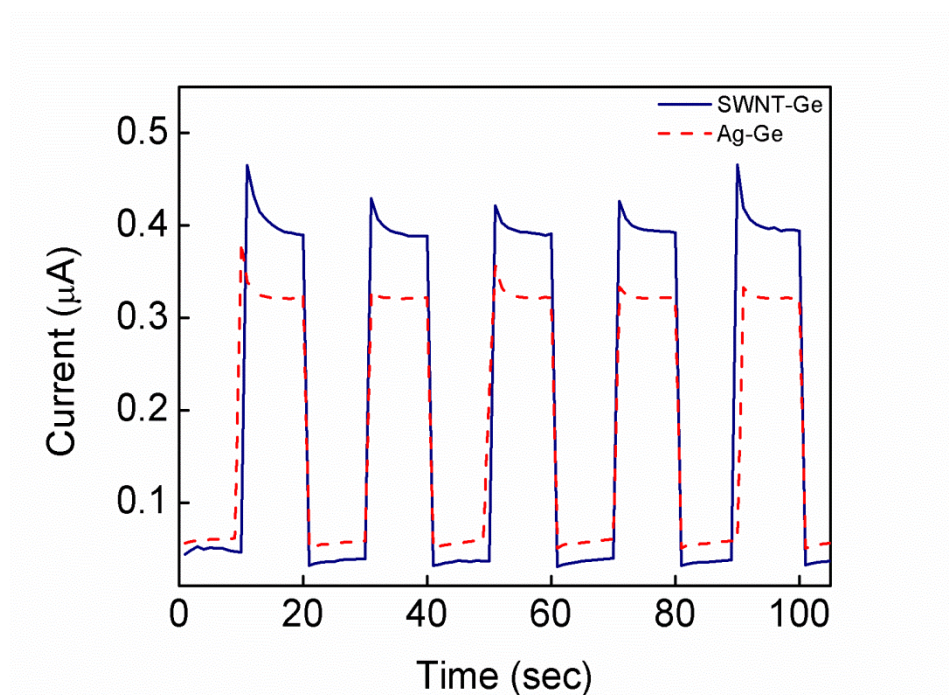


**Figure 3. 14.** Comparison of light ON/OFF responses of Ag-Ge and SWNT-Ge NW photodetectors on glass substrates.

I-V and light ON/OFF measurements were also conducted for flexible devices fabricated on PET substrates under flat and curved conditions. Typical I-V characteristics and light ON/OFF curves of SWNT-Ge photodetectors flexed to different radius of curvatures are provided in Figures 3.15 and 3.16 (a), respectively. The photoresponse current was measured upon bending. A 10 % increase in both dark and light current was found upon bending. This increase was attributed to better mechanical coupling between electrodes and Ge NWs as the device was bent. The dark and light currents were also measured after several bending cycles as shown in Figure 3.16 (b). Repeated bending cycles resulted only in a small decrease in the light current, whereas the dark current showed almost no change. The same behavior

was also observed for Ag-Ge photodetectors. The ON/OFF measurements of Ag-Ge and SWNT-Ge photodetectors are compared in Figure 3.17. Dark current of SWNT-Ge photodetectors was found to be lower than Ag-Ge photodetector, while both of them have the same light current, as described previously.

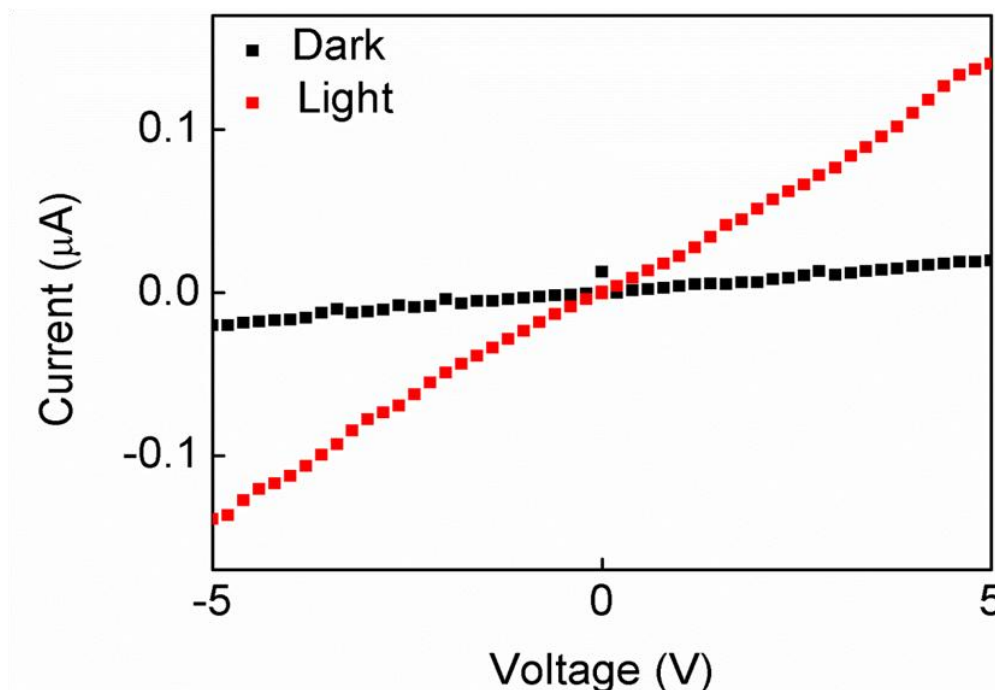


**Figure 3. 15.** A typical I-V curve for SWNT-Ge photodetectors on PET substrates.

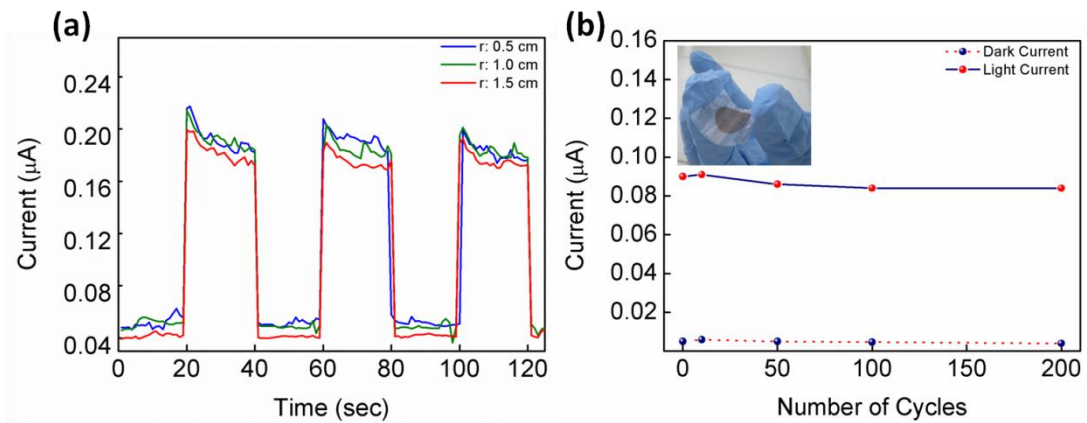


**Figure 3. 16.** Light ON/OFF measurements of SWNT-Ge photodetectors on PET substrates with (a) different bending radius and (b) repeated bending cycles. Inset shows a flexible SWNT-Ge photodetector.

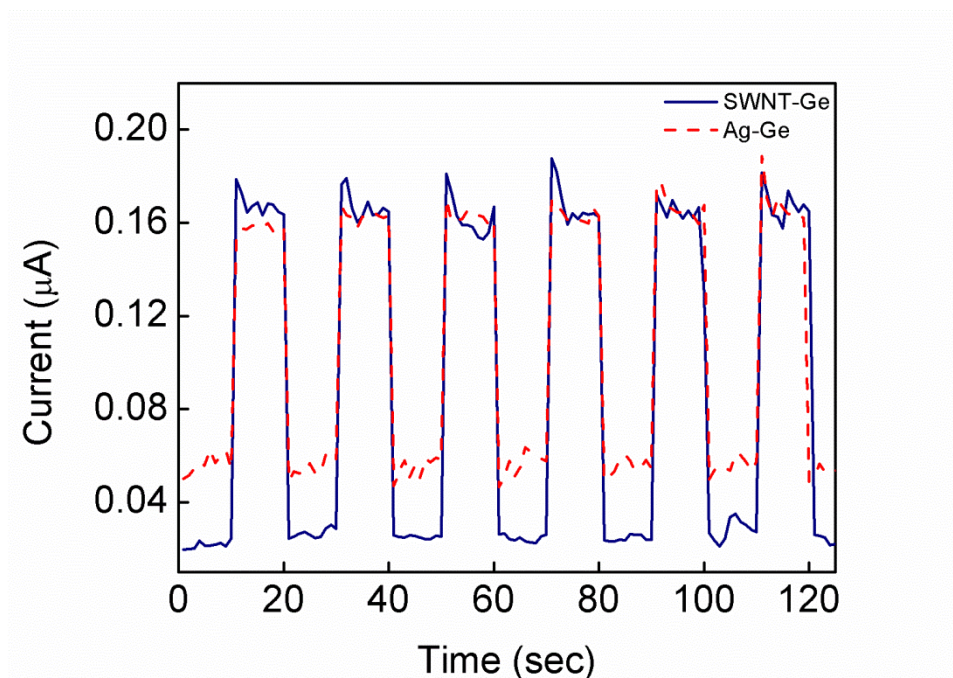


**Figure 3. 17.** Comparison of light ON/OFF responses of flat Ag-Ge and SWNT-Ge NW photodetectors on PET substrates.

## CHAPTER 4

### CONCLUSIONS AND FUTURE RECOMMENDATIONS

#### 4.1 Conclusions

In this study, Ge NWs were synthesized by vapor transport mechanism using three different solid powder precursors, which were Ge, GeI<sub>4</sub>+Ge and GeO<sub>2</sub>+C powders. Following synthesis, NWs were used to fabricate fully transparent and flexible Ge NW network photodetectors. Fabricated photodetectors were then characterized.

In the first part, synthesis of Ge NWs with three different precursors was investigated. Parametric studies with respect to temperature and pressure were conducted. The average diameter and length of the NWs were 40 nm and several microns, respectively, and diameters were found to increase with temperature and pressure. Following synthesis, the oxide layer around the as-synthesized NWs was removed. The oxide layer was found to be thicker on Ge NWs synthesized from Ge powder compared to other precursors. Oxide layer was removed by HBr etching and confirmed with TEM and XPS analysis.

In the second part of the thesis, photodetectors were fabricated from the synthesized Ge NWs. For this purpose, Ge NW networks were deposited onto glass and PET substrates by vacuum filtration and stamping method. Vacuum filtration method enabled control over the NW density and in turn conductivity and transmittance of the Ge NW networks. Transmittance and dark resistance variation with NW density was investigated. With increased NW density, transmittance of the network decreased while its dark resistance was increased. Then, fully transparent flexible

photodetectors were fabricated using deposited Ge NW networks as active material and Ag NWs and SWNTs as the electrode materials. Light ON/OFF and I-V measurements were conducted for both Ag-Ge and SWNT-Ge NW photodetectors for different Ge NW network densities and bending radius for flexible devices. All devices had fast response and relaxation times, which were below 10 milliseconds. Photoresponse current increased with Ge NW density in the network, while the current ratio stayed constant. Bending radius affected both dark and light current of the devices. Current increased around 10% from its initial value with increased radius. This effect was attributed to better mechanical contact during bending. SWNT-Ge photodetectors have lower dark current when compared to Ag-Ge photodetectors as sheet resistance of SWNT thin films was higher than that of Ag networks. It was concluded in this thesis that devices that use NW networks have potential to have better performances and easier fabrication techniques over their bulk counterparts. Our results open up a field of transparent and flexible devices using all NW network enhanced fabrication.

## **4.2 Future Recommendations**

In this thesis, it is proven that Ge NWs can be synthesized with desired diameters using solid precursors through vapor transport method. It is also possible within this method to control the length of the NWs so length control of the Ge NWs can be investigated. Ge NWs can grow using various catalysts other than Au, such as platinum (Pt), silver (Ag), palladium (Pd), copper (Cu) and nickel (Ni). These catalysts have been investigated with in CVD growth [95] so, their behavior in vapor transport growth can also be investigated.

After the synthesis Ge NWs were utilized in fully transparent, flexible photodetectors. Photoresponse characterization of the devices was made using a full spectrum solar simulator, the characterizations can also be conducted with IR light source. Spectral response measurements of fabricated photodetectors can also be

done. Ge NWs were successfully transported from the growth substrate to the device substrate as explained previously. Ease of transportation of the NWs enables utilization in many different devices therefore, synthesized NWs can be used in field effect transistors, solar cells, chemical and biological sensors.

## REFERENCES

- [1] G.H. Tu, Germanium Nanowire Controlled Synthesis, Allignment and Field Effect Transistor Characteristics, (Thesis, Ph.D.), Department of Materials Science and Engineering and the Committee on Graduate Studies of Stanford University, 2007, 1.
- [2] J. Sarkar, G. G. Khan and A. Basumallick, *Bull. Mater. Sci.*, 2007, 30, 271.
- [3] C. L. Chien *J. Appl. Phys.* 1991,69, 5267.
- [4] T. T. Albrecht, J. Schotter, G. A. Kästle, N. Emley, T. Shibauchi, L. K. Elbaum, K. Guarini, C. T. Black, M. Tuominen and T. P. Russell, *Science*, 2000, 290, 2126.
- [5] K. Nielsch, F. Muller, A. P. Li and U. Gosele, *Adv. Mater.*, 2000, 12, 582.
- [6] Z. Zhang, X. Sun, M. S. Dresselhaus, J. Y. Ying and J. Heremans, *Phys. Rev. B*, 2000, 61, 4850.
- [7] J. Heremans, C. M. Thrush, Y. M. Lin, S. Cronin, Z. Zhang, M. S. Dresselhaus and J. F. Mansfield, *Phys. Rev. B*, 2000, 61, 2921.
- [8] Y. M. Lin, O. Rabin, S. B. Cronin, J. Y. Ying and M. S. Dresselhaus, *Appl. Phys. Lett.* 2002, 81, 2403.
- [9] J. Heremans, C. M. Thrush, D. T. Morelli and M. C. Wu, *Phys. Rev. Lett.*, 2002, 88, 216801.
- [10] C. Dames and G. Chen 21st Int. conf. thermoelectrics: Proc. ICT symposium, Long Beach (Piscataway: IEEE) 2002, 317.

- [11] G. Dresselhaus, M. S. Dresselhaus, Z. Zhang, X. Sun, J. Ying and G. Chen, 17th Int. conf. thermoelectrics: Proc. ICT'98, 1998, 43–46.
- [12] G. Chen, M. S. Dresselhaus, G. Dresselhaus, J. P. Fluerial and T. Caillat, Int. Mater. Rev. 2003, 48.
- [13] A. I. Hochbaum, R. Chen, R. D. Delgado, W. Liang, E. C. Garnett, M. Najarian, A. Majumdar & P. Yang, Nature, 2007, 451, 163.
- [14] Bhushan B (ed.) Springer handbook of nanotechnology, 2005, Berlin, Heidelberg: Springer.
- [15] B. Wang, S. Yin, G. Wang and J. Zhao, J. Phys.: Condens. Matter, 2001, 13, L403.
- [16] J. Zhao, C. Buia, J. Han and J. P. Lu, Nanotechnology, 2003, 14, 501.
- [17] D.A. Smith, Mechanical, Electromechanical, and Optical Properties of Germanium Nanowires, Thesis (Ph. D.), Faculty of the Graduate School of The University of Texas at Austin, 2009, 3-5.
- [18] A. K. Wanekaya, W. Chen, N. V. Myung and A. Mulchandani, Electroanalysis, 2006, 18 533.
- [19] C. F. Bohren and D. R. Huffman, Absorption and scattering of light by small particle 1983, New York: Wiley.
- [20] J. Wang, A. Rahman, G. Klimeck and M. Lundstrom, IEEE, 2005, 10.
- [21] D. Wang, H. Dai, Appl. Phys. A, 2006, 85, 217.
- [22] Y. H. Ahn, J. Park, Appl. Phys. Lett., 2007, 91, 162102.

- [23] B. Polyakov, B. Daly, J. Prikulis, V. Lissauskas, B. Vengalis, M. A. Morris, J. D. Holmes and D. Ertz, *Adv. Mater.* 2006, 18, 1812.
- [24] F. Leonard, A. A. Talin, B. S. Swartzentruber and S.T. Picraux, *PRL*, 2009, 102, 106805.
- [25] Y. Zhang, S.B. Kim, J.P. McVittie, H. Jagannathan, J.B. Ratchford, C.E.D. Chidsey, Y. Nishi, and H.S. Philip Wong, *IEEE Transactions On Electron Devices*, 2008, 55, 9.
- [26] L. Li, X. Fang, H. G. Chew, F. Zheng, T. H. Liew, X. Xu, Y. Zhang, S. Pan, G.Li, and L. Zhang, *Adv. Funct. Mater.* ,2008, 18, 1080.
- [27] C.J. Kim, H.S. Lee, Y.J. Cho, K. Kang, M.H. Jo, *Nano Lett.* ,2010, 10, 2043.
- [28] C.J. Kim , H.S. Lee , Y.J. Cho , J.E. Yang , R. R. Lee , J. K.Lee, and M.H. Jo, *Adv. Mater.* 2011, 23, 1025.
- [29] C. Yan, N. Singh, H. Cai, C. L. Gan, and P. S. Lee, *ASC Appl, Mat. Interfaces*, 2010, 2, 1794.
- [30] D. Wang, *Pure Appl. Chem.*, 2007,79, 65.
- [31] C. Fang, H. Foll, and J. Nano Lett, 2006, 6, 1578.
- [32] T. Hanrath, B. A. Korgel. *Small*, 2005, 1, 717.
- [33] T. Hanrath, B. A. Korgel. *J. Am. Chem. Soc.*, 2002, 124, 1424.
- [34] R. S. Wagner and W. C. Ellis, *Appl. Phys. Lett.*, 1964, 4, 89.
- [35] A. M. Morales, C. M. Lieber. *Science* ,1998, 279, 208.
- [36] T. I. Kamins, X. Li, and R. Stanley Williams, X. Liu, *Nano Lett*, 2004 4, 3, 503.
- [37] D. Wang and H. Dai, *Angew. Chem.* 2002, 114, 24, 4977.
- [38] S. Kodambaka, J. Tersoff, M. C. Reuter, F. M. Ross, *Science*, 2007, 316, 729.

- [39] J. W. Dailey, J. Taraci, T. Clement, D. J. Smith, J. Drucker, S. T. Picraux. J. Appl. Phys. 2004, 96, 7556.
- [40] S.Mathur, H. Shen, V. Sivakov, U. Werner, Chem. Mater. 2004, 16, 2449.
- [41] C.B. Jin, J.E. Yang, and M.H. Jo, Appl. Phys. Lett., 2006, 88, 193105.
- [42] J. W. Dailey, J. Taraci, and T. Clement, D.J. Smith, J. Drucker, S. T. Picraux, J. Appl. Phys., 2004, 96, 12, 7556.
- [43] H. Omi, T. Ogino. Appl. Phys. Lett. 1997,71, 2163.
- [44] Y. Y. Wu, P. D. Yang. Chem. Mater. 2000,12, 605.
- [45] G. Gu, M. Burghard, G. T. Kim, G. S. Dusberg, P. W. Chiu, V. Krstic, S. Roth, W. Q. Han. J. Appl.Phys. 2001, 90, 5747.
- [46] Y. F. Mei, Z. M. Li, R. M. Chu, and Z. K. Tang, G. G. Siu, Ricky K. Y. Fu, and Paul K. Chu, W. W. Wu and K. W. Cheah, Appl. Phys. Lett., 2005, 86, 021111.
- [47] C.Yan, M. Y. Chan, T. Zhang, and P. S. Lee, J. Phys. Chem. C, 2009, 113, 1705.
- [48] Y. Wu and P. Yang, J. Am. Chem. Soc., 2001, 123, 3165.
- [49] B. Yu, X. H. Sun, G. A. Calebotta, G. R. Dholakia and M. Meyyappan, J. Cluster Sci., 2006,17, 4, 579.
- [50] X. H. Sun, C. Didychuk, T. K. Sham, and N. B. Wong, Nanotech., 2006, 17, 2925.
- [51] H. Dong, H. Zhu, Q. Meng, X. Gong, and W. Hu, Chem. Soc. Rev., 2012, 41, 1754.
- [52] C. Claeys, E. Smoen, Germanium-Based Technologies From Materials to Devices, Elsevier, 2007.
- [53] A. Rogalski, Progress in Quantum Electronics, 2003, 27, 59.

- [54] J. Wang and S. Lee, *Sensors*, 2011, 11, 696.
- [55] S.Fama, L. Colace, G. Masini, G.Assanto, H.Luan, *Appl. Phys. Lett.*, 2002, 81, 586.
- [56] S. Klinger, M.Berroth, M.Kaschel, M.Oehme, E.Kasper, *IEEE Photon. Technol. Lett.* 2009, 21, 920.
- [57] J. Liu, J. Michel, W. Giziewicz, D. Pan, K. Wada, D. Cannon, S. Jongthammanurak, D. Danielson, L. Kimerling, J. Chen, *Appl. Phys. Lett.* 2005, 87, 103501.
- [58] M.Jutzi, M.Berroth, G. Wöhl, M.Oehme, E.Kasper, *Mater. Sci. Semicond. Process.* 2005, 8,423.
- [59] Y. Kang, H.Liu, M.Morse, M.Paniccia, M.Zadka, S. Litski, G.Sarid, A.Pauchard, Y. Kuo, H.Chen, *Nat. Photon.* 2008, 3, 59.
- [60] S. Assefa, F. Xia, Y.Vlasov, *Nature*, 2010, 464, 80.
- [61] K. Ang, J. Ng, A. Lim, M. Yu, G. Lo, D. Kwong, *Communication Conference and Exposition and the National Fiber Optic Engineers Conference (OFC/NFOEC 2010)*, Los Angeles, 2010, CA, USA, 21–25.
- [62] D. Decoster, J. Harari, *Optoelectronic Sensors*, Wiley, 2009, 1-14.
- [63] C. Soci, A. Zhang, X.Y. Bao, H. Kim, Y. Lo, and D. Wang, *Journal of Nanoscience and Nanotechnology*, 2010,10, 1.
- [64] G. Gu, M. Burghard, G. T. Kim, G. S. Dusberg, P. W. Chiu, V. Krstic, S.Roth, W.Q. Han, *J. Appl. Phys.*, 2001, 90, 5747.

- [65] L. Colace, V. Sorianello, M. Balbi, G. Assanto, *Appl. Phys. Lett.*, 2007, 91, 021107.
- [66] C. Yan, N. Singh, H. Cai, C. L. Gan, and P. S. Lee, *ACS Appl. Mater. Interfaces*, 2010, 2, 1794.
- [67] B. R. Huang, J. F. Hsu, C. S. Huang, Y. T. Shih, K. S. Lu, *Mater. Sci. Eng.* 2007, 27, 1197.
- [68] C. Yan, N. Singh, P. S. Lee, *Appl. Phys. Lett.* 2010, 96, 053108.
- [69] C. C. Lin, W. H. Lin and Y. Y. Li, *J. Nanosci. Nanotechnol.* 2009, 9, 2813.
- [70] H. Bao, C. M. Li, X. Cui, Q. Song, H. Yang and J. Guo, *Nanotechnology*, 2008, 19, 335302.
- [71] H. E. Unalan, Y. Zhang, P. Hiralal, S. Dalal, D. Chu, G. Eda, K. B. K. Teo, M. Chhowalla, W. I. Milne, and G. A. J. Amaratunga, *Appl. Phys. Lett.* 2009, 94, 163501.
- [72] A. D. Pasquier, H. E. Unalan, A. Kanwal, S. Miller, M. Chhowalla, *Appl. Phys. Lett.* 2005, 87, 203511.
- [73] H. E. Unalan, G. Fanchini, A. Kanwal, A. D. Pasquier, M. Chhowalla *Nano Lett.*, 2006, 6, 677.
- [74] S. De, T. M. Miggins, P. E. Lyons, E. M. Doherty, P. N. Nirmalraj, W. J. Blau, J. J. Boland, J. N. Coleman, *ACS Nano*, 2009, 3, 1767.
- [75] J. Wu, M. Agrawal, H. A. Becerril, Z. Bao, Z. Liu, Y. Chen, P. Peumans, *ACS Nano* 2010, 4, 43.
- [76] Q. Cao, Z. T. Zhu, M. G. Lemaitre, M. G. Xia, M. Shim, *Appl. Phys. Lett.* 2006, 88, 113511.

- [77] M.W. Rowell, M.A. Topinka, M.D. McGehee, H.J. Prall, G. Dennler, N.S. Sarıçift, L. Hu, G. Gruner, *Appl.Phys. Lett.* 2006, 88, 233506.
- [78] L. Hu, D.S. Hecht, G. Gruner, *Appl. Phys. Lett.* 2009, 94, 081103.
- [79] S. De, T.M. Miggins, P.E. Lyons, E.M. Doherty, P.N. Nirmalraj, W.J. Blau, J.J. Boland, J.N. Coleman, *ACS Nano*, 2009, 3, 176.
- [80] Y. Choi, *IJAST*, 2010, 24, 75.
- [81] A. Behnam, J. Johnson, Y. Choi, L. Noriega, M.G. Ertosun, Z. Wu, A. G. Rinzier, P. Kapur, K. C. Saraswat, A. Ural, *J. Appl. Phys.* 2008, 103, 114315.
- [82] L. Yuan, J. Dai, X. Fan, T. Song, Y.T. Tao, K. Wang, Z. Xu, J. Zhang, X. Bai, P. Lu, J. Chen, J. Zhou, Z.L. Wang, *ACS Nano*, 2011, 5, 4007.
- [83] M.C. McAlpine, H. Ahmad, D. Wang, J.R. Heat, *Nature*, 2007, 23, 1.
- [84] W. F. Zhang, Z. B. He, G. D. Yuan, J. S. Jie, L. B. Luo, X. J. Zhang, Z. H. Chen, C. S. Lee, W. J. Zhang, S. T. Lee *Appl. Phys. Lett.*, 2012, 94, 123103.
- [85] A. Nadarajah, R.C. Word, J.Meiss, R. Konenkamp, *Nano Lett.*, 2008, 8, 534.
- [86] G. Zhu, R.Yang, S. Wang, Z.L. Wang, *Nano Lett.*, 2010,10, 3151.
- [87] D. Kuang, J. Brilllet, P.Chen, M. Takata, S.Uchida, H. Miura, K. Sumioka, S.M. Zakeeruddin, M. Gratzel , *ACS Nano*, 2008, 2, 1113.
- [88] Sun, Y.; Gates, B.; Mayers, B.; Xia, Y. *Nano Lett.*, 2002, 2, 165.
- [89] S. Coskun, B. Aksoy, and H. E. Unalan, *Cryst. Growth Des.*, 2011, 11, 4963.
- [90] B.B. Parekh, G. Fanchini, G.Eda, M. Chhowalla, *Appl. Phys. Lett.*, 2007,90, 121913.

- [91] K. Heo, H. Lee, Y. Park, J. Park, H. J. Lim, D. Yoon, C. Lee, M. Kim, H. Cheong, J. Park, J. Jian, S. Hong, *J. Mater. Chem.*, 2012, 22, 2173.
- [92] J. Zhou, Y. Gu, Y. Hu, W. Mai, P.H. Yeh, G. Bao, A. K. Sood,<sup>4</sup> D. L. Polla,<sup>5</sup> and Z. L. Wang, *Appl. Phys. Lett.*, 2009, 94, 191103.
- [93] B. R. Huang, J.F. Hsu, C.S. Huang, Y.T. Shih, K.S. Lu, *Mater. Sci. Eng.* 2007, 27, 1197.
- [94] X.T. Zhou, J.Q. Hu, C.P. Li, D.D.D. Ma, C.S. Lee, S.T. Lee. *Chem. Phys. Lett.*, 2003, 369, 220.
- [95] J. L. Lensch-Falk, E. R. Hemesath, D.E. Perea and L. J. Lauhon, *J. Mater. Chem.*, 2009, 19, 849.